Towards Modeling Delaminations Along Arbitrary Interfaces in Multi-layered Composite Shells: Interlaminar Coupling with Geometrically Exact Shell Finite Elements

Addressing Large Deformation and Buckling

Aamir Ali

Delft University of Technology

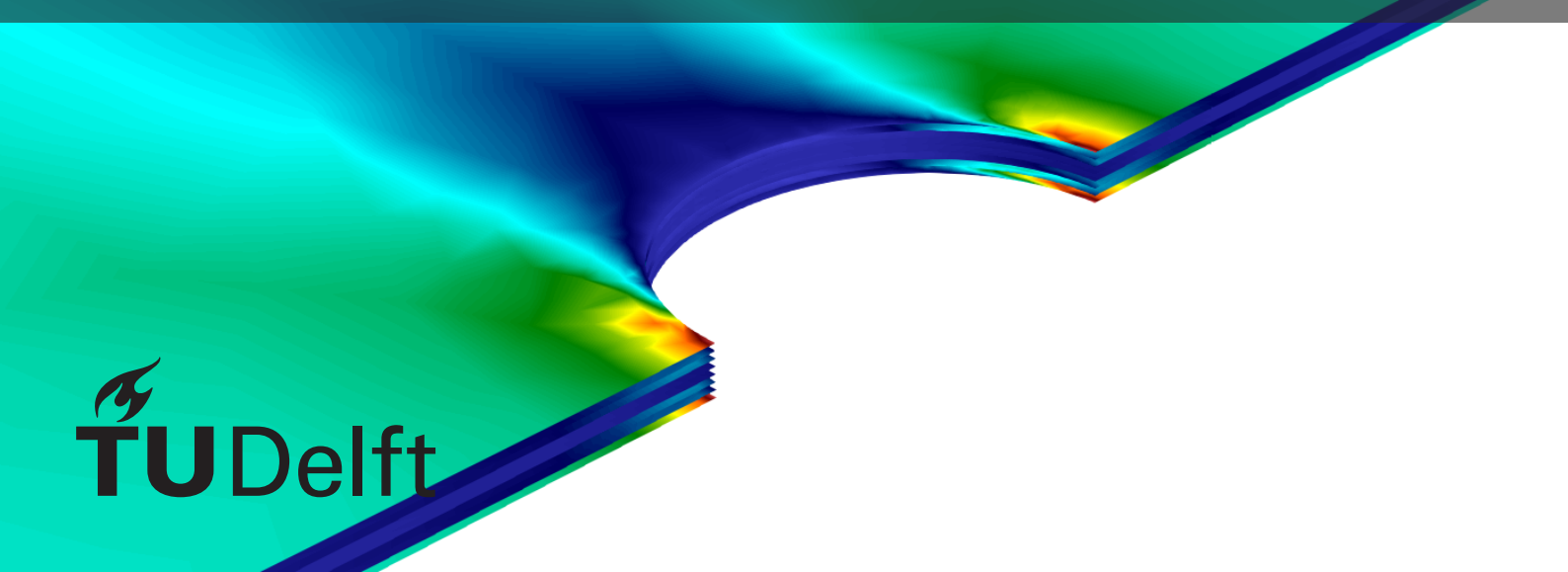

TU Delft

Towards Modeling Delaminations Along Arbitrary Interfaces in Multi-layered Composite Shells: Interlaminar Coupling with Geometrically Exact Shell Finite Elements

Addressing Large Deformation and Buckling

by

Aamir Ali

to obtain the degree of Master of Science
at the Delft University of Technology,
to be defended publicly on Tuesday November 5, 2024 at 10:00.

Student number:	4959892	
Project duration:	January 08, 2024 – November 5, 2024	
Thesis committee:	Dr. B. Giovanardi,	TU Delft, supervisor
	Dr. B. Chen,	TU Delft, chair
	Dr. B. Caglar,	TU Delft, external member

An electronic version of this thesis is available at http://repository.tudelft.nl/.

TU Delft

Acknowledgments

For the few who are going to read this: I would like to express my gratitude to Dr. Bianca Giovarnardi for her guidance and support throughout this thesis, which marks the completion of my Master's degree in Aerospace Engineering at Delft University of Technology. Her ability to break down a complex concept was especially helpful in the early stages, and her feedback has been crucial to the development of this work. Additionally, I would like to thank Timothy for answering numerous coding-related questions and engaging in interesting discussions.

I also want to thank my friends for their support during this project. Nathan and Malolan, in particular, have been working on similar topics, and we have often found ourselves venting about the frustrations inherent in modeling damage—only to realize that in the process, we were damaging ourselves as well. Sharing these challenges with them made the journey a little more manageable.

Lastly, I want to thank my family for their support.

Aamir Ali
Delft, November 2024

*"**Programming**: the art of hating every minute until you get it right, then loving every second—until the next bug."*

-Aamir Ali

Executive Summary

Traditional aircraft wings rely on flaps and ailerons for flight control, which are usually optimized for only one flight condition. To address this, morphing wings have been developed that can change shape during flight to improve aerodynamic efficiency. Specifically, new research is exploring controlled buckling—once seen as a structural failure mode—to create *passive* morphing systems. Thin-walled, multi-layered composites can be used within these morphing structures to minimize weight. However, during buckling, these structures are susceptible to matrix cracks and delaminations, these matrix cracks allow delaminations to traverse multiple interfaces — a process referred to as delamination migration. Although it is critical to experimentally obtain the failure loads of composite structures, the process of manufacturing test samples and setting up high-fidelity experimental tests—including a complete set of measurements—can be complex and expensive. Calling for advanced modeling techniques.

To effectively model these migrations, it is essential to understand the interaction between interlaminar and intralaminar damage. This thesis represents a step towards developing a unified approach for modeling both matrix cracks and delaminations in composite materials. Specifically, it introduces a high-fidelity finite element methodology that explicitly models each layer in a multi-layered composite structure as individual shells. This approach is crucial for simulating delaminations along arbitrary interfaces, as it can be complemented with cohesive finite elements at all interfaces between laminae.

The developed model was then extensively analyzed. First, verification on the models is performed on four benchmarks: free vibration, post-buckling behavior, beam twist, and beam roll-up. Four different configurations were modeled, using one, two, four, and eight layers, while keeping the overall thickness of the laminate constant across all cases. In the first model, the shell is excited by its first mode shape. By comparing the results to the analytical solution, this model demonstrates that the rotational inertia of each layer has been properly calculated. The second model tests how the four configurations respond to the buckling load calculated for a single-layer shell. It confirmed that distributing the load across all layers produces the same post-buckling response. The third model examines the behavior of a thick shell under applied torque, evaluating its response to a large torsional deformation. The fourth verification model is the classic Euler beam roll-up problem. In this case, a moment is applied at the tip of the shell, causing it to roll into a circle. This model is widely used to test large deformations and nonlinear behavior. The last two models revealed an issue with the current implementation of the stability terms designed to prevent relative displacements between layers. While the term correctly maintains separation between layers, it does not do so in the direction of the thickness, thus causing the interpenetration of layers. The source of this issue has been identified, along with a potential solution.

Simple numerical experiments were conducted to evaluate the model's ability to capture the coupling behavior typical of composite materials. An out-of-plane load was applied to one edge to observe whether a shell with a unidirectional layup twists under varying fiber angles. As expected, no twist was observed for the $\theta = 0°$ and $\theta = 90°$ models, while the greatest twist occurred in the $\theta = 30°$ model, with a slight twist seen at $\theta = 60°$. However, when using an antisymmetric layup with symmetric upper and lower halves, no twist was observed, confirming the anticipated behavior. This demonstrates that altering the layup can negate the shear in each layer, effectively eliminating the twist. The final numerical experiment involved an open hole tension test with a symmetric layup, where stress concentrations around the hole were compared against experimental results, indicating the direction of the matrix cracks. A good agreement was observed between the two.

The results of this thesis demonstrate the feasibility of explicitly modeling each layer in a composite laminate. This approach lays the groundwork for creating a unified framework that addresses both intralaminar and interlaminar interactions.

Acronyms

CDM Continuum Damage Mechanics. 4, 16, 19, 22, 23, 27, 28
CERR Critical Energy Release Rate. 20, 23
CLPT Classical Laminated Plate Theory. 7–9, 11, 30
CZM Cohesive Zone Model. 4, 5, 7, 14, 19, 21, 23, 25–28, 30

DCB Double Cantilever Beam. vi, 14–16, 18, 21, 22
DG/CZM Discontinuous Galerkin/Cohesive Zone Model. 5, 15, 30, 90

ERR Energy Release Rate. vi, 16, 17, 20, 25, 29
ESL Equivalent Single Layer. 6, 7, 10, 12, 13, 30

FEM Finite Element Method. 10, 21, 23, 38
FNM Floating Node Method. 4, 5, 14, 20, 31
FRP Fiber-Reinforced Polymer. 23
FSDT First-Order Shear Deformation. vi, 8–12, 15, 16, 22, 30
FZZT First-Order Zig-Zag Theory. 12

LEFM Linear Elastic Fracture Mechanics. 16, 17, 20, 22, 25

MLCL Multi-Linear Cohesive Law. 27

OOP Object-Oriented Programming. 54

PDE Partial Differential Equation. 5, 46
PNM Phantom Node Method. 4, 5, 14, 17, 20, 30, 31

TSL Traction-Separation Law. vi, 5, 23, 26, 27

VCCT Virtual Crack Closure Technique. 4, 14, 20, 30

XFEM eXtended Finite Element Method. 4, 5, 14, 17, 21, 22, 30, 31

Contents

List of Figures

List of Tables

Chapter 1

Introduction

In recent years, the extensive use of advanced composites in various engineering disciplines has generated significant attention, mostly due to their exceptional stiffness-to-weight ratio and tailorability. From tennis rackets to large wind turbine blades, the utilization of composite materials spans a wide array of applications [1–5]. The tailorability of composites allows for fine control of properties such as specific stiffness, strength, and fracture toughness [3]. However, a good understanding of their failure mechanisms and correct modeling approaches are needed in order to design safe structures.

1.1. Exploiting Buckling in Aerospace Applications

One promising application of buckling exploitation in aerospace is in morphing wings. These wings, capable of changing their shape in-flight to optimize aerodynamic performance, require structures that can dynamically adapt to external loads. The term *"morph"*, derived from the Greek word *"morphos"*, meaning shape, highlights the ability of these wings to alter their form in response to varying flight conditions [6]. A historical overview of morphing wing concepts can be found in [6].

During takeoff and landing, aircraft use flap control to adjust the wing's aerodynamic properties, increasing lift by extending the flaps to enlarge the wing surface and modify its camber. This enables the aircraft to achieve the necessary lift at lower speeds, which is essential during takeoff and crucial for maintaining control during landing. Similarly, morphing wings aim to optimize aerodynamic shape for different flight conditions, adapting in real-time to improve performance during various phases of flight, such as takeoff, cruise, and landing. By dynamically adjusting the wing's shape, morphing wings can enhance the flight envelope, control, and range. Moreover, they offer the potential to reduce design, manufacturing, and maintenance costs by eliminating the need for multiple mission-specific aircraft designs, replacing them with a single, adaptable system [6].

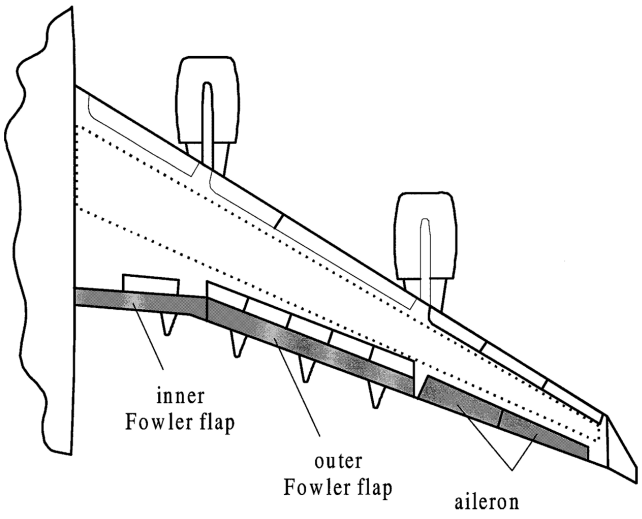

Figure 1.1: Flaps and ailerons of a typical transport aircraft [7].

An aircraft wing, traditionally equipped with flaps and ailerons is shown in Figure 1.1. One of the more conventional morphing wing concepts is the Fowler flap, illustrated in Figure 1.2. This system, in addition to enhancing the Fowler flap with an additional cambering function, also provides the potential to completely remove the aileron. This concept is also called the *"finger concept"* since it is based on an active rib structure, the individual elements of which, similar to the human finger, are successively tilted towards each other via a kinematic coupling arrangement [7]. Since the ribs are deflecting downwards, the upper and lower skin cannot be connected but should allow sliding over the ribs to avoid buckling. At the trailing edge a linear slide bearing is thus needed. The fixed front section is not changed to avoid a totally new design.

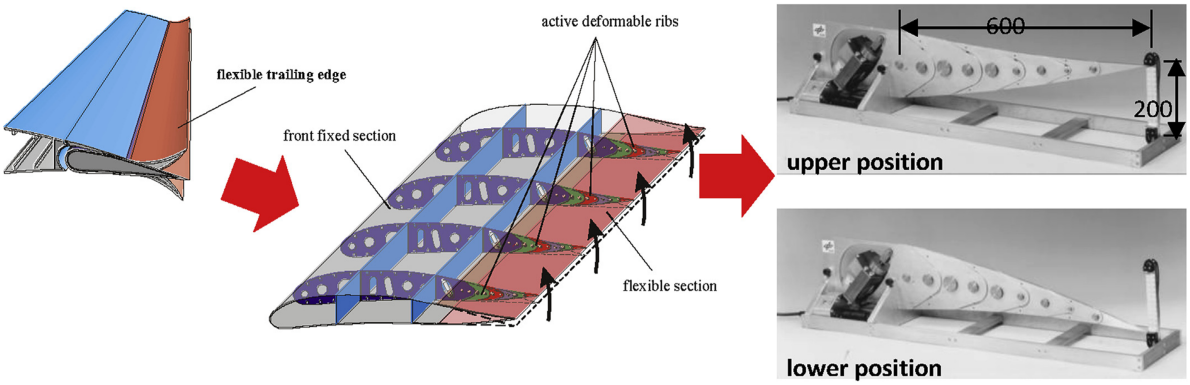

Figure 1.2: Position and design of active deformable ribs in the Fowler flap [6, 7].

Recent literature has proposed to incorporate buckling-driven mechanisms [8], such as localized constraints that guide deformation, allowing for multi-stable configurations states where the wing maintains stability under different aerodynamic conditions. Traditionally, buckling has been regarded as a failure mode to be avoided as it is associated with large deformations and loss of load-carrying capacity [8]. However, the potential of controlled buckling lies in its ability to induce significant structural deformations with minimal actuation input. By designing elements to operate within the post-buckling regime, structural weight can potentially be reduced while maintaining the same load-bearing performance. This is particularly relevant for composite materials, which offer high strength-to-weight ratios and can be tailored to exploit buckling without compromising the overall integrity of the structure. In the work of [8], the post-buckling behavior of the wing is tailored by the stiffness of the rear spar relative to the rest of the structure. Buckling-driven mechanisms enable the structure to adjust its stiffness in response to varying load conditions, see Figure 1.3.

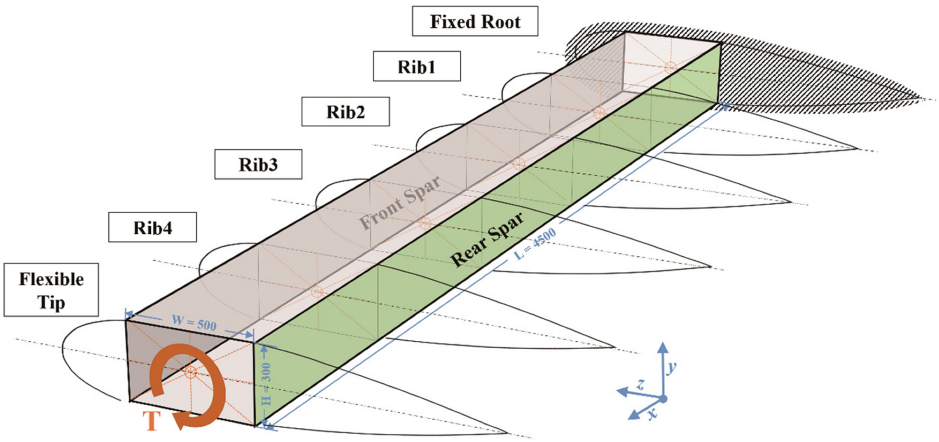

Figure 1.3: Model of wing box used to investigate the buckling-driven mechanisms of the rear spar [8].

Controlled buckling mechanisms thus enable the development of passive morphing systems, which respond automatically to certain aerodynamic loads without the need for complex active control systems [8]. This opens up a wide design space for compliant mechanisms that utilize elastic instabilities to achieve desired shapes and responses. However, these mechanism also influence the failure modes, e.g., skin-stiffener separation. In 2017, Dávila and Bisagni [9] investigated the effect of damage on stiffened post-buckled composite structures. During post-buckling, as the load increases, the initial buckling causes out-of-plane displacements in the skin, which progressively increases. The delamination at the skin-stiffener interface typically begins near a defect, in this case a teflon insert, and propagates both along the flange and towards the loading direction. This propagation is driven by the out-of-plane deflection, particularly at the inflection points where the skin moves away from the stiffener [9]. As the delamination grows, the structural stiffness decreases, leading to a change in buckling mode and the eventual collapse of the structure. The study shows that once delamination initiates, it can propagate rapidly under continued cyclic loading, leading to a catastrophic failure. The change in buckling mode is caused by the formation of a tunnel under the stiffener when it detaches from the skin, unsurprisingly named *"tunneling"* [9]. Skin-stiffener separation is also known to lead to matrix cracking, occurring right after skin-stiffener separation allowing the delamination to migrate into the skin [9, 10].

1.2. Modeling Damage in Composites

Based on the previously discussed skin-stiffener separation, and given the use of thin-walled multi-layered composite components in aerospace applications, such as aircraft fuselages [2], it is crucial to accurately model damage. The primary design objective is to minimize weight while effectively withstanding external loads. However, simulating damage in these multi-layered composite components presents several challenges due to their laminated and non-homogeneous nature [11].

For a multidirectional laminate, regardless of the complexity of the initial delamination process, the progression consistently ends at the $0°/\theta°$ interface [12]. Off-axis laminae are particularly susceptible to matrix cracking, which allows the delamination to traverse multiple interfaces until it reaches a $0°$ lamina. At this point, further propagation is typically halted, as the $0°$ interface prevents additional crack migration. Consequently, it can be observed that *interlaminar* toughness decreases as the lamina angle increases. In one of the test cases, a pre-crack initiated delaminations at three additional interfaces, one of which propagated opposite to the loading direction.

The process of manufacturing test samples and conducting physical tests, which typically involves many samples and manual operations, is both costly and time-consuming. This has led to a growing demand for more economically efficient methods of structural testing, increasingly relying on simulations [13]. The development of accurate and computationally efficient formulations capable of predicting the failure process of large-scale structures, is a complex and still ongoing task, even after decades of research.

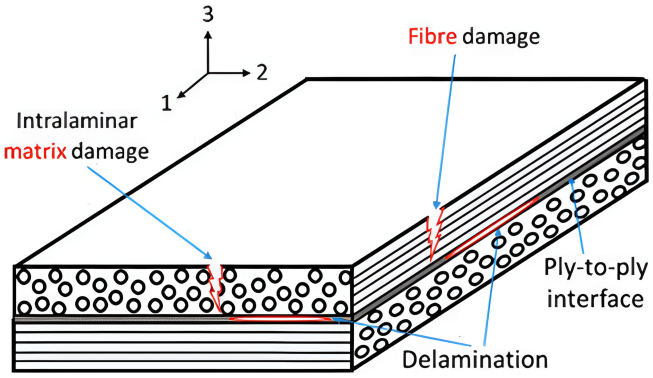

Figure 1.4: Fiber, interlaminar and intralaminar damage [13].

Major modeling challenges stem from the inherent complex mechanics of damage, which occurs at

scales that are orders of magnitude smaller than the structural components to be analyzed [11]. Damage in laminated composites is typically classified into two categories, namely, *intralaminar* and *interlaminar* damage, as shown in Figure 1.4. *Intralaminar* damage, confined to a single lamina, encompasses fiber breaking, matrix cracking, and fiber-matrix debonding. On the other hand, *interlaminar* damage, also known as delamination, occurs at the laminae interfaces, involving the physical separation of initially connected laminae [11, 14].

When it comes to addressing *intralaminar* damage, the introduction of Continuum Damage Mechanics (CDM) gave rise to significant progress. This approach aims to simulate, at the continuum level, the equivalent effects of various *intralaminar* damage modes mentioned earlier. Noteworthy contributions in this domain include the work of Ladeveze and Le Dantec [15], who utilized CDM to describe the macroscopic and continuum-level effects of matrix cracking and matrix/fiber debonding.

The modeling and simulation of *interlaminar* damage is less complicated. One common approach to simulate delamination involves the placement of cohesive interface elements between individual layers of the composite [16, 17]. In this framework, the laminate is represented at the level of each individual lamina. For instance, adjacent laminae with the same fiber orientation can be grouped into a single, thicker lamina for modeling purposes [11]. The cohesive interfaces are introduced to establish connections between laminae and enforce appropriate traction-separation relationships, known as the Cohesive Zone Model (CZM). CZMs can be distinguished based on their implementation within the model. *Intrinsic* cohesive models are inserted between elements before the simulation starts [18, 19]. Conversely, *extrinsic* cohesive models are inserted into the mesh after predicting the initiation of damage [19, 20]. It is important to note that the *extrinsic* approach requires the development of a systematic procedure, as nodes have to be created ad hoc and communicated to the rest of the calculation. Furthermore, in parallel computations, implementing the *extrinsic* framework is not trivial, facing various algorithmic challenges [16]. A drawback of both element types is that fracture can only occur where these elements are put in place [19]. If damage has to be calculated at other locations, interface elements have to be placed at these locations as well.

Several methodologies have been developed in recent years to model damage in fiber-reinforced composite laminates. In 2008, Bruno et al. [21] proposed a framework integrating CDM and Fracture Mechanics to capture the interaction between interlaminar and intralaminar damage mechanisms. In 2011, van der Meer et al. [22] introduced a computational approach for modeling progressive failure in composite laminates, using the Phantom Node Method (PNM) for matrix cracking, interface elements for delamination, and CDM for fiber failure. In 2012, Bouvet et al. [23] applied the CZM to simulate matrix cracking and delamination during low-velocity impacts, where fiber failure was taken into account using CDM. By 2015, De Carvalho et al. [24] combined the Floating Node Method (FNM) with the Virtual Crack Closure Technique (VCCT) to model delamination migration in cross-ply laminates. Also in 2015, Vigueras et al. [25] used eXtended Finite Element Method (XFEM) with a hybrid extrinsic and intrinsic CZM to model interlaminar and intralaminar damage interactions. The PNM was used to generate matrix cracks, with extrinsic cohesive elements inserted into the cracks, while intrinsic cohesive elements were placed between the layers to simulate delamination. In 2018, Bazilevs et al. [11] proposed a multi-layer modeling approach utilizing Kirchhoff-Love shell theory with the CZM to simulate interlaminar damage, and CDM to model intralaminar damage. In 2019, Yun et al. [26] developed a progressive damage model that integrates CDM and CZM, capturing interactions between delamination and matrix cracks by accounting for the crack direction and the degradation of the constitutive model. Finally, in 2020, Action and Leone [10] modeled delamination migration at a skin-stiffener interface into the skin through a matrix crack using CDM and the CZM.

When using both CDM for intralaminar failure and CZM for interlaminar delamination, the earlier mentioned interaction between interlaminar and intralaminar damage is unable to be captured, e.g., matrix cracks causing delamination growth or the the migration of delaminations to other interfaces as mentioned before. This method is unable to resolve the high stresses at the tip of a transverse crack in numerical simulations since elements where the transverse crack is predicted, soften without accurately capturing the stress field at the interface [11, 21, 26]. traditionally, CDM is unable to correctly predict the direction of crack propagation in composite materials since it does not account for the fiber direction. A

simple approach to circumvent this limitation is to align the mesh of each layer with the fiber direction manually and couple the laminae with constraints since the mesh does not align anymore [10]. This results in cracks being constrained by a band of elements whose length has to be small enough to capture this crack accurately. In contrast, the XFEM, FNM, and PNM in combination with cohesive elements are able to capture the interaction by introducing discontinuities within the elements as cracks develop. However, the system of equations grows in size during the simulation as additional degrees of freedom are activated to represent these discontinuities.

In 1973, Reed and Hill [27] laid the foundation for the Discontinuous Galerkin method by developing a methodology for solving hyperbolic Partial Differential Equations (PDEs). Recently, the Discontinuous Galerkin method has been proposed for elasticity problems [28]. The method involves partitioning the domain into individual element domains, which drastically increases the number of nodes and the accompanying degrees of freedom [2, 28, 29]. The shape functions incorporate possible discontinuities along interior element edges to describe the displacement field [19]. Stabilization integrals are introduced to enforce displacement compatibility across the internal element boundaries prior to fracture [2, 28]. These stabilization integrals are needed since they represent the internal forces keeping the structure together. The result of this approach is that each element domain has its own nodes and corresponding degrees of freedom; completely independent from neighboring elements. This approach of splitting the domain into smaller element domains is not efficient and increases the computational cost of the simulation. However, the Discontinuous Galerkin method is highly scalable since each element domain has its own shape functions and boundary conditions, thus compensating for the increased cost by computing the contribution of different interfaces in parallel [2, 19, 28]. Another advantage of this method is that since each element already has its own domain, no new nodes have to be created when damage is detected. Instead, cracks are initiated or propagated by deactivating the displacement compatibility integrals across the internal boundaries in the weak form and substituting them with traction-separation integrals [29]. Since this approach utilizes the CZM and the Discontinuous Galerkin method, it is also called the Discontinuous Galerkin/Cohesive Zone Model (DG/CZM) approach [19, 29].

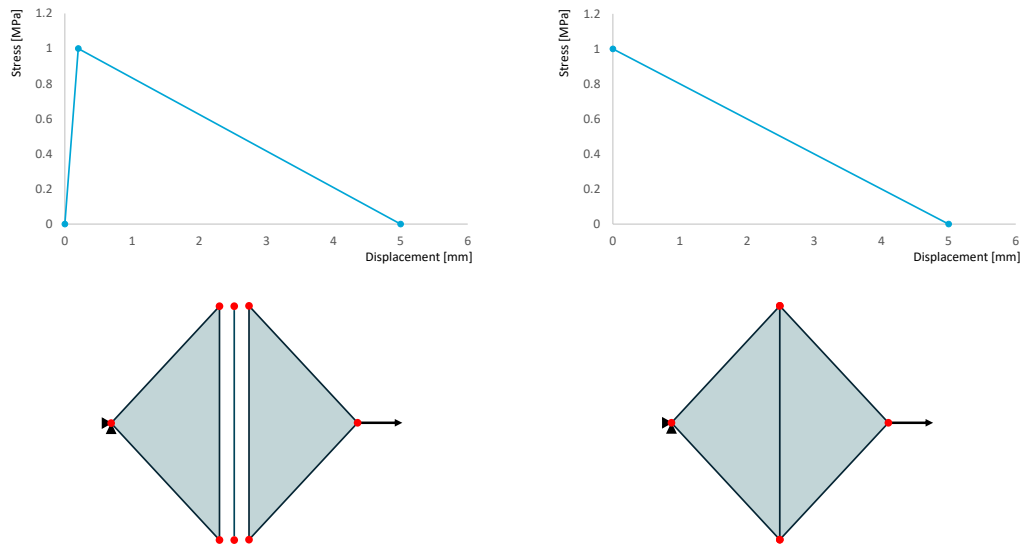

(a) Intrinsic cohesive law including an artifical elastic compliance.

(b) Extrinsic cohesive law without artificial elastic compliance.

Figure 1.5: Intrinsic and extrinsic TSLs.

When considering the challenges posed by the initial part of the traction-separation law, distinguishing between *intrinsic* and *extrinsic* approaches becomes crucial. As mentioned before, the *intrinsic* approach involves inserting interface elements before the simulation begins, where the traction-separation law often contains an unphysical artificial compliance, see Figure 1.5a, resulting in a linear elastic region prior to the actual softening region [16, 19, 30]. Placing such traction-separation laws at every interface would yield unsatisfactory results, despite the effective modeling of delaminations. This is because the

artificial compliance can significantly impact the accuracy of the computations [16].

Conversely, the *extrinsic* approach activates the interface element only upon the detection of damage [20], see Figure 1.5b. However, this approach encounters computational challenges as nodes need to be dynamically created and numbered during the simulation, leading to algorithmic difficulties [16]. In addressing these challenges, the Discontinuous Galerkin framework adopts a hybrid approach, incorporating elements of both *intrinsic* and *extrinsic* methodologies. The assumption is that damage can be initiated at any internal boundary, allowing for the creation of damage at all these internal boundaries. The softening process is activated when the stress-based failure criteria are satisfied, providing a practical compromise between the advantages of intrinsic and *extrinsic* approaches. An overview of several stress-based delamination failure criteria can be found in [31]. These criteria range from simple maximum stress models to more complex ones that account for the interactions between various stress components.

Finally, the thesis objective can be defined as follows:

Research Objective

To investigate the feasibility of high-fidelity Finite Element Methods for explicitly modeling each layer in multi-layered materials subjected to large deformations and buckling at the component level.

1.3. Thesis Outline

This thesis is structured as follows. Chapter 2 presents a comprehensive review of the existing literature, beginning with an overview of current plate theories such as Equivalent Single Layer (ESL), Layer-wise, and Zig-Zag theories. It then explores various approaches for modeling damage in composites, including interlaminar and intralaminar damage models, and concludes by identifying gaps in the literature. These gaps form the basis for the research questions. Chapter 3 starts by a description of the kinematic framework and the weak form of the governing equations. Chapter 4 presents the results of the verification studies and the numerical experiments into the behavior of composites, with an analysis of the model's accuracy in capturing these phenomena. Finally, Chapter 5 provides the conclusions and recommendations. It summarizes the key findings, revisits the research questions posed in Chapter 2, and offers suggestions for future research in this field.

Chapter 2

Literature Review

This chapter is organized into two key sections. First, Section 2.1 provides an in-depth review of various plate theories, discussing their relevance to the analysis of multi-layered materials and highlighting their respective strengths and applications. Following this, Section 2.2 delves into the methods used for damage modeling in composite materials, with a focus on techniques such as CZM and other frameworks for predicting damage and failure behavior. The chapter concludes by identifying a gap in the literature.

This literature review aims to develop a clear understanding of the methods for analyzing and simulating both the kinematic assumptions and damage mechanisms in multi-layered materials.

2.1. Existing Plate Theories

2.1.1. Equivalent Single Layer

ESL theories are derived from 3D elasticity theory by making assumptions about kinematics or stress distribution throughout the laminate's thickness. This approach simplifies the analysis of a complex, 3D structure into a 2D problem [32, 33]. In ESL theories, the displacement field is assumed to be a linear combination of unknown functions u_{ij} and the laminate thickness coordinate z^j:

$$u_i(x, y, z, t) = \sum_{j=0}^{N} z^j u_{ij}(x, y, t) \tag{2.1}$$

Theories belonging to this class are based on *a priori* assumptions involving a continuous displacement field through the entire thickness of the plate. However, they are less accurate in the analysis of structures exhibiting local nonlinear behavior which can be the case during large deformations [4, 5, 33]. Because of these simplifications, ESL theories typically offer limited accuracy in the modeling of e.g., interlaminar damage where the complex 3D stress state at the interfaces between layers must be known [34]. However, these theories are primarily suited for the global response of undamaged, very thin to relatively thick laminates, where the inability to resolve local stress and displacement field distributions within the laminate is less problematic [4, 5, 33]. To model damage accurately, 3D brick elements can be used, but such elements are computationally more expensive.

Classical Laminated Plate Theory

The simplest ESL plate theory is the Classical Laminated Plate Theory (CLPT), which is an extension of the classical Kirchhoff-Love plate theory [35]. The corresponding assumptions are [33]:

1. **Straight lines remain straight after deformation:** Straight lines that are perpendicular to the undeformed plate mid-surface (e.g., transverse normals) remain straight after deformation.
2. **No elongation of transverse normals:** The theory assumes that there is no elongation or contraction in the transverse direction of the plate, meaning that the thickness of the plate remains constant during deformation. This assumption states that the transverse displacement is independent of the thickness coordinate and the transverse normal strain ε_{zz} is zero.
3. **Normals to mid-surface remain normal:** The normal vectors to the mid-surface of the undeformed plate rotate such that they remain normal to the mid-surface after deformation. This assumption ensures that the transverse shear strains, ε_{xz} and ε_{yz}, are zero.

In CLPT the following assumptions and restrictions are made [33]:

- Individual layers are perfectly bonded (assumption).
- Each layer has a uniform thickness (restriction).
- Linear-elastic material with three planes of symmetry (restriction).
- Small strains and displacements (restriction).
- Zero transverse shear stresses on top and bottom surface (restriction).

Because of the restriction of small strains and displacements no distinction is made between the material coordinates X and the spatial coordinates x. This means that no distinguishment is made between the Second Piola-Kirchhoff and the Cauchy stress tensor, or between the Green-Lagrange strain tensor and the infinitesimal linear strain tensor. The displacement field u satisfying these assumptions is derived from the infinitesimal strain ε_{xz}. Starting with $\frac{\partial u}{\partial z} = -\frac{\partial w}{\partial x}$, integrating both sides with respect to z gives: $\int \frac{\partial u}{\partial z}\, dz = \int -\frac{\partial w}{\partial x}\, dz$. Integrating and doing the same for v and w gives [33]:

$$u(x, y, z, t) = u_0(x, y, t) - z\frac{\partial w_0}{\partial x} \tag{2.2a}$$

$$v(x, y, z, t) = v_0(x, y, t) - z\frac{\partial w_0}{\partial y} \tag{2.2b}$$

$$w(x, y, z, t) = w_0(x, y, t) \tag{2.2c}$$

Where u_0, v_0 and w_0 represent the displacement components of the mid-surface in the x, y and z directions, respectively. The terms $z\frac{\partial w_0}{\partial x}$ and $z\frac{\partial w_0}{\partial y}$ in the expressions for u and v, respectively, account for the change in the out-of-plane displacement w with respect to the x and y directions along the thickness of the plate, see Figure 2.1. Moderate rotations are in the order of of 10-15 degrees. In other words, deformation is entirely due to bending and in-plane stretching [33]. This formulation neglects the shearing of transverse normals. As a result the director (unit normal vector) is always perpendicular to the mid-surface.

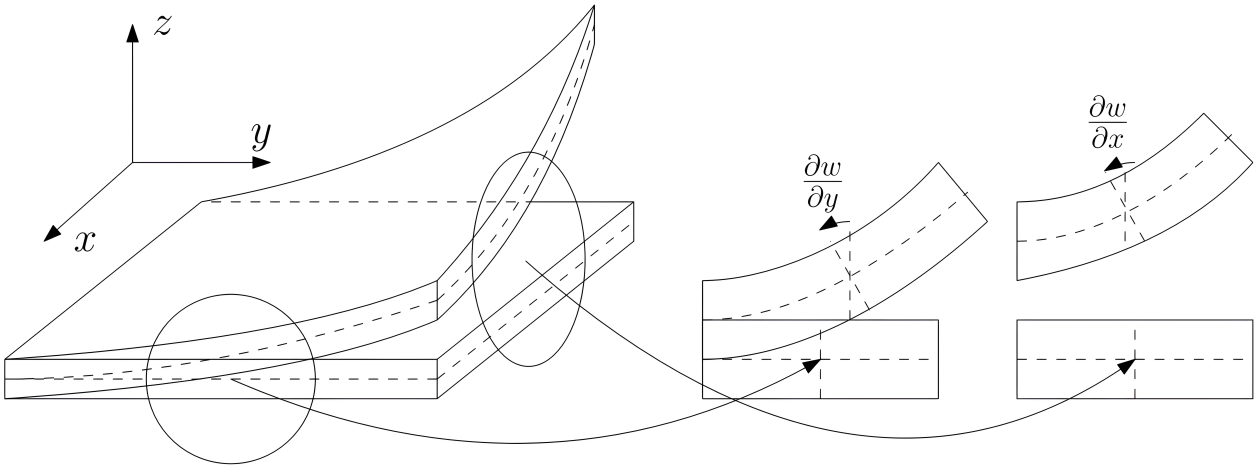

Figure 2.1: Kinematic assumption for CPLT using the Kirchhoff hypothesis [36].

First-Order Shear Deformation Theory

The displacement fields for FSDT by Reissner [37] and Mindlin [38] are typically represented by setting the order N equal to 1 for u and v, but 0 for w in Equation 2.1 [33]:

$$u(x, y, z, t) = u_0(x, y, t) + z\phi_x(x, y, t) \tag{2.3a}$$

$$v(x, y, z, t) = v_0(x, y, t) + z\phi_y(x, y, t) \tag{2.3b}$$

$$w(x, y, z, t) = w_0(x, y, t) \tag{2.3c}$$

Where ϕ_x and $-\phi_y$ in the expressions for u and v, account for rotations of the transverse normal about the y and x axes, respectively, see Figure 2.2. Thus relaxing the third constraint of the Kirchhoff hypothesis. When the ratio of in-plane dimensions to out-of-plane dimensions exceeds 50, the displacement field of Equation 2.3 approach the displacement field of Equation 2.2 [33]. Hence, for thin plates CLPT is used whereas for thicker plates FSDT is more accurate.

$$\phi_x = \frac{\partial u}{\partial z} \tag{2.4a}$$

$$\phi_y = \frac{\partial v}{\partial z} \tag{2.4b}$$

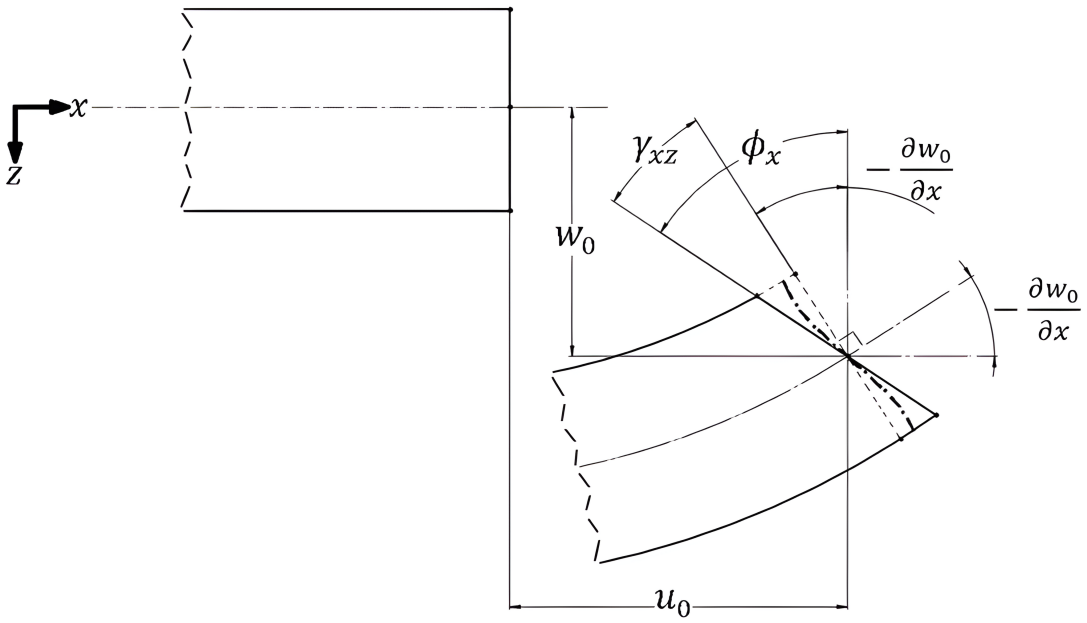

Figure 2.2: Kinematic assumption for FSDT [39].

Note that the in-plane strains vary linearly through the laminate thickness, whereas the transverse shear strains remain constant. In reality, the stress distribution is at least quadratic or parabolic through the laminate thickness [33]. The top and bottom surfaces are stress-free, and the maximum shear stress occurs in the middle of the plate. This issue can be addressed by using higher-order theories such as Second-Order and Third-Order theories, however, this is beyond the scope of this work. Another less expensive solution is to use a shear correction factor κ, which is computed such that the strain energy of the transverse shear stresses matches that predicted by 3D-elasticity theory. Usually a κ of 5/6 is used, however, for laminated plates and shells this correction factor depends on the individual layer properties, the layering scheme, and the loading and boundary conditions [33].

The work of Simo and Fox [40, 41] uses FSDT, but extends it to be geometrically exact. According to Simo and Fox, geometrically exact in the case of shells means:

Geometrically Exact

"Regarding the term *"geometrically exact"*. In any numerical solution procedure, there are two different levels of approximation to be considered: the first level concerns the geometry of the shell and the balance equations governing the motion of the shell; the second level is related to the numerical solution of the governing equations. In the present context, the term *"geometrically exact"* refers to the first level. Accepting the kinematic assumption which defines the class of admissible motions, the geometry of the shell, as well as the balance equations, are treated exactly. In comparison to other numerical treatments of shell theory, one less level of approximation is made" [41].

The above definition for geometrically exact means that the following restriction on the model is removed:

- Small strains and displacements (restriction).

Achieving geometric exactness with respect to the second level is not feasible when using the Finite Element Method (FEM). The primary kinematic assumption in this work involves the shearing of the normal vector, also known as the director. Unlike in Kirchhoff theory [42], where the director remains normal to the mid-surface, here the director is allowed to shear (rotate). Typically, assumptions about the maximum rotation are made, and the kinematics of this shell will be discussed in detail in Chapter 3.

Since composites can fail under small strains [25], Discontinuous Galerkin methods using regular plate theory are still relevant. In 2021, Guarino et al. [32] proposed Discontinuous Galerkin formulations for linear composite plates and shells using higher-order theories, including FSDT, Second-Order, and Third-Order theories. In 2023, Guarino and Milazzo [2] extended this formulation to include nonlinear kinematics. However, this model has not yet been applied to fracture modeling in composite laminates, leaving opportunities for future research.

2.1.2. Layerwise Theory

Since ESL theories cannot accurately capture the 3D stress field, as mentioned earlier, more accurate theories are needed to determine the 3D stress field, particularly in primary aircraft structures. To achieve this, full 3D elasticity theory must be employed; however, this approach is quite expensive. Consequently, the Layerwise theory developed by Reddy [33, 43, 44] has been introduced as an alternative. In the Layerwise theory, each lamina has its own independent displacement field. The Layerwise theory must satisfy the following stress continuity conditions at the interfaces between laminae:

$$\left\{ \begin{array}{c} \sigma_{xx} \\ \sigma_{yy} \\ \sigma_{xy} \end{array} \right\}^{(k)} \neq \left\{ \begin{array}{c} \sigma_{xx} \\ \sigma_{yy} \\ \sigma_{xy} \end{array} \right\}^{(k+1)} \quad \text{and} \quad \left\{ \begin{array}{c} \sigma_{xz} \\ \sigma_{yz} \\ \sigma_{zz} \end{array} \right\}^{(k)} = \left\{ \begin{array}{c} \sigma_{xz} \\ \sigma_{yz} \\ \sigma_{zz} \end{array} \right\}^{(k+1)} \tag{2.5}$$

Since adjacent laminae generally have different orientations, a mismatch in stiffness occurs. Therefore, the second condition implies:

$$\left\{ \begin{array}{c} \varepsilon_{xz} \\ \varepsilon_{yz} \\ \varepsilon_{zz} \end{array} \right\}^{(k)} \neq \left\{ \begin{array}{c} \varepsilon_{xz} \\ \varepsilon_{yz} \\ \varepsilon_{zz} \end{array} \right\}^{(k+1)} \tag{2.6}$$

In all ESL theories, it is assumed that the displacement field is a continuous function of the laminate thickness, whether linear, quadratic, or of higher order. Consequently, the transverse strains at the interfaces are continuous. However, this assumption leads to discontinuous transverse stresses at the interfaces, which is contrary to the requirements outlined in Equation Equation 2.5 [33]. The Layerwise theory addresses this issue by assuming that the displacement field exhibits only C^0-continuity throughout the laminate thickness, rather than C^1-continuity as in ESL theories, as illustrated in Figure 2.3. This approach ensures that while the displacement components remain continuous through the thickness,

their derivatives do not, allowing for discontinuities in transverse strains.

The displacement fields satisfying Equation 2.5 is given by [33]:

$$u(x,y,z,t) = u_0(x,y,t) + \sum_{j=1}^{N} U_j(x,y,t)\Phi_j(z) \tag{2.7a}$$

$$v(x,y,z,t) = v_0(x,y,t) + \sum_{j=1}^{N} V_j(x,y,t)\Phi_j(z) \tag{2.7b}$$

$$w(x,y,z,t) = w_0(x,y,t) + \sum_{j=1}^{M} W_j(x,y,t)\Psi_j(z) \tag{2.7c}$$

Where $U(x,y,0,t)$, $V(x,y,0,t)$ and $W(x,y,0,t)$ are 0 at the mid-surface of the plate/shell. U_j, V_j and W_j are the nodal values of the displacements U, V and W, N is the order of interpolation for the in-plane displacement whereas M is the order of interpolation for the out-of-plane displacement. Thus setting M to zero means that the laminate is inextensible in the transverse direction. $\Phi_j(z)$ and $\Psi_j(z)$ are continuous functions, e.g., one-dimensional Lagrange interpolation functions of the thickness coordinate, that satisfy the condition:

$$\Phi_j(0) = 0 \tag{2.8a}$$

$$\Psi_j(0) = 0 \tag{2.8b}$$

The displacement fields for CLPT and FSDT can be obtained from Equation 2.7 by selecting appropriate variables U_j, V_j and W_j, and functions $\Phi_j(z)$ and $\Psi_j(z)$. E.g, for CLPT [33]:

$$N = 1, \quad M = 0, \quad U_1 = -\frac{\partial w_0}{\partial x}, \quad V_1 = -\frac{\partial w_0}{\partial y}, \quad \Phi_1 = z \tag{2.9}$$

And for FSDT [33]:

$$N = 1, \quad M = 0, \quad U_1 = \phi_x, \quad V_1 = \phi_y, \quad \Phi_1 = z \tag{2.10}$$

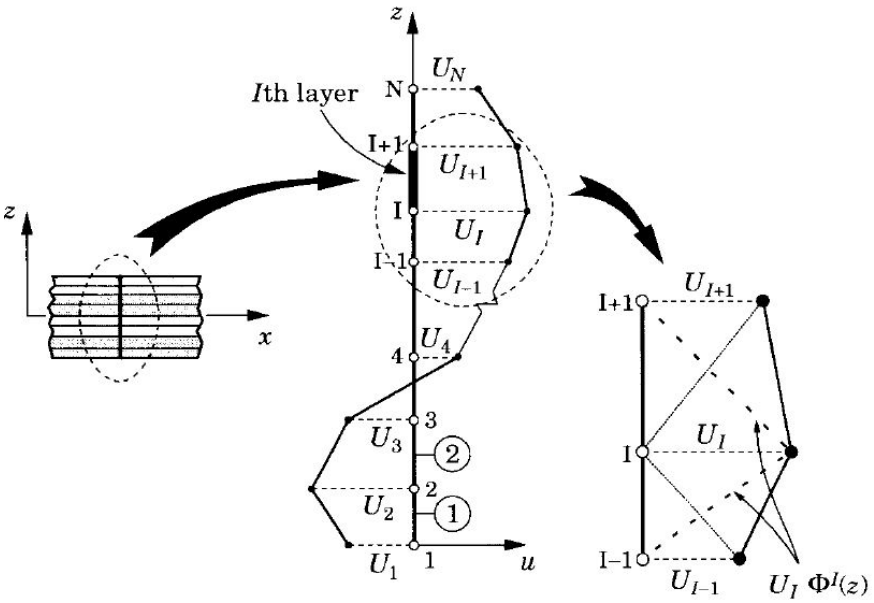

Figure 2.3: Displacement field and linear approximation functions $\Phi_j(z)$ used in the Layerwise theory [33].

2.1.3. Zig-Zag Theory

The main drawback of Layerwise theories lies in their significant computational expense, as the number of layers in a laminate grows, so does the number of degrees of freedom [33, 43, 44]. This means that as the complexity of the laminate structure increases, the computational resources required to analyze it also rise.

Attempts to combine the advantages of Layerwise theory and ESL theories have led to Zig-Zag or discrete-layer theories. The First-Order Zig-Zag Theory (FZZT) introduced by Sciuva [45] in the mid-1980s is a novel class of laminate theory. In this theory, the in-plane displacements within a laminate are assumed to vary linearly across layers and remain continuous throughout the thickness of the laminate. However, what sets FZZT apart is its ability to achieve this continuity while maintaining only five degrees of freedom per node, regardless of the number of layers in the laminate. This accomplishment is made possible by ensuring that the transverse shear stress continuity conditions are analytically satisfied at each interface within the laminate.

The assumed form of the Zig-Zag displacement fields is [33]:

$$u^{(k)}(x,y,z,t) = u_{ESL} + f_1^{(k)}(z)\phi_1(x,y,t) \tag{2.11a}$$

$$v^{(k)}(x,y,z,t) = v_{ESL} + f_2^{(k)}(z)\phi_2(x,y,t) \tag{2.11b}$$

$$w^{(k)}(x,y,z,t) = w_{ESL} \tag{2.11c}$$

Where f_j and ϕ_j are determined such that the displacement and transverse stresses are continuous at the interfaces. $f_i^{(k)}(z)\phi_i(x,y,t)$ are the Zig-Zag displacement terms and describe the cross-sectional distortions that are typical of multi-layered laminates.

In 2000, Cho and Averill [46] developed a refined Zig-Zag plate theory and a corresponding 3D brick element with five degrees of freedom per node. In this theory the laminate can be split into m sublaminates, each sublaminate consists of n perfectly bonded laminae. The displacement fields in the mth sublaminate can be written as:

$$u^{(k)}(x,y,z,t) = u_0(x,y,t) + z\phi_x(x,y,t) + \sum_{j=1}^{k-1}(z-z_j)\phi_{1j}(x,y,t) \tag{2.12a}$$

$$v^{(k)}(x,y,z,t) = v_0(x,y,t) + z\phi_y(x,y,t) + \sum_{j=1}^{k-1}(z-z_j)\phi_{2j}(x,y,t) \tag{2.12b}$$

$$w^{(k)}(x,y,z,t) = w_b(x,y,t)\left(1-\frac{z}{h}\right) + w_t(x,y,t)\left(\frac{z}{h}\right) \tag{2.12c}$$

This theory uses the FSDT superimposed by a continuity term, the shear stress continuity at the kth interface, used to determine ϕ_{1j} and ϕ_{2j}, is expressed as:

$$\sigma_{yz}^{(k)} = \sigma_{yz}^{(k+1)} \quad \text{and} \quad \sigma_{xz}^{(k)} = \sigma_{xz}^{(k+1)} \tag{2.13}$$

ϕ_{1j} and ϕ_{2j} are determined by analytically ensuring continuous transverse stresses at the interfaces between laminae, however, this limits these theories to elastic laminates without damage. It can be showed that ϕ_{1j} and ϕ_{2j} depend on the ratios of shear properties between sublaminates and their individual shear deformations. It is evident that the assumed displacement field in Zig-Zag theories essentially consists of an ESL theory with an additional term to ensure interlaminar continuity. Another key observation is that the second assumption of the Kirchhoff hypothesis is relaxed, transverse deformations is allowed. w_t and w_b are the transverse deflections of the top and bottom surfaces of the mth sublaminate, respectively. Consequently, the displacement component $w^{(k)}$ varies linearly through the sublaminate thickness whereas $u^{(k)}$ and $v^{(k)}$ vary piecewise linearly through the thickness.

2.1.4. Global-Local Theory

In 1999, Williams [47] formulated the global-local theory, based on a dual-length-scale displacement approach. This formulation includes layer displacement fields with global and local components, allowing for flexible orders and functional forms. The novelty of this theory is the consideration of different length scales, which is the main difference from existing theories. In the analysis of laminated plates, this dual length-scale approach incorporating both global and local displacement fields offers a computationally efficient alternative to Layerwise theories [4, 5, 47]. This theory adds additional unknowns to the system, albeit not as many as the Layerwise methods, it is a compromise between Layerwise and ESL methods. In other words, layers of interest can have a Layerwise displacement field whereas the rest of the laminate—e.g., a group of laminae with the same orientation—has a computationally less expensive ESL field.

The displacement field for the kth layer is assumed to be [4, 5, 47]:

$$u^{(k)}(x,y,z,t) = \sum_{r\in\bar{\mathcal{P}}} \bar{U}_r(x,y,t)\bar{\phi}_r(z) + \sum_{s\in\tilde{\mathcal{P}}^{(k)}} \tilde{U}_s^{(k)}(x,y,t)\tilde{\phi}_s^{(k)}(\bar{z}) \tag{2.14a}$$

$$v^{(k)}(x,y,z,t) = \sum_{r\in\bar{\mathcal{P}}} \bar{V}_r(x,y,t)\bar{\phi}_r(z) + \sum_{s\in\tilde{\mathcal{P}}^{(k)}} \tilde{V}_s^{(k)}(x,y,t)\tilde{\phi}_s^{(k)}(\bar{z}) \tag{2.14b}$$

$$w^{(k)}(x,y,z,t) = \sum_{r\in\bar{\mathcal{P}}} \bar{W}_r(x,y,t)\bar{\phi}_r(z) + \sum_{s\in\tilde{\mathcal{P}}^{(k)}} \tilde{W}_s^{(k)}(x,y,t)\tilde{\phi}_s^{(k)}(\bar{z}) \tag{2.14c}$$

The indices r and s vary over the ranges $r \in [\bar{J}_{\min}, \bar{J}_{\max}]$ and $s \in [\tilde{J}_{\min}, \tilde{J}_{\max}]$. The parameters $\bar{J}_{\min}$ and $\bar{J}_{\max}$ correspond to the minimum and maximum orders of the global displacement expansion, while $\tilde{J}_{\min}$ and $\tilde{J}_{\max}$ indicate the limits of the local displacement expansion within a layer. The global coordinates are defined as x, y, and z, with the reference plane established at the laminate's mid-surface ($z = 0$). The local coordinates for a layer, which can include multiple laminae, a single lamina, or a sublamina region, are represented by x, y, and $\bar{z}$, satisfying the condition $z_{k-1} \le \bar{z} \le z_k$ [47].

The following definitions are chosen [3]:

$$\bar{\phi}_r := z^r \quad \text{and} \quad \tilde{\phi}_s^{(k)} := z^s \tag{2.15}$$

The terms included in the global expansion and the local expansion for the kth layer are defined by the sets $\bar{\mathcal{P}}$ and $\tilde{\mathcal{P}}^{(k)}$. For example, if $\bar{\mathcal{P}} := \{0,1,2,3\}$, the global expansion becomes a complete cubic polynomial in z. Meanwhile, if $\tilde{\mathcal{P}}^{(k)} := \{1\}$, the local expansion is limited to a single linear term.

2.2. Modeling Damage in Composites

As previously explained, damage in composites can be classified into two main categories: interlaminar damage and intralaminar damage. To model these types of damage, various finite element modeling techniques are employed, including the VCCT, CZM, and XFEM, as illustrated in Figure 2.4. Within the scope of XFEM, alternative techniques such as the PNM and FNM are also encompassed. The XFEM can model both types of damage: intralaminar damage by simulating cracks within laminae, and interlaminar damage by simulating cracks between laminae. However, they are often used in conjunction with methods like CZM and VCCT to model crack propagation [48].

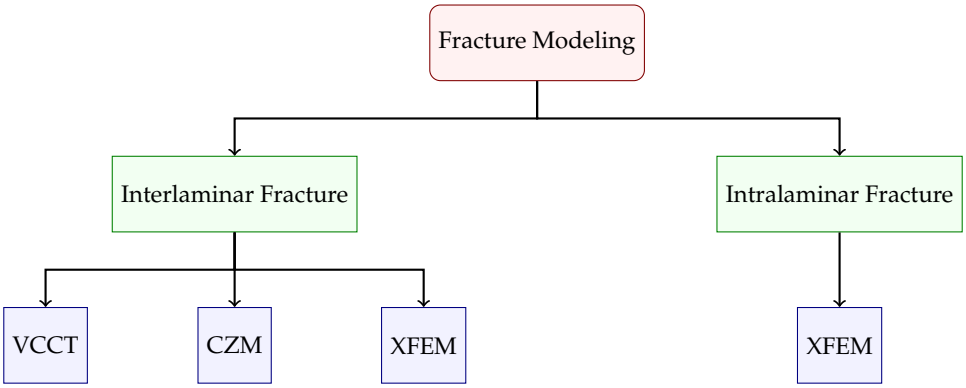

Figure 2.4: Flowchart of fracture modeling methods (adapted from [48]).

2.2.1. Interlaminar Damage

In 2000, Sprenger et al. [34] developed a methodology to model delamination in composite structures through the use of 3D-shell elements, shell elements, with a finite-thickness interface element. The authors introduced a modified eight-node brick element, these elements are then used to model the individual laminae. To model delamination, Sprenger et al. extended Hashin's criterion, incorporating a softening law characterized by a damage parameter that describes the slope of the softening curve. Due to the use of solid elements, the complex stress states at element interfaces was able to be captured more effectively, based on the DCB test results (see Figure 2.5). There seems to be a reasonably good agreement between the developed eight-node element and the experimental results. However, the results were found to be too stiff, especially in the initiation of damage. Standard 3D elements with 27 nodes have also been used to model the laminae, and a much better match can be seen. The authors suggest this could be due to the displacement elements used to discretize the interface layer, these elements do not effectively capture the detailed stress variations inside interface layer [34].

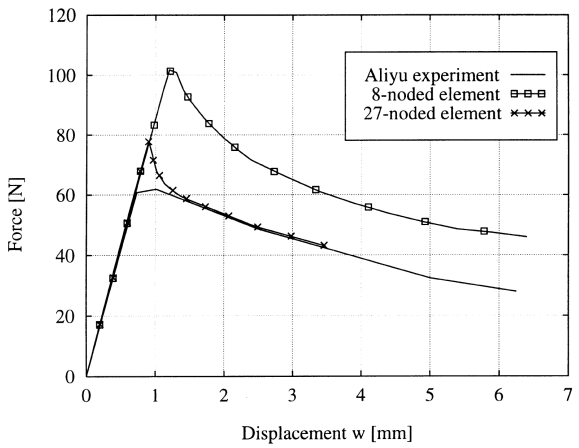

Figure 2.5: Load versus displacement of DCB test: experimental and numerical results of the proposed eight-node shell element and quadratic 27-node volume elements for modeling the laminae. The 27-node element shows much better agreement with experimental results [34].

Later, in 2008, Balzani and Wagner [14] developed an isoparametric hexahedral finite element model to simulate delamination in unidirectional fiber-reinforced composites using a cohesive zone approach. The model incorporates two constitutive laws to represent delamination behavior: one with linear softening and another with exponential softening. The composite strips are modeled using quadrilateral FSDT shell elements from Subsection 2.1.1 and damage is modeled by utilizing a solid-like interface element, characterized by a very thin initial thickness, to simulate the fracture process accurately. Note that the area under the curve in Figure 2.21b is now divided by the initial thickness instead of the initial length. The exponential softening law is designed to initiate delamination only under tensile normal stresses and includes a penalty term to prevent crack face interpenetration. Balzani and Wagner validated their model through numerical examples, including the DCB test (see Figure 2.6), demonstrating good agreement with the same experimental data as in Figure 2.5 and analytical solutions. The exponential softening model is noted for its better convergence compared to the linear softening model, using a realistic Mode I interface strength σ_n^0 and number of elements n. The linear softening model failed to converge using the same strength and mesh as the exponential softening model. Finally, as expected linear unloading to the origin is observed.

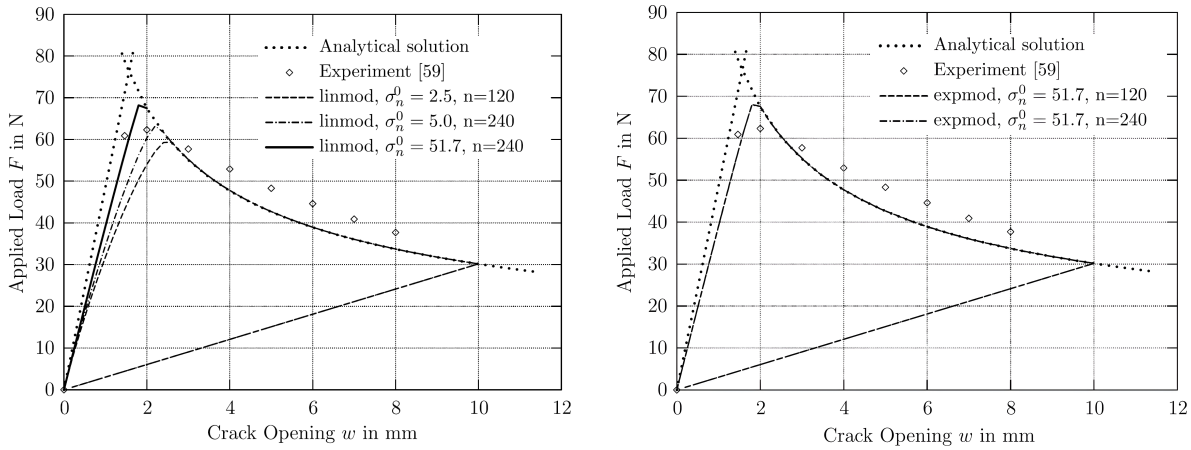

(a) Load-displacement curves of DCB test using the bilinear model: experimental and numerical results.

(b) Load-displacement curves of DCB test using the exponential model: experimental and numerical results.

Figure 2.6: Load versus displacement of DCB test where σ_n^0 is the Mode I interface strength and n is the number of elements in the mesh [14]. The exponential softening curves show better convergence compared to the bilinear ones. This can be seen in the solid black curve for linear softening, where convergence stops for similar properties as the exponential curve.

In 2014 and 2015, Versino et al. [4, 5] proposed both linear (small deformation) and nonlinear (finite deformation) shell models utilizing the DG/CZM method in the thickness direction for composites. The Discontinuous Galerkin fluxes effectively maintain interlaminar continuity in perfectly bonded laminates, allowing for a seamless transition to a delaminated state. The Discontinuous Galerkin method ensures numerical consistency in representing interfacial debonding by utilizing the interior penalty method from [28]. This study uses the Global-Local framework (see Subsection 2.1.4) allowing for the superposition of global and local displacement fields which could be used to model the coupling between effects related to different length scales, e.g., coupling between interlaminar and intralaminar damage. The performance of this formulation was validated through several numerical examples, including: perfectly bonded and delaminated surfaces and the DCB test. The results for the DCB test, see Figure 2.7, demonstrate the current framework's capability to accurately capture delamination initiation and propagation using the DG/CZM method. However, while the director is utilized in this work, only the displacement degrees of freedom are considered. The rotation of the director is neither determined nor updated as the shell deforms. Additionally, this approach only accounts for opening displacements (Mode I), neglecting the influence of shear forces on delamination growth.

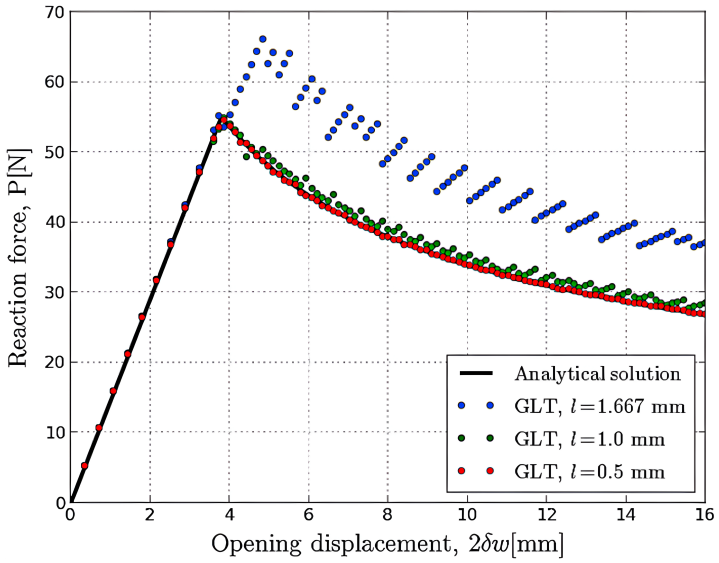

Figure 2.7: Load versus displacement of DCB test for several element lengths l: experimental and numerical results using the proposed four-node interface element [5]. Convergence towards analytical solution is observed as the mesh is refined.

2.2.2. Interlaminar and Intralaminar Damage

In 2008, Bruno et al. [21] developed a methodology to investigate the interaction between interlaminar and intralaminar damage mechanisms in fiber-reinforced composite laminates. Note that with interaction is meant taking into account intralaminar damage at the integration points of the laminae to calculate the ERR. The theoretical model is based on a thermodynamic framework, integrating both CDM and Fracture Mechanics. This dual approach allows for the simulation of homogenized distributed microcracks (intralaminar damage) and interfacial delamination processes (interlaminar damage) respectively. The laminate description employs the FSDT plate theory alongside an interface methodology. This combination ensures accurate ERR mode mix calculations while maintaining low computational costs. The numerical modeling is implemented through a finite element approach where linear elastic interface elements with high stiffness properties are used to simulate the mechanical behavior between laminate layers. Numerical results are provided for various loading conditions, including pure mode I, mode II, and mixed-mode. These results highlight how intralaminar damage mechanisms intensify ERR, thus accelerating growth of the delamination front. For example, in a mixed-mode loading condition involving a DCB specimen, the ERR components normalized over their critical values showed that intralaminar damage mechanisms lead to a higher ERR prediction compared to Linear Elastic Fracture Mechanics (LEFM), consequently crack growth is predicted to occur sooner. Additionally, sensitivity analyses in terms of the ERR and comparisons with the LEFM framework were performed, see Figure 2.8. These analyses demonstrate that while LEFM provides realistic results for laminates with small fiber orientation angles, hence minimal intralaminar damage, it underestimates the ERR for structures subjected to transverse or shear loads, where intralaminar damage mechanisms are significant. The maximum percentage error observed in these predictions ranged from 20-25%.

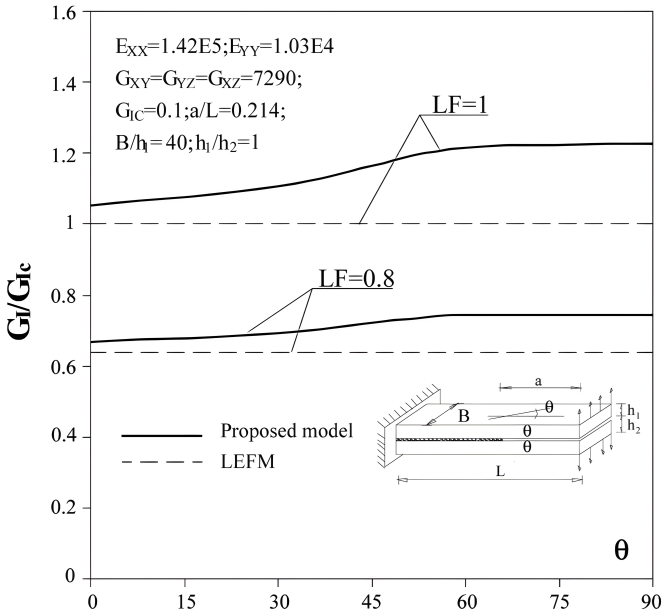

Figure 2.8: Normalized value of the ERR for Mode I versus the layup angle θ for the laminate $[\theta_2/\theta_2]$ under two Load Factors (LF), comparing both LEFM and the proposed formulation. As the angle increases, intralaminar damage increases, thus increasing the ERR. Effectively this lowers the load at which damage occurs [21].

In 2011, van der Meer et al. [22] developed a computational framework to model the progressive failure of composite laminates, integrating several different techniques to accurately simulate interlaminar and intralaminar damage mechanisms. For matrix cracking, the PNM, a variation of the XFEM, was employed. This method allows for a mesh-independent representation of matrix cracks as straight discontinuities within the displacement field, effectively capturing the progression of cracks within the laminae and providing a detailed simulation of intralaminar damage. Interlaminar damage, specifically delamination, was modeled using interface elements designed to simulate the separation between laminae. The delamination model incorporates a cohesive zone approach with a damage law that uses linear softening to relate traction to displacement jumps. A fine mesh is needed to capture the cohesive zone for delamination properly. If this requirement is not met, an oscillatory response is found and convergence problems arise before final failure [17, 49], see Figure 2.9. The reason for this, as stated in [17], is that the fracture energy released increases for larger elements.

Phantom Node Method

The PNM is used to model discontinuities in finite element analysis by introducing additional "phantom" nodes. Each original node is paired with a phantom node, thus doubling the number of nodes in the element. When a crack intersects an element, these additional nodes are activated to form sub-elements on each side of the discontinuity. Stiffness and force calculations are performed only for the active parts of these sub-elements [22, 50]. The PNM is shown to be equivalent to the XFEM with Heaviside enrichment for strong discontinuities (cracks) [50].

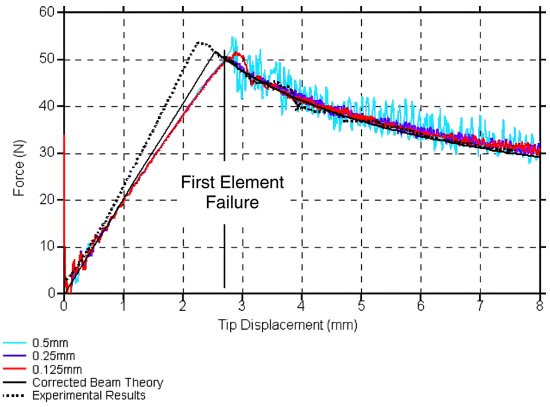

(a) Load-displacement curves of DCB test using small element sizes: minimum of two in process layer.

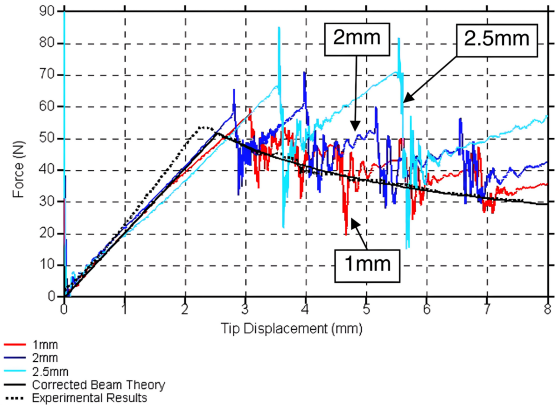

(b) Load-displacement curves of DCB test using large element sizes: less than two in process layer.

Figure 2.9: DCB load-displacement curves in relation to the number of interface elements within the numerical cohesive zone. It is observed that the response becomes oscillatory when less than two elements have been used in the process/cohesive layer [17]. A convergence study is needed to match the response.

This work makes two simplifications in order to limit the computational cost. First, analyses are performed in a plane stress state instead of explicitly modeling the thickness. Furthermore, out-of-plane and bending deformations are not part of the model. As a result the interface elements can only capture shear delamination since out-of-plane displacements are neglected. The second simplification is that the mesh is only refined in part of the region where damage is allowed, outside of this region no damage can happen and individual layers are rigidly tied together. The elastic stiffness of the interface elements is calibrated to represent the through-the-thickness shear deformation of the laminae, utilizing the in-plane shear stiffness and ply thickness. This choice simplifies the model since the stiffness is not orthotropic and does not depend on the fiber direction. Fiber failure was addressed using a continuum damage model with isotropic softening. This model tracks the maximum strain in the fiber direction and initiates damage when the strain exceeds a critical threshold. An exponential softening relation is then used to simulate fiber failure. The effectiveness of the computational framework was verified through open-hole tension and Compact Tension tests, the results of the Compact Tension test are given in Figure 2.10.

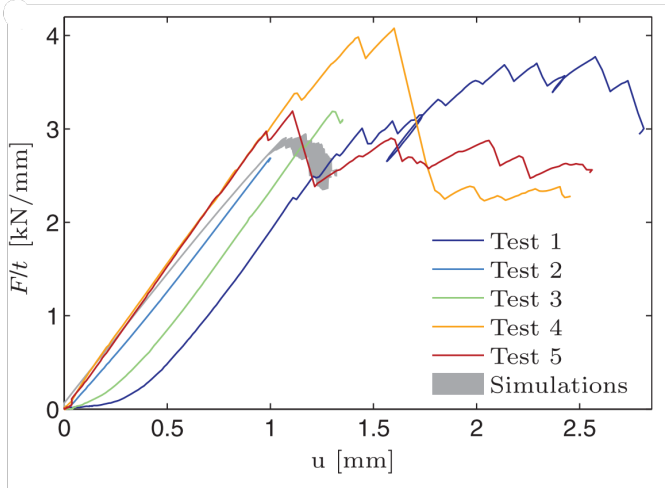

Figure 2.10: Compact Tension test load-displacement curves: simulations for $[45/90/-45/0]_{\infty}$ laminates with varying crack spacing (defined as the normal separation between pre-existing cracks), and experiments for $[45/90/-45/0]_{4s}$ laminates. The results match before damage initiation but not after, when the experimental tests show a higher load. The authors suggest this could be due to fiber bridging, which is not taken into account in the damage model [22].

The results for the simulations are obtained by varying the crack spacing, defined as the normal separation between pre-existing cracks. New cracks can only be added when this separation is larger than the

specified crack spacing. These result show that initially the numerical and experimental results match really well, however, not after damage has been created. The authors suggest this could be due to the fiber damage evolution law, which does not take into account fiber bridging, resulting in the fracture toughness being much lower compared to the experimental results.

In 2012, Bouvet et al. [23] used the CZM to simulate both interlaminar and intralaminar damage, and the permanent indentation (plastic dent) in composite laminates subjected to low velocity impacts. The methodology integrates three primary damage types observed during impact: matrix cracking, fiber failure, and delamination, each addressed in this model. Intralaminar damage, or matrix cracking is simulated using interface elements based on Hashin's failure criterion. These elements represent the cracks that propagate through the thickness of the ply. The model employs a mesh of longitudinal strips with one volume element in the ply thickness, connected by zero-thickness interface elements normal to the transverse direction. This setup captures the discontinuity created by matrix cracks, which is essential for accurately simulating the impact damage morphology. However, the model simplifies certain aspects by assuming instantaneous propagation of matrix cracks through the ply thickness and neglecting small or angled matrix cracks, focusing instead on the largest possible cracks that run through the entire thickness. Fiber failure is simulated using a CDM approach in the volume elements, the model applies a failure criterion to determine the initiation and progression of fiber failure within the composite material. This method ensures that the reduction in strength due to fiber breakage is represented in the simulations. Interlaminar damage is simulated using zero-thickness interface elements based on fracture mechanics. This approach captures the separation between laminae, which are meshed separately. Damage initiation and propagation occurs at the interfaces between the meshed strips representing individual laminae. Experimental observations have shown that matrix cracking debris can block crack closure, contributing to permanent deformation. This model includes this phenomenon by introducing a "plastic-like" behavior in the interface elements, which models the effect of the debris by limiting the closure of the interface and is supposed to capture the plastic indentation observed in experiments. The model's validity is assessed through numerical tests in the commercial software ABAQUS/Explicit [51], and the numerical impact force versus displacement and time are compared with experimental data, see Figure 2.11. The validation also focuses on the simulated shape of the deformation, e.g., the delaminated first interface on the opposite side of the impact as can be seen in Figure 2.12.

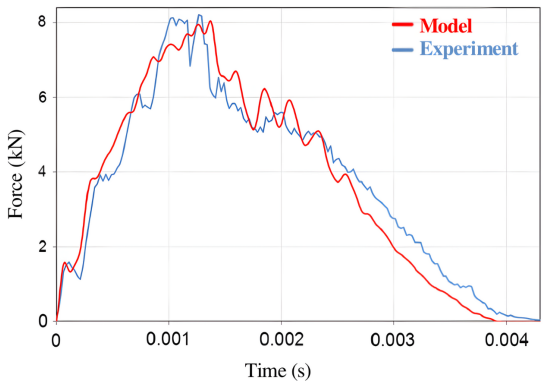

(a) Experimental and numerical curves of impact force versus time.

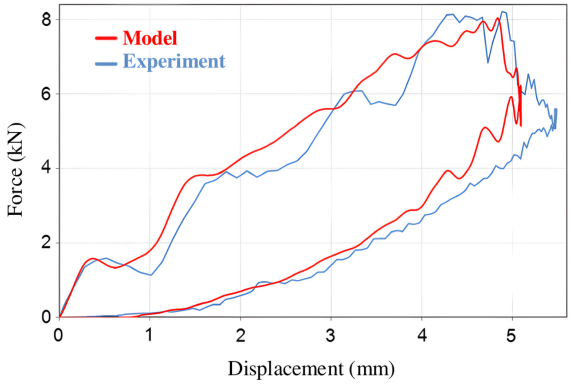

(b) Experimental and numerical curves of impact force versus displacement.

Figure 2.11: Experimental and numerical curves of impact force versus time and displacement, a reasonably good match is observed [23].

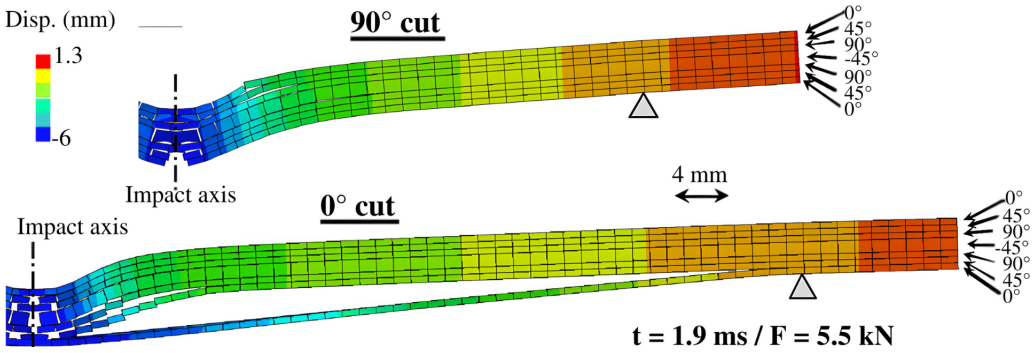

Figure 2.12: Maximum deformed mesh during 25 Joule impact showing matrix cracks and delaminations at two cuts: 0 and 90 degrees [23].

Floating Node Method

In the FNM, "floating nodes" are introduced into the element; these nodes are termed "floating" because they do not require predefined position vectors like regular nodes. Once a strong discontinuity is detected, the element is split into sub-elements based on the intersection coordinates of the crack with the element boundaries. Unlike the PNM, this approach directly uses these intersection coordinates to define nodal positions for each sub-element, thereby simplifying the mapping and integration process to be as straightforward as remeshing [50].

In 2015, De Carvalho et al. [24] proposed a combination of the FNM, proposed by Chen et al. [50] in 2014, with the VCCT to model Delamination Migration in cross-ply tape laminates. This approach is designed to model delamination migration, which involves the propagation of a delamination from one interface to another through matrix cracks. By integrating delamination, matrix cracking, and their interactions within a single element utilizing the FNM, this method attempts to represent the kinematics involved in these processes. In this method, 2D elements with 4 real nodes and 16 floating nodes are used, the floating nodes are assigned to edges or the internal volume of the elements. The floating nodes do exist from the start of the simulation but are inactive until damage is created, at this time they are assigned to the strong discontinuity/crack. This is a key aspect of this methodology, its ability to determine the onset and path of migration, independent of the mesh. This is achieved by explicitly representing both delamination and matrix cracks within the elements. The ERRs at each crack position are calculated using VCCT using the force required to keep the crack closed, assuming the crack propagates in a self-similar fashion along its forward projection. This is an important assumption since it allows for the determination of the force and the relative displacements, thus being crucial for the application of VCCT. The delamination growth is assumed to grow when the Critical Energy Release Rate (CERR) of the interface is equal to a failure criterion taking into account Mode I and Mode II release rates. Similarly, matrix cracks are assumed to follow a mode I propagation path in the transverse isotropy plane, perpendicular to the fibers, using their own failure criterion.

Virtual Crack Closure Technique

The most prominent LEFM approach is the VCCT. The VCCT uses an energy-based criteria to predict delamination propagation along paths aligned with element edges. A limitation of this technique is that the prediction of damage initiation is not possible and needs predefined cracks to work [14].

The interaction of damage in this framework is demonstrated through the delamination migration test, which serves as a validation for the proposed approach. The results from the delamination migration test simulations show a reasonably good agreement with experimental observations, see Figure 2.13. The study found that maximum load is primarily influenced by load-offset L (distance between applied load and initial delamination tip), initial delamination length, and interface toughness, as these factors directly affect the delamination fracture criterion. On the other hand, migration location is affected

mainly by load-offset and matrix fracture toughness. The dependency on load-offset was anticipated since it alters the location where the shear traction sign changes, thereby controlling the migration location. Additionally, a sensitivity analysis revealed that increasing the baseline fracture toughness of the matrix changes the migration onset location by increasing the distance between the migration onset and the initial delamination tip. However, decreasing the baseline matrix fracture toughness does not affect the migration location.

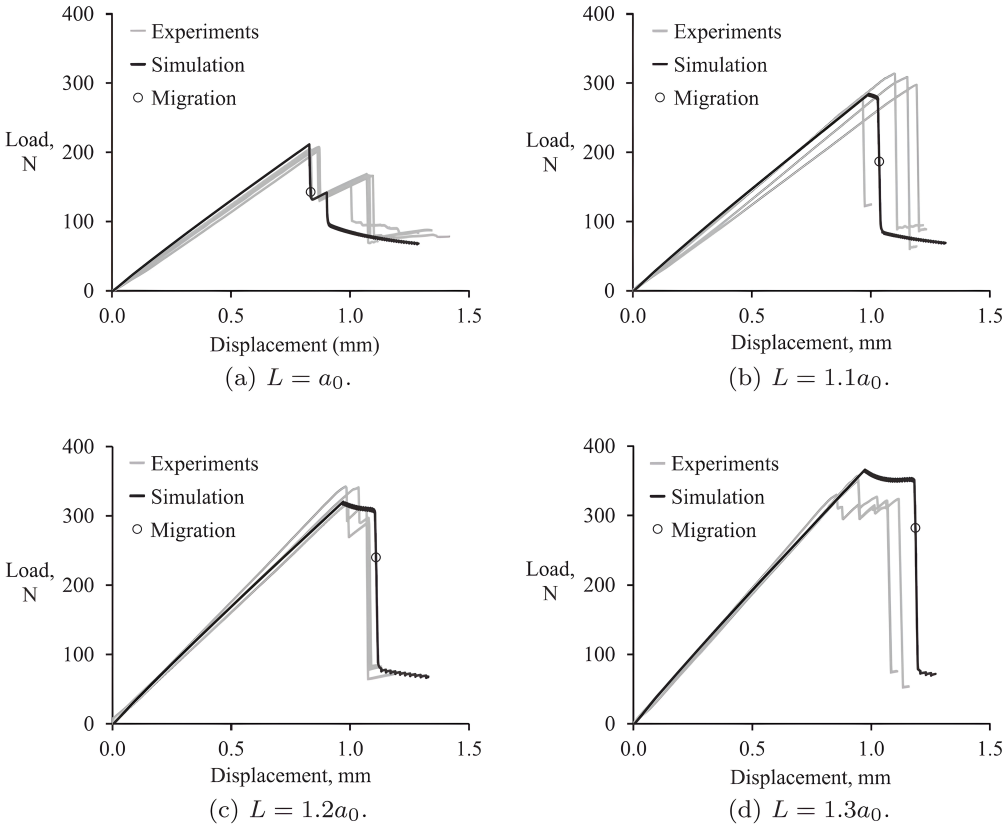

Figure 2.13: Load-displacement curves for several load offsets L (distance between applied load and initial delamination tip), where a_0 is the initial delamination length, and the moment of delamination migration is indicated after unstable delamination growth (sharp drop in load) [24].

In 2015, Vigueras et al. [25] used XFEM with the CZM to model damage in composites. XFEM was chosen for its ability to initiate cracks independently of the mesh, avoiding the need for remeshing, or predefined fracture paths. For interlaminar failure, an intrinsic CZM was used. This model was calibrated using experimental data, specifically DCB tests. This allowed the model to capture the progressive damage and energy dissipation during delamination. In contrast, intralaminar failure was modeled using an extrinsic CZM embedded within the XFEM framework. As explained previously, this extrinsic approach activates cohesive elements only upon crack initiation. The crack propagation was driven by a modified Rankine tensile stress criterion, which dictated the orientation of the cracks based on local stress conditions. This combined XFEM/CZM method allowed for the modeling of matrix cracks, as well as their interaction with delamination. The XFEM enrichments, which add additional degrees of freedom to capture the crack geometry, were applied locally, limiting their effects to elements near the crack. This localized enrichment approach minimized the impact on computational resources and allowed the rest of the domain to use standard FEM formulations. The composite structure was partitioned into subdomains, each assigned to a processor. Because the XFEM enrichments are defined locally, the model avoided unnecessary global communication between processors. The implementation demonstrated good parallel scalability based on a speed-up analysis, with the model showing near-linear scalability in both explicit and implicit XFEM simulations up to 2048 processors.

eXtended Finite Element Method

The XFEM is used to model discontinuities in finite element analysis by enriching standard shape functions with additional terms that account for cracks or other discontinuities. Unlike traditional methods, XFEM does not require the mesh to conform to the crack geometry. Instead, special enrichment functions, such as the Heaviside function for strong discontinuities, are introduced. Elements are divided into standard elements, blending elements, and reproducing (cracked) elements. This allows XFEM to model cracks accurately without re-meshing as the crack propagates [52].

In 2018, Bazilevs et al. [11] introduced a multi-layer approach for the simulation of interlaminar and intralaminar damage in composite laminates, integrating Kirchhoff-Love shell theory with cohesive zone modeling techniques. The core of their approach is the Kirchhoff-Love thin shell model, which is used to model each lamina independently, connected by interface elements that allow for transverse shear deformation of the entire laminate. The reason for selecting Kirchhoff-Love shells is to avoid the transverse shear locking of FSDT, however, the rotational degrees of freedom are neglected which means it cannot be used with large deformations. To simulate intralaminar damage, the authors employ CDM, thus modeling the equivalent effects of various damage modes, such as matrix cracking, fiber breaking, and fiber-matrix debonding, at the continuum level. These damage mechanisms are implemented to degrade the original elastic properties of the material based on a linear failure criteria, providing a realistic simulation of damage initiation and progression within the laminates. Furthermore, the authors utilize a zero-thickness cohesive-interface element to model delamination and transverse shear in the entire laminate, even though shear is neglected in laminae. The proposed interface element is actually a penalty contact formulation enriched with a Mixed-Mode cohesive law combining opening (Mode I) and shear (Mode II) modes. While allowing for modeling of the delamination process, a separate interpenetration constraint is needed after the elements have failed. Validation of the proposed framework is performed using standard tests such as the DCB test, the results can be seen in Figure 2.14. The load-displacement curves are shown for three simulations and LEFM with a reasonably good agreement. The three simulations are performed using different interface strengths t_n^0, each progressively stronger, which delays the point of damage initiation. Additionally, the model has been compared to FSDT. The transverse shear of the laminate is modeled by adjusting the cohesive penalty stiffness, essentially allowing the layers to shear along each other. When the stiffness is infinite, no transverse shear is modeled because the Kirchhoff assumption is enforced throughout the thickness. However, the authors suggest that with a non-zero stiffness, shear is effectively modeled. Using the appropriate penalty stiffness, a good agreement with FSDT was achieved. However, this does not actually model shear so its general accuracy remains doubtful.

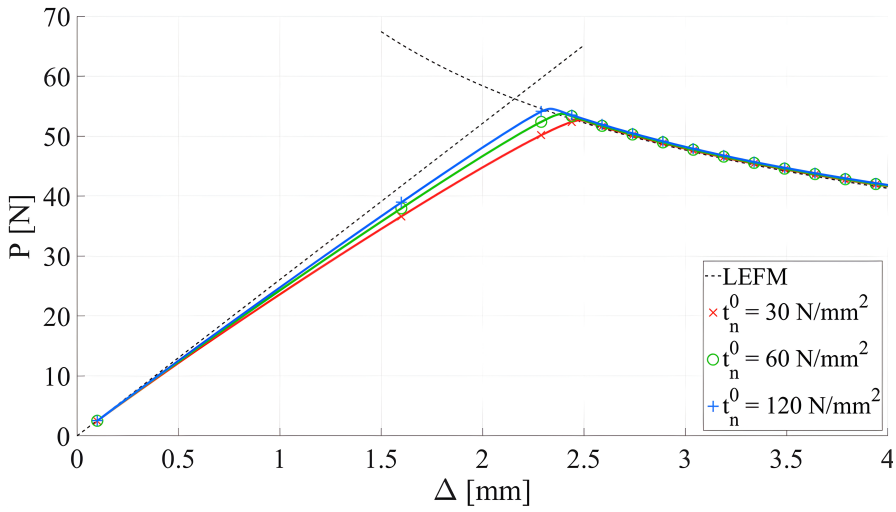

Figure 2.14: Load-displacement curves for the DCB test, obtained for several interface strengths t_n^0 and LEFM, are presented. A reasonably good agreement can be observed; as expected, higher interface strengths delay the initiation of damage without significantly affecting delamination propagation [11].

In 2019, Yun et al. [26] developed a progressive damage model to reflect the interaction between delamination and intralaminar cracks in Fiber-Reinforced Polymer (FRP) laminates. This methodology integrates a CDM model with a CZM to simulate and predict the fracture behavior and ultimate load of composites under quasi-static loading conditions. This study models intralaminar cracks using a CDM approach, and for delamination, a CZM with a mixed bilinear law is employed. The authors state that when using both CDM for intralaminar failure and CZM for interlaminar delamination, the interaction between interlaminar and intralaminar damage is usually not captured, e.g., matrix cracks causing delaminations or the the migration of delaminations as mentioned before. Usually the CZM combined with CDM is not able to resolve the high stresses at the tip of a transverse crack in numerical simulations since elements where the transverse crack is predicted, soften without accurately capturing the stress field at the interface [26]. Additionally, attempts to visualize the crack path in off-axis tensile test simulations show that this approach does not explicitly represent the kinematics of the cracks since only the constitutive response is degraded [53]. Finally, a disadvantage of using a CZM together with CDM is that failure is modeled less accurately because the stress concentration caused by matrix cracks cannot be captured when reaching an interface between cohesive interfaces and solid elements [24].

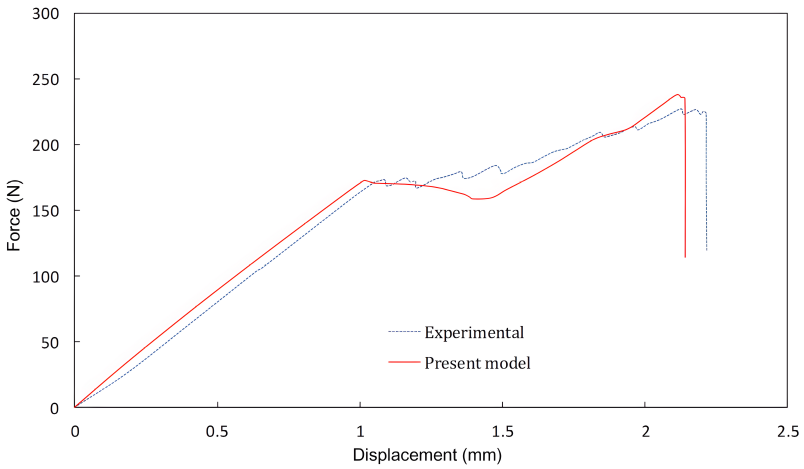

Figure 2.15: Simulated and experimental load-displacement curves for the delamination migration problem [26]. A similar drop in load as in [24] is observed at the point of migration.

This approach is the first to effectively capture interactions of interlaminar and intralaminar damage modes in composites using the CZM and CDM frameworks. However, to do this with the standard CDM would not be possible based on the earlier mentioned limitations. The CDM must thus be able to consider the direction of the matrix crack next to the degradation of the constitutive model. For interlaminar damage, a Mixed-Mode TSL, combining Mode I and Mode II, is used. Interaction is included by considering the degradation of the interlaminar CERR following intralaminar damage such as fiber and matrix damage. It is assumed that the surface in which matrix cracking occurs is parallel to the fiber direction, the angle of the surface's normal vector with the direction perpendicular to this surface is α is referred to as the crack direction parameter. This parameter depends on the stress components perpendicular to the fibers. The damage parameter and the new direction parameter are updated iteratively as damage is created, ensuring that the propagation of intralaminar cracks is captured. The degradation of the interlaminar fracture energy following intralaminar failure is also considered, allowing the model to reflect the interaction between different damage mechanisms effectively. To model this, a meso-level FEM is developed using the commercial software ANSYS [54] to predict the progressive failure of intralaminar and interlaminar damage, as well as their interaction in laminated composites. The composite layers are meshed with structural solid elements, while the interfaces between layers are modeled with cohesive zone elements from the ANSYS element library. If an element is damaged, the corresponding damage variable and crack direction are calculated, leading to stiffness degradation as defined by the damage evolution model. Numerical simulations showed good agreement with experimental data, particularly in terms of the load-displacement curve and the point of delamination migration, corresponding to the sharp load drop, see Figure 2.15. The model

consists of only 0° and 90°-degree plies with a pre-crack defined at the interface between 0° and 90°-degree laminae. Initially, the delamination grows along the pre-crack direction. Subsequently, the crack propagates into the adjacent 90°-degree lamina as a matrix crack. Delamination growth is stopped until the point of migration, after which the load drops and it continues along the adjacent interface.

2.2.3. Cohesive Zone Model

Zero-Thickness Cohesive Elements

In 1960, Dugdale [55] introduced the idea that uniform tractions, equal to the yield stress, are transmitted through a narrow yield zone ahead of a crack tip in materials that exhibit plastic behavior. Independently, in 1962, Barenblatt [56] introduced cohesive forces to capture the influence of interatomic interactions in polycrystals. This perspective views fracture as a gradual process, wherein separation occurs across an extended crack tip or cohesive zone, countered by cohesive forces, as seen in Figure 2.16. This conceptualization of fracture allows for the integration of essential fracture parameters, such as maximum cohesive traction and fracture energy—the area under the cohesive law of the material—into the analysis [20, 57]. An appealing aspect of this approach is its flexibility, as it does not assume a specific constitutive response in the bulk material, nor does it rely on predefined assumptions regarding the extent of crack growth or the shape and location of successive crack fronts [20].

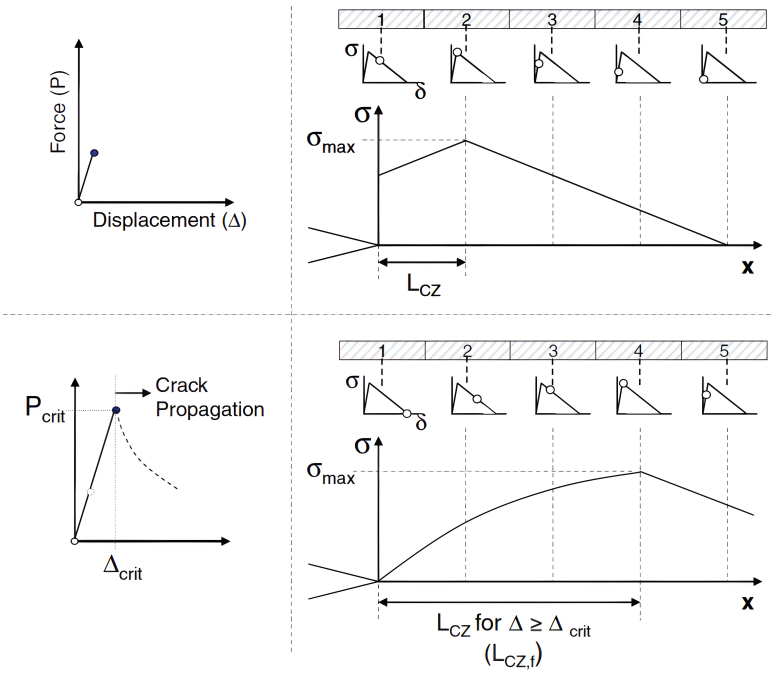

Figure 2.16: Gradual development of fracture surface and numerical cohesive zone length [17].

The parameter G, representing the ERR, serves as a widely utilized parameter to describe delamination behavior in composite structures. It quantifies the energy released per unit area associated with the newly opened crack surface. In the context of predicting delaminations, a popular approach relies on fracture mechanics: the ERR G is compared with the critical value G_c, and delamination is identified when all interlaminar stresses reach zero [34]. To accurately capture energy dissipation during damage evolution and prevent mesh-size dependency in the numerical solution, the slopes of the softening laws are determined as functions of both the fracture toughness G_c and the characteristic length L [58]:

$$G_c = L \int_0^{\varepsilon_f} \sigma(\varepsilon)\, d\varepsilon \tag{2.16}$$

CZMs offer a method to characterize materials displaying strain-softening behavior. At their core lies the assumption that alongside the actual crack, there forms a fictitious crack, often termed the process zone, extending from the real crack [16, 59]. Within this zone, the material, despite undergoing damage, retains the ability to transmit stresses. Unlike LEFM, which presupposes an instantaneous drop in stress to zero upon crack initiation, CZMs recognize a gradual decline in stress as the crack opens [16]. This decline continues until a critical displacement is reached, at which point the interaction ceases. In other words, the CZM is a representation of the separation process occurring right before the tip of

the crack, until reaching a critical opening displacement, at which point new free surfaces are created [19]. CZMs relate the inelastic TSL, which describes the degradation response, to a specific reference surface [16]. This reference surface is typically the interface between two adjacent elements, as shown in Figure 2.18. Finite elements that utilize this approach are often called zero-thickness or surface-like cohesive elements, as they relate interfacial tractions to the relative interfacial displacement. Numerous CZMs utilizing this surface-like element structure have been suggested, often accompanied by diverse descriptions of the TSL [60]. Some of these TSLs can be seen in Figure 2.19. Schellekens and Borst [61] were one of the first the first to model delaminations using interface elements, they discretized the laminae by introducing plane strain elements with cubic interpolation functions and placed interface elements between the laminae.

A general intrinsic cohesive element comprises the following three features, see Figure 2.17 [17]:

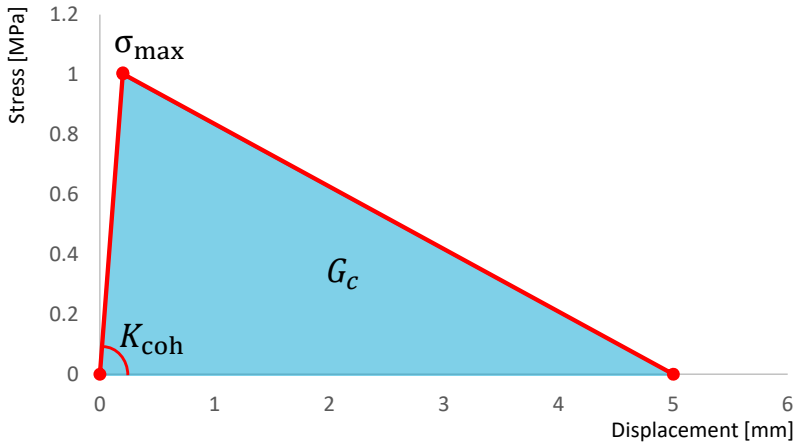

Figure 2.17: Features of Cohesive Zone Elements with example axis values.

1. An initial elastic region (K_{coh}) until reaching a maximum stress ($\sigma_{\max}$), representative of the interfacial strength.
2. A softening region until reaching zero stress, indicating element failure.
3. The total area bounded by the curve equals the fracture toughness (G_c) of the material.

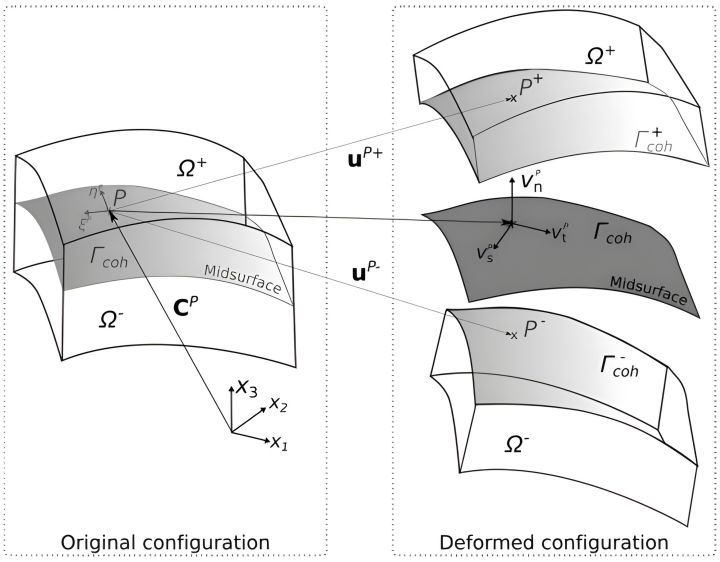

Figure 2.18: Zero-thickness or surface-like cohesive zone element between two bulk elements [62].

In 2019, Lu et al. [63] studied the effect of the three above-mentioned features on the CZM: the penalty stiffness (K_{coh}), cohesive strength ($\sigma_{\max}$), and fracture toughness (G_c). The penalty stiffness is a numerical parameter that governs the initial elastic behavior of the cohesive elements. An appropriate K_{coh} ensures that the interface behaves correctly under elastic deformation. If it is too low, the structure's compliance increases artificially, leading to inaccurate predictions. Conversely, if it is too high, it can cause numerical difficulties, such as non-convergence and an increased computational cost, due to the stiffer interface requiring more iterations to solve. Therefore, choosing an optimal K_{coh} is critical for balancing accuracy and computational efficiency [63]. The cohesive strength defines the maximum stress that the interface can withstand before damage initiates. It is a crucial parameter because it directly influences the onset of delamination. Finally, accurate determination of $\sigma_{\max}$ ensures that the model correctly predicts the initiation of cracks. If $\sigma_{\max}$ is set too high or too low, the model might either delay the initiation of delamination or predict it prematurely, leading to discrepancies with experimental observations. Accurate values of G_c ensure that the energy dissipation during crack propagation is correctly represented, which is crucial for predicting the delamination path and the load-displacement response of the composite. The sensitivity of the model to K_{coh} and $\sigma_{\max}$ is examined to ensure the chosen values provide a balance between numerical accuracy and computational efficiency. For most problems, a penalty stiffness ranging from 10^5 to 10^6 N/mm^3 provides the best balance between accuracy and efficiency [63].

Since its inception, cohesive zones have been applied to model various fracture phenomena. E.g., in 1990, Tvergaard [64] modeled fiber pull-out in metal-matrix composites using a polynomial TSL (Figure 2.19a), and in 1999, De-Andrés et al. [20] used an exponential TSL (Figure 2.19d) to model fatigue crack growth in aluminum shafts. In 2011, Paggi and Wriggers [59] described the degradation of properties within the interface area using a CDM framework. They illustrated that the stress-displacement response of the system can be seen as a new CZM, shaped directly by the progression of damage. The TSL serves as a phenomenological representation of the underlying fracture mechanism, however, the shape and input parameters of CZMs are usually chosen computational reasons rather than being physically accurate [59]. Another approach is to calibrate the TSL to match experimental data. In 2023, Abdel-Monsef et al. [65] created a new Multi-Linear Cohesive Law (MLCL) based on the superposition of multiple bilinear TSLs (Figure 2.19e) to represent experimental data, the resulting TSL can be seen in Figure 2.20.

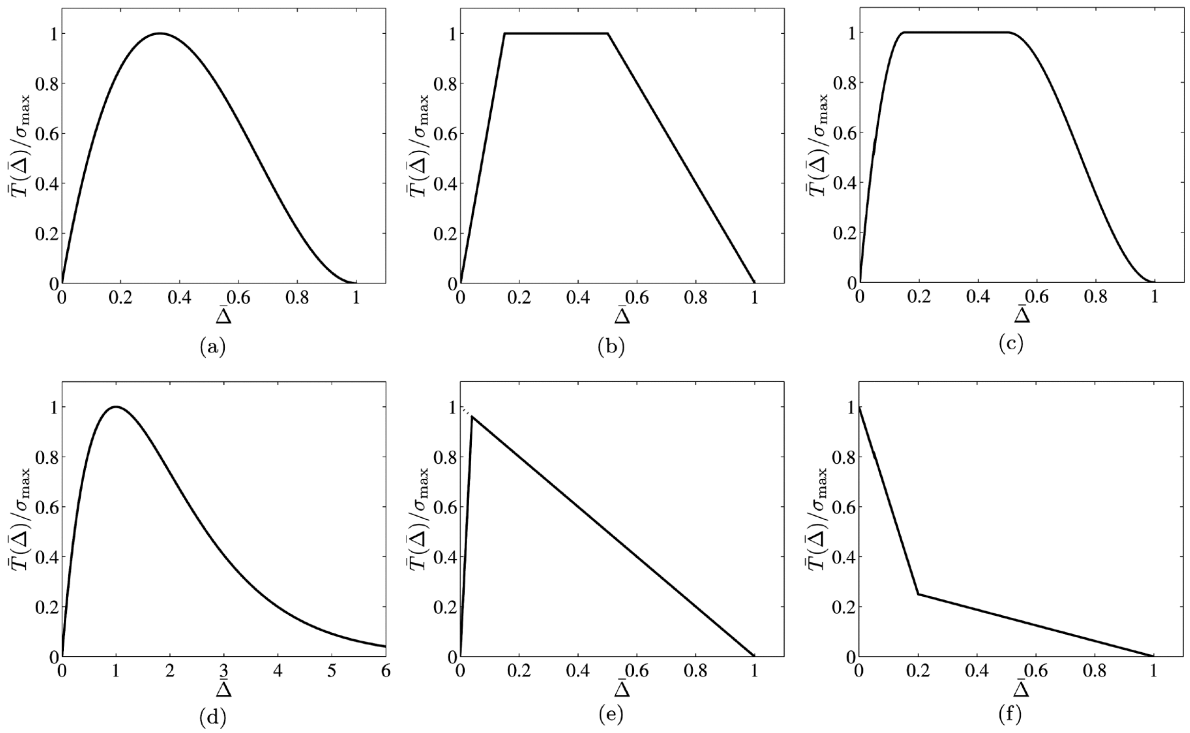

Figure 2.19: Several traction-separation laws: (a) cubic polynomial, (b) trapezoidal, (c) smoothed trapezoidal, (d) exponential, (e) linear softening, and (f) bilinear softening (adapted from [60]).

In the context of CDM, as the mesh is refined, the fracture energy and dissipation tend to decrease, ultimately approaching zero. This phenomenon results in a localization problem, however, CZMs do not face this challenge because they include a well-defined fracture energy and represent fracture as a sharp discontinuity [19]. As a result, CZMs effectively solves the issue of diminishing energy dissipation with mesh refinement. However, the interface element approach has its drawbacks, notably the constraint imposed on the fracture path, confined to element interfaces [14, 30, 34]. According to the principle of minimum potential energy, the required energy for propagation increases since the crack has to deviate from the *"optimal"* direction [19].

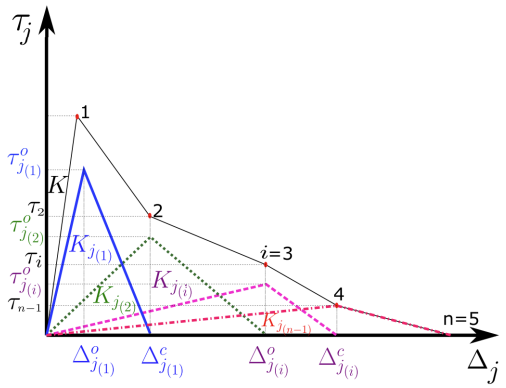

Figure 2.20: A mixed-mode multi-linear traction-separation law created to match experimental data using several bilinear cohesive laws [65].

Finite-Thickness Cohesive Elements

As mentioned earlier, zero-thickness interface elements relate interfacial tractions to the relative displacements across the interface. Since these are surface elements, it is not possible to directly calculate strains, one length scale is thus undefined in the elastic material law [34]. The concept of finite thickness cohesive elements allows for the description of the interface by assuming that failure occurs within a very narrow and confined area [16, 17, 66]. In such elements, the strains and resulting stresses are calculated directly at the integrations points from the displacement field inside the interface element, using the stresses across the interface is thus not needed. Since delamination is caused by the interlaminar stresses only, the in-plane stresses are set to zero a priori in the element formulation. The two in-plane normal stresses and the in-plane shear stress are managed by the deformation of the laminate itself, with each layer bearing the load. The interface between layers does not contribute to this in-plane deformation. If the interface elements were to influence the mechanical response under in-plane loading, it would introduce an incorrect additional stiffness into the structure. As a result, the only stresses that the interface should handle are the through-thickness normal stress and the two out-of-plane shear stresses, together forming the interlaminar stress vector [14].

The failure strain ε_f must correspond to the fracture energy released during total decohesion, G_c. This value can be determined by calculating the area under the stress-strain curve depicted in Figure 2.21b and multiplying it by the element thickness h. This relationship establishes a link between the stress-strain behavior and the ERR, as described by Griffith and Irwin [67, 68]. The fracture toughness is written as follows [57]:

$$G_c = h \int_0^{\varepsilon_f} \sigma(\varepsilon)\, d\varepsilon \tag{2.17}$$

In the reference configuration, the thickness of the cohesive element is assumed to be equal to the crack band thickness, thereby defining the element thickness as the characteristic length. However, regular surface-based cohesive zone models typically integrate a length scale associated with the cohesive element's surface area, as illustrated in Equation 2.16. This difference can be explained be noting that the Young's modulus and shear modulus are related to the area by definition [57].

It has been shown that the global response of the structure remains nearly unchanged for thickness ratios of $h_T/h_L \leq 10^{-2}$ [14, 34], see Figure 2.21a. The reason for this is that the bending and torsional moments, resulting from nodal eccentric forces, tend to zero.

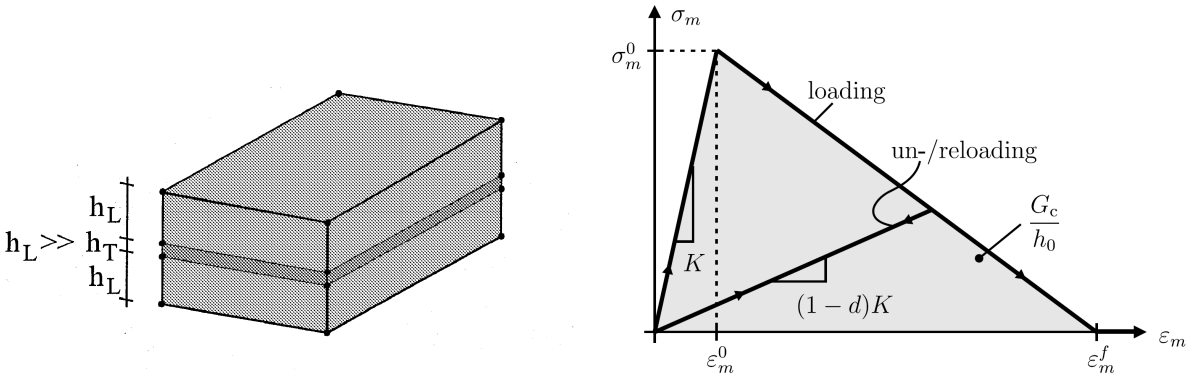

(a) Eight-node finite thickness interface element between two solid elements representing laminae [34].

(b) Finite thickness traction-separation law where the fracture toughness is now divided by the initial height [14].

Figure 2.21: Finite thickness interface element and traction-separation law.

2.3. Conclusions from the Literature Study

The literature review has highlighted the limitations and strengths of various plate theories, particularly in the context of modeling laminated composites. ESL methods, such as CLPT and FSDT, provide a simplified approach that is effective for analyzing the global response of thin to moderately thick laminates. However, these methods lack the accuracy needed to capture local nonlinear behaviors and complex 3D stress states at interfaces, which are crucial in scenarios involving interlaminar damage.

Advanced approaches, such as Layerwise and Zigzag theories, were introduced to address some of the issues arising in ESL theories. However, Layerwise theories are computationally expensive for most realistic laminates due to the large number of unknowns. Zigzag theories, on the other hand, are mainly suited for undamaged laminates, making them less applicable for this work. Global-Local theories combine ESL and Layerwise methods by using Layerwise theories for only some laminae. Despite this improvement, they still face challenges when dealing with highly localized damage or large deformations, where modeling strategies such as 3D brick elements or full Layerwise fields might be necessary despite their higher computational cost.

The CZM has been successfully utilized to model interlaminar damage [14, 23, 26, 34], but its reliance on mesh boundaries can cause issues in modeling intralaminar damage. Additionally, coarse meshes lead to problems such as an oscillatory load displacement response [17]. Attempts to model delaminations and matrix cracks using the CZM have also been made [23], which was achieved by placing cohesive elements between solid elements inside and between individual laminae. However, this approach requires prior knowledge of the crack path to place cohesive elements accordingly. One possible solution is to place cohesive elements everywhere. If intrinsic cohesive elements are used, the solution may be impacted by artificial compliance due to the penalty stiffness. On the other hand, using extrinsic elements requires creating a large number of nodes during the simulation, which complicates parallel implementation and reduces its efficiency.

A summary of the literature utilizing the Discontinuous Galerkin method to model damage in composites is presented in Table Table 2.1. The Discontinuous Galerkin method has not been widely used to model damage in composites, with one exception. Specifically, Versino et al. [4, 5] applied the method to model delaminations in composites. However, their implementation does not account for rotational degrees of freedom or the associated shear deformation. In contrast, the geometrically exact shells presented by Simo and Fox [40, 41] do not rely on such assumptions and are capable of modeling any deformation, provided that the kinematic assumptions hold true. Using such elements to model damage occurring during buckling and large deformation would be more accurate.

Table 2.1: Plate Theories and Implementation of Discontinuous Galerkin, Interlaminar, and Intralaminar Damage.

Plate Theory	Interlaminar Damage	Intralaminar Damage
Kirchhoff-Love	-	-
Reissner-Mindlin	-	-
Layerwise	-	-
Zig-Zag	-	-
Global-Local	[4, 5]	-

Unlike approaches such as XFEM and PNM, VCCT and cohesive elements are confined to mesh boundaries, leading to challenges when dealing with coarse meshes. In particular, CZM often experiences oscillatory load-displacement responses under such conditions. However, when combined with the Discontinuous Galerkin method, cohesive elements present a more straightforward approach. Since all nodes on the boundaries are predefined, there's no need for additional steps to create or define them, eliminating the need for recomputing elemental contributions during the simulation. While this approach may be much slower in serial computation compared to the aforementioned methods, it is feasible in parallel computation, as the entire size of the global system of equations is known beforehand. By employing an extrinsic cohesive law, this method avoids making assumptions about the material response prior to fracture. Consequently, the DG/CZM method can effectively model both

interlaminar and intralaminar damage by placing cohesive elements throughout the model.

Methods like XFEM and PNM offer alternative approaches for modeling delaminations. XFEM enriches the shape functions as cracks propagate through elements, while PNM activates additional phantom nodes as cracks form, allowing for a mesh-independent solution. Thus requiring the recalculation and assembly of elemental contributions to the global system of equations as new elements are formed. The FNM is conceptually similar to remeshing, simplifying the process by directly using the intersection coordinates of the crack with the elemental boundaries to assign floating nodes as the crack propagates.

This leads to the following research question, which serves as the first step towards modeling delaminations at arbitrary interfaces:

Main Research Question

How can high-fidelity Finite Element Methods be employed to investigate the feasibility of explicitly modeling each layer in multi-layered materials subjected to large deformations and buckling at the component level?

This will be done by answering the following sub-questions:

Sub-Question 1

How can the Discontinuous Galerkin method be employed to model any number of layers through-the-thickness?

Sub-Question 2

How do the multi-layer predictions from the proposed method compare to equivalent single-layer configurations across several benchmarks?

Sub-Question 3

What adjustments are needed for the proposed method for it to be able to model interlaminar damage effectively along any interface using the Discontinuous Galerkin approach?

Chapter 3

Methodology

This chapter starts with a detailed kinematic description is provided in Section 3.1, which lays the groundwork for understanding the deformation of the shell elements. Next, the weak form of the governing equations is discussed in Section 3.2. The discretization process is addressed in Section 3.3, where the Discontinuous Galerkin method used for solving the equations is introduced. Following this, Section 3.4 presents the contribution of the new interface elements to the weak form The constitutive laws applicable to both isotropic and composite materials are presented in Section 3.5. Implementation details of the numerical methods are discussed in Section 3.6, covering the key aspects of the computational framework. Section 3.7 explains how incremental variations are solved. Subsequently, the kinematic update procedures are examined in Section 3.8, which are crucial for tracking the deformation accurately throughout the analysis. Finally, the through-the-thickness stretching of the shell is explained in Section 3.9, which, although not implemented in this study, will allow the incorporation of out-of-plane stresses into the model to be used for fracture initiation.

In the following, Greek indices (α, β, γ) vary from 1 to 2 unless mentioned otherwise, and Latin indices (i, j, k) vary from 1 to 3. All equations and definitions are taken from [19] and [41] unless stated otherwise.

3.1. Kinematic Description

The key assumption in shell elements is that the thickness is much smaller compared with the in-plane dimensions as well as both radii of curvature [33]. Because of this, only the mid-surface of the shell element has to be modeled where the thickness only affects the stresses. As a result, any point in the body is defined relative to the mid-surface, denoted by $\mathcal{S}$. The mid-surface has a parameterization $\boldsymbol{\varphi} : \mathcal{A} \subset \mathbb{R}^2 \rightarrow \mathbb{R}^3$ such that:

$$\mathcal{S} = \{\bar{\mathbf{x}} \in \mathbb{R}^3 : \bar{\mathbf{x}} = \boldsymbol{\varphi}(\boldsymbol{\xi}),\ \boldsymbol{\xi} \in \mathcal{A}\} \tag{3.1}$$

Where $\mathcal{A}$ is the mid-surface in parametric coordinates. The following set is defined to state the kinematic assumptions:

$$\mathscr{C} := \left\{(\boldsymbol{\varphi}, \mathbf{t}) : \mathcal{A} \subset \mathbb{R}^2 \rightarrow \mathbb{R}^3 \times S^2\right\} \tag{3.2}$$

This set defines the ***inextensible*** *one-director Cosserat surface* where:

- The map $\boldsymbol{\varphi} : \mathcal{A} \rightarrow \mathbb{R}^3$ is used to define the mid-surface position.
- The map $\mathbf{t} : \mathcal{A} \rightarrow S^2$ is used to define a normal vector at any point in the mid-surface.

Cosserat Surface

A Cosserat surface is a body $\mathscr{C}$ consisting of a mid-surface in $\mathbb{R}^3$, with particles $\bar{\mathbf{x}}$ and a single director $\mathbf{t}$ attached to every point of the mid-surface [41].

Any configuration of the shell is described as:

$$\mathcal{B} := \left\{\mathbf{x} \in \mathbb{R}^3 \mid \mathbf{x} = \boldsymbol{\Phi}(\xi_1, \xi_2, \xi_3) \ \text{ where } \ (\xi_1, \xi_2, \xi_3) \in \mathscr{C}\right\} \tag{3.3}$$

An exact description for the reference configuration also exists:

$$\mathcal{B}^0 \coloneqq \left\{ \mathbf{X} \in \mathbb{R}^3 \mid \mathbf{X} = \mathbf{\Phi}^0 (\xi_1, \xi_2, \xi_3) \text{ where } (\xi_1, \xi_2, \xi_3) \in \mathscr{C} \right\} \tag{3.4}$$

Material points within the body are located using a vector field $\mathbf{t} : \mathcal{A} \to S^2$, referred to as the director field, where S^2 represents the unit sphere defined as:

$$S^2 = \{ \mathbf{t} \in \mathbb{R}^3 : \|\mathbf{t}\| = 1 \} \tag{3.5}$$

This means that the director can take any value on the unit sphere. The kinematic assumptions allows for points $\mathbf{x}$ in $\mathcal{B}$ to be described by the mapping:

$$\mathbf{x} = \mathbf{\Phi} (\xi_1, \xi_2, \xi_3) \coloneqq \boldsymbol{\varphi} (\xi_1, \xi_2) + \xi_3 \mathbf{t} (\xi_1, \xi_2) \tag{3.6}$$

Where $\boldsymbol{\varphi} (\xi_1, \xi_2)$ represents the parameterization of the mid-surface and $\mathbf{t} (\xi_1, \xi_2)$ denotes the director field, see Figure 3.1. The reference configuration is defined as the undeformed shell, where points $\mathbf{X}$ in $\mathcal{B}^0$ are described by:

$$\mathbf{X} = \mathbf{\Phi}^0 (\xi_1, \xi_2, \xi_3) \coloneqq \boldsymbol{\varphi}^0 (\xi_1, \xi_2) + \xi_3 \mathbf{t}^0 (\xi_1, \xi_2) \tag{3.7}$$

In this equation and subsequent ones, reference configuration quantities are labeled with superscript 0. The deformation is represented by the map $\boldsymbol{\chi} : \mathcal{B}^0 \to \mathcal{B}$ defined as:

$$\boldsymbol{\chi} \coloneqq \mathbf{\Phi} \circ \left(\mathbf{\Phi}^0 \right)^{-1} \tag{3.8}$$

The tangent map $\nabla \mathbf{\Phi}$ relative to the inertial basis $\{E_i\}_{i=1,2,3}$ is given by:

$$\nabla \mathbf{\Phi} \coloneqq \frac{\partial \mathbf{\Phi}}{\partial \xi_i} \otimes E^i = g_i \otimes E^i \tag{3.9}$$

The tangent map is $\nabla \mathbf{\Phi}$ associated with $\mathbf{\Phi} : \mathcal{A} \times [h^-, h^+] \to \mathbb{R}^3$ is given by:

$$\nabla \mathbf{\Phi} = (\partial_\alpha \boldsymbol{\varphi} + \xi_3 \partial_\alpha \mathbf{t}) \otimes E^\alpha + \mathbf{t} \otimes E^3 \tag{3.10}$$

Where $\partial_\alpha \coloneqq \frac{\partial}{\partial \xi_\alpha}$ denotes the partial derivative with respect to the parametric coordinates, such that $a_\alpha = \partial_\alpha \boldsymbol{\varphi}$. The deformation gradient associated with the displacement is then:

$$\boldsymbol{F} = \boldsymbol{T}_{\boldsymbol{\chi}} \coloneqq \nabla \mathbf{\Phi} \circ (\nabla \mathbf{\Phi}^0)^{-1} \tag{3.11}$$

Finally, the variation of $\boldsymbol{F}$ is:

$$\delta \boldsymbol{F} = \left[(\partial_\alpha \delta \boldsymbol{\varphi} + \xi_3 \partial_\alpha \delta \mathbf{t}) \otimes E^\alpha + \delta \mathbf{t} \otimes E^3 \right] (\nabla \mathbf{\Phi}^0)^{-1} \tag{3.12}$$

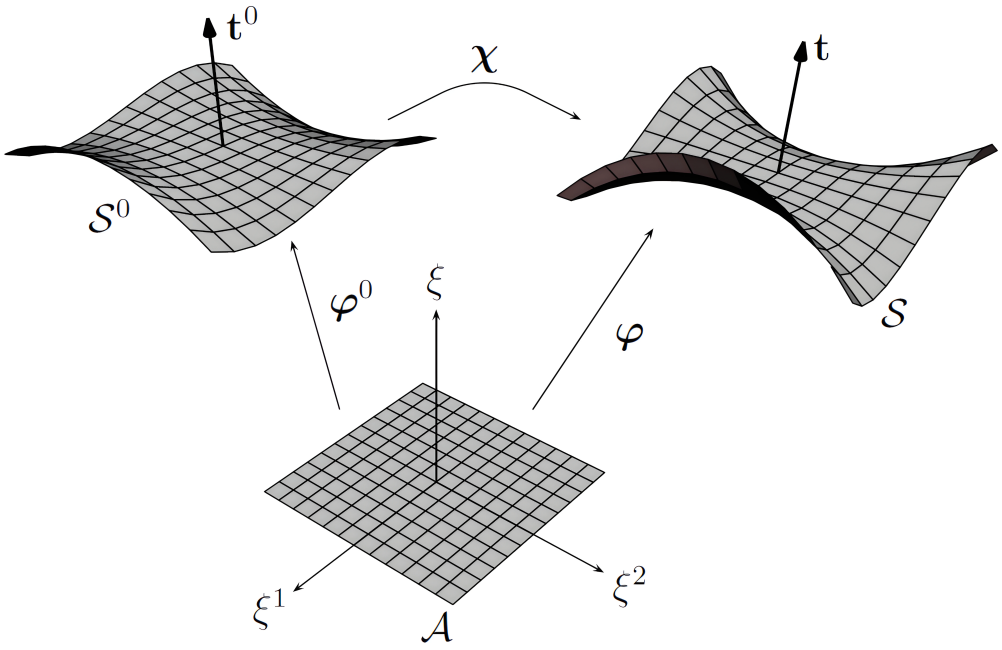

Figure 3.1: Reference and current configurations of the mid-surface [19, 69, 70].

The tangent space to the mid-surface at the point $\bar{\mathbf{x}}$, denoted by $T_{\bar{\mathbf{x}}}\mathcal{S}$, is spanned by the convected basis $\{a_\alpha\}_{\alpha=1,2}$ given by:

$$a_\alpha := \frac{\partial \boldsymbol{\varphi}}{\partial \xi_\alpha} \tag{3.13}$$

This tangent space $T_{\bar{\mathbf{x}}}\mathcal{S}$ can be thought of as the basis vectors in the plane tangent to the shell at the point $\bar{\mathbf{x}}$, this tangent basis is trivial for flat plates since in this case it is always $\mathbb{R}^2$. The tangent space $\mathbf{t} \in S^2$ (tangent plane to $\mathbf{t}$ on the unit sphere S^2) can be thought of as the set containing vectors tangent to curves $\varepsilon \mapsto \mathbf{t}_\varepsilon$. It is obtained by noting that $\mathbf{t}_\varepsilon|_{\varepsilon=0} = \mathbf{t}$ and taking the derivative of Equation 3.5 with respect to ε:

$$T_{\mathbf{t}}S^2 = \left\{\delta\mathbf{t} \in \mathbb{R}^3 : \delta\mathbf{t} \cdot \mathbf{t} = 0\right\} \tag{3.14}$$

This means that $\delta\mathbf{t}$ is a vector in $\mathbb{R}^3$ defined to be orthogonal to the vector $\mathbf{t}$. The director in the reference configuration is obtained as:

$$\mathbf{t}^0 = \frac{a_1^0 \times a_2^0}{\|a_1^0 \times a_2^0\|} \tag{3.15}$$

The components of the metric tensor of the mid-surface are:

$$a_{\alpha\beta} = \partial_\alpha \boldsymbol{\varphi} \cdot \partial_\beta \boldsymbol{\varphi} \tag{3.16}$$

The metric tensor essentially represents the projections of the basis vectors onto each other. In the case of a plate, the metric tensor reduces to the identity tensor. The so-called dual basis vectors can be determined from the covariant basis vectors a_α as:

$$a^\alpha = a^{\alpha\beta} a_\beta \tag{3.17}$$

Here, $a^{\alpha\beta}$ is the inverse of the metric tensor $a_{\alpha\beta}$, and they are related by the Kronecker delta δ^α_γ:

$$a^{\alpha\beta} a_{\beta\gamma} = \delta^\alpha_\gamma \tag{3.18}$$

The shearing of normal vectors is calculated using the first order tensor γ_α as follows:

$$\gamma_\alpha = a_\alpha \cdot \mathbf{t} \tag{3.19}$$

This tensor would be zero in the Kirchhoff-Love formulation. The curvature tensor $\kappa_{\alpha\beta}$ is determined by:

$$\kappa_{\alpha\beta} \coloneqq a_\alpha \cdot \partial_\beta \mathbf{t} \tag{3.20}$$

The curvature tensor determines the bending of the mid-surface and equals the classical curvature tensor when the out-of-plane shear strains are zero, the director $\mathbf{t}$ is normal to the surface in this case. In the reference configuration, these tensors are written as $a^0_{\alpha\beta}$, γ^0_α, and $\kappa^0_{\alpha\beta}$. The strains are then determined relative to the reference configuration as:

$$\epsilon_{\alpha\beta} = \frac{1}{2}\left(a_{\alpha\beta} - a^0_{\alpha\beta}\right) \tag{3.21a}$$

$$\zeta_\alpha = \gamma_\alpha - \gamma^0_\alpha \tag{3.21b}$$

$$\rho_{\alpha\beta} = \kappa_{\alpha\beta} - \kappa^0_{\alpha\beta} \tag{3.21c}$$

The Jacobian of the metric tensor is given as:

$$\bar{j} = \|a_1 \times a_2\| = \sqrt{\det\left(a_{\alpha\beta}\right)} = \sqrt{a_{11}a_{22} - a_{12}a_{21}} \tag{3.22}$$

The differential area element in $\mathcal{S}$ is then obtained using the surface Jacobian as follows:

$$\mathrm{d}\mathcal{S} = \bar{j}\mathrm{d}\mathcal{A}, \quad \mathrm{d}\mathcal{A} \coloneqq \mathrm{d}\xi_1\mathrm{d}\xi_2 \tag{3.23}$$

Based on the mapping in Equation 3.7, 3D covariant base vectors for the $\boldsymbol{\xi}$-reference frame are given by:

$$g_i = \frac{\partial \boldsymbol{\Phi}^0}{\partial \xi_i} \tag{3.24}$$

Substituting Equation 3.7 into Equation 3.24, the covariant base vectors g_i are given as:

$$g_\alpha = a_\alpha + \xi_3 \frac{\partial \mathbf{t}^0}{\partial \xi_\alpha} \tag{3.25a}$$

$$g_3 = \mathbf{t}^0 \tag{3.25b}$$

The metric tensor of the entire body is calculated using the covariant base vectors g_i as follows:

$$g_{ij} = g_i \cdot g_j \tag{3.26}$$

Quantities calculated in the reference frame spanned by the covariant basis g_α are mapped to the reference surface through the shifter tensor μ^β_α, which is expressed as:

$$g_\alpha = \mu^\beta_\alpha a_\beta \tag{3.27}$$

Finally, the volume of an element can be written as:

$$dV = \sqrt{\det\left(g_{ij}\right)}\, d\xi_1 d\xi_2 d\xi_3 = \mu d\mathcal{S} d\xi_3 \tag{3.28}$$

Where μ is the determinant of the shifter tensor. Since different interfaces can have different areas due to the curvature, μ has to be evaluated at the thickness coordinate of the interface as follows:

$$\mu = \det\left(\mu^\beta_\alpha\right), \quad \mu^{(k)} = \mu\big|_{\xi_3^{(k)}} \tag{3.29}$$

Consequently, an area element on the kth interface can be expressed as:

$$d\mathcal{S}^{(k)} = \mu^{(k)} d\mathcal{S} \tag{3.30}$$

An example of a mapping for a flat plate can be seen in Appendix B.

3.2. Weak Form of the Equations of Motion

The derivation of the general weak form can be seen in Appendix A, however, it needs to be slightly adjusted for shell elements. Starting with the essential Dirichlet boundary conditions the shell is subjected to:

$$\boldsymbol{\varphi}(\xi_\alpha, t) = \bar{\boldsymbol{\varphi}}(\xi_\alpha, t) \quad \text{on} \quad \partial_\varphi \mathcal{A} \times [0, T] \tag{3.31a}$$

$$\mathbf{t}(\xi_\alpha, t) = \bar{\mathbf{t}}(\xi_\alpha, t) \quad \text{on} \quad \partial_\mathbf{t} \mathcal{A} \times [0, T] \tag{3.31b}$$

The space of admissible velocities is all that comply with these prescribed values:

$$\mathbb{X} = \left\{ \mathcal{V} \in \mathcal{A} \to \mathbb{R}^3 \times T_\mathbf{t} S^2 : \boldsymbol{\varphi}|_{\partial_\varphi \mathcal{A}} = \bar{\boldsymbol{\varphi}} \text{ and } \mathbf{t}|_{\partial_\mathbf{t} \mathcal{A}} = \bar{\mathbf{t}} \right\} \tag{3.32}$$

The space of admissible variations (those that satisfy the geometric constraints) can be defined as:

$$\mathbb{V} = \left\{ \delta\mathcal{V} := (\delta\boldsymbol{\varphi}, \delta\mathbf{t}) \in \mathcal{A} \to \mathbb{R}^3 \times T_\mathbf{t} S^2 : \delta\boldsymbol{\varphi}|_{\partial_\varphi \mathcal{A}} = 0 \text{ and } \delta\mathbf{t}|_{\partial_\mathbf{t} \mathcal{A}} = 0 \right\} \tag{3.33}$$

This space, as expected, includes all possible variations that comply with the Dirichlet boundary conditions on the boundary.

Principle of Virtual Power

The *Principle of Virtual Power* states [19]:

- The internal power of the body remains unchanged regardless of its orientation.
- The energy balance is $\mathcal{P}_{\text{ext}} = \mathcal{P}_{\text{int}} + \delta\mathcal{K}$ for all admissible variations $\delta\mathcal{V} \in \mathbb{V}$.

The equations of motion are derived from the *Principle of Virtual Power*, as explained by Gurtin [71, 72]. By selecting a set of variations $(\delta\boldsymbol{\varphi}, \delta\mathbf{t}) \in \delta\boldsymbol{\mathcal{V}}$, the weak form of the equations of motion is established. Introducing:

- The stress resultant $\mathbf{n}^\alpha$ that expends power through $\partial_\alpha \delta\boldsymbol{\varphi}$.
- The stress couple resultant $\tilde{\mathbf{m}}^\alpha$ that expends power through $\partial_\alpha \delta\mathbf{t}$.
- The through-thickness stress resultant $\mathbf{l}$ that expends power through $\delta\mathbf{t}$.

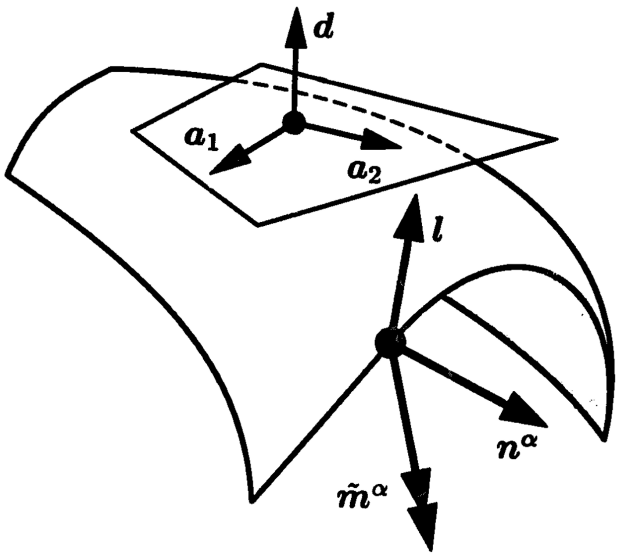

Figure 3.2: Convected (mid-surface) basis where $\mathbf{d}$ is the modified director which will be covered in Section 3.9, stress resultant $\mathbf{n}^\alpha$, stress couples resultant $\tilde{\mathbf{m}}^\alpha$, and through-the-thickness stress resultant $\mathbf{l}$ [73].

Following the terminology of Simo and Fox [40], $\mathbf{n}^\alpha$ is the stress resultant, $\tilde{\mathbf{m}}^\alpha$ is the stress couple resultant, and $\mathbf{l}$ is the through-thickness stress resultant. Using these resultants, as shown in Figure 3.2, the virtual internal power is given by:

$$\mathcal{P}_{\text{int}}(\delta\mathcal{V}) \coloneqq \int_\Omega \boldsymbol{P} : \delta\boldsymbol{F}\, d\Omega = \int_h \int_\mathcal{S} \left(\boldsymbol{P}(\nabla\boldsymbol{\Phi}^0)^{-1} E^\alpha \cdot (\partial_\alpha \delta\boldsymbol{\varphi} + \xi_3 \partial_\alpha \delta\mathbf{t}) + \boldsymbol{P}(\nabla\boldsymbol{\Phi}^0)^{-1} E^3 \cdot \delta\mathbf{t} \right) j^0 d\xi_1 d\xi_2 d\xi_3 \tag{3.34}$$

Where Equation 3.28 has been used and $\boldsymbol{P}$ and $\boldsymbol{F}$ are the First Piola-Kirchhoff stress tensor and the deformation gradient, respectively [40]. This expression simplifies by using Equation 3.23 and the definitions for the stress resultants:

$$\mathcal{P}_{\text{int}}(\delta\mathcal{V}) \coloneqq \int_\mathcal{S} (\mathbf{n}^\alpha \cdot \partial_\alpha \delta\boldsymbol{\varphi} + \tilde{\mathbf{m}}^\alpha \cdot \partial_\alpha \delta\mathbf{t} + \mathbf{l} \cdot \delta\mathbf{t})\, d\mathcal{S} \tag{3.35}$$

With the following definitions for the stress resultants $\mathbf{n}^\alpha$, $\tilde{\mathbf{m}}^\alpha$ and $\mathbf{l}$:

$$\mathbf{n}^\alpha = \frac{1}{\bar{j}} \int_h \boldsymbol{P} g^{0\alpha} j^0\, d\xi_3 \tag{3.36a}$$

$$\tilde{\mathbf{m}}^\alpha = \frac{1}{\bar{j}} \int_h \xi_3 \boldsymbol{P} g^{0\alpha} j^0\, d\xi_3 \tag{3.36b}$$

$$\mathbf{l} = \frac{1}{\bar{j}} \int_h \boldsymbol{P} g^{03} j^0\, d\xi_3 \tag{3.36c}$$

Since $\delta\mathbf{t} \in T_\mathbf{t}\mathcal{S}^2$, it can be shown that due to the assumption of inextensible directors, the component of $\mathbf{l}$ in the direction of $\mathbf{t}$ is indeterminate, it does no work and can thus be neglected [19]. The reduced internal power is then given:

$$\mathcal{P}_{\text{int}}(\delta\mathcal{V}) \coloneqq \int_\mathcal{S} \left(\frac{1}{2} \widetilde{n}_{\alpha\beta} \delta a_{\alpha\beta} + \widetilde{m}_{\alpha\beta} \delta\kappa_{\alpha\beta} + \widetilde{q}_\alpha \delta\gamma_\alpha \right) d\mathcal{S} \tag{3.37}$$

Where $\widetilde{\bullet}$ denotes only the generalized forces that expand power, and the following decomposed stress resultants have been used:

$$\mathbf{n}^\alpha = \widetilde{n}_{\alpha\beta} \partial_\beta \boldsymbol{\varphi} + \widetilde{m}_{\alpha\beta} \partial_\beta \mathbf{t} + \widetilde{q}_\alpha \mathbf{t} \tag{3.38a}$$

$$\tilde{\mathbf{m}}^\alpha = \widetilde{m}_{\alpha\beta} \partial_\alpha \boldsymbol{\varphi} + \text{indeterminate components} \tag{3.38b}$$

$$\mathbf{l} = \widetilde{q}_\alpha \partial_\alpha \boldsymbol{\varphi} + \text{indeterminate components} \tag{3.38c}$$

However, the assumption of inextensible directors does not allow for the modeling of delaminations in composite laminates where the stress normal to the mid-surface is important, more about this in Section 3.9. As usual the external power consists of body and boundary terms:

$$\mathcal{P}_{\text{ext}}(\delta\mathcal{V}) = \int_\mathcal{S} (\mathbf{f} \cdot \delta\boldsymbol{\varphi} + \boldsymbol{\tau} \cdot \delta\mathbf{t})\, d\mathcal{S} + \int_{\partial_N\mathcal{S}} \bar{\bar{\mathbf{n}}} \cdot \delta\boldsymbol{\varphi}\, ds + \int_{\partial_M\mathcal{S}} \bar{\bar{\mathbf{m}}} \cdot \delta\mathbf{t}\, ds \tag{3.39}$$

Where ds stands for an arc length in $\mathcal{S}$. The vectors $\bar{\bar{\mathbf{n}}}$ and $\bar{\bar{\mathbf{m}}}$ represent the prescribed force and torque on the boundaries $\partial_N\mathcal{S}$ and $\partial_M\mathcal{S}$, respectively. The regions where essential and natural boundary conditions are applied satisfy the following conditions:

- $\overline{\partial_{\boldsymbol{\varphi}}\mathcal{A} \cup \partial_N\mathcal{A}} = \partial\mathcal{A}$
- $\partial_{\boldsymbol{\varphi}}\mathcal{A} \cap \partial_N\mathcal{A} = \emptyset$
- $\overline{\partial_\mathbf{t}\mathcal{A} \cup \partial_M\mathcal{A}} = \partial\mathcal{A}$
- $\partial_\mathbf{t}\mathcal{A} \cap \partial_M\mathcal{A} = \emptyset$

The kinetic energy is taken to be composed of the quadratic forms:

$$\mathcal{K}(\mathcal{V}) = \int_\mathcal{S} \left(\frac{1}{2} \bar{\rho} \|\dot{\boldsymbol{\varphi}}\|^2 + \frac{1}{2} \bar{I} \|\dot{\mathbf{t}}\|^2 \right) d\mathcal{S} \tag{3.40}$$

A definition for $\bar{\rho}$ and $\bar{I}$ will be given in Section 3.6. The variation in kinetic energy can then be written as:

$$\delta\mathcal{K}(\delta\mathcal{V}) = \int_{\mathcal{S}} \left(\bar{\rho}\ddot{\boldsymbol{\varphi}} \cdot \delta\boldsymbol{\varphi} + \bar{I}\ddot{\mathbf{t}} \cdot \delta\mathbf{t}\right) \, d\mathcal{S} \tag{3.41}$$

3.3. Discontinuous Galerkin Discretization

One of the main advantages of the Discontinuous Galerkin method, as mentioned before, is that each element has its own domain. This allows for the initiation of cracks without the need to create new nodes, assign them, or adjust the shape functions. Damage can be effectively modeled by deactivating the stability integrals across internal boundaries in the weak form, which are then replaced with traction-separation integrals to enable damage propagation. Additionally, jumps in displacement occur naturally at each interface, which can directly be utilized in the traction-separation integrals.

To ensure that a shape function is suitable for finite element analysis, the integral of the function over the domain must be finite. This guarantees that integrals involving these shape function remain well-defined. Additionally, for the function's derivatives to be usable in the weak or variational formulation, their integrals must also be finite [74]. The FEM involves integrals of both the shape functions and their derivatives to approximate the solution. If these integrals are not finite, the contributions to the weak form will not be either.

Let $\mathcal{T}_h$ be the set of isoparametric triangular elements that interpolate the mid-surface of the shell, denoted as $\mathcal{S}$. Here, $\mathcal{S} \simeq \mathcal{S}^h = \bigcup_{E\in\mathcal{T}_h} E$. The notation $\partial_I E$ signifies the collection of all internal edges and surfaces, $\left[\bigcup_{E\in\mathcal{T}_h} \partial E\right] \setminus \partial\mathcal{S}$.

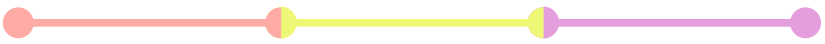

(a) Three beam elements with connected nodes.

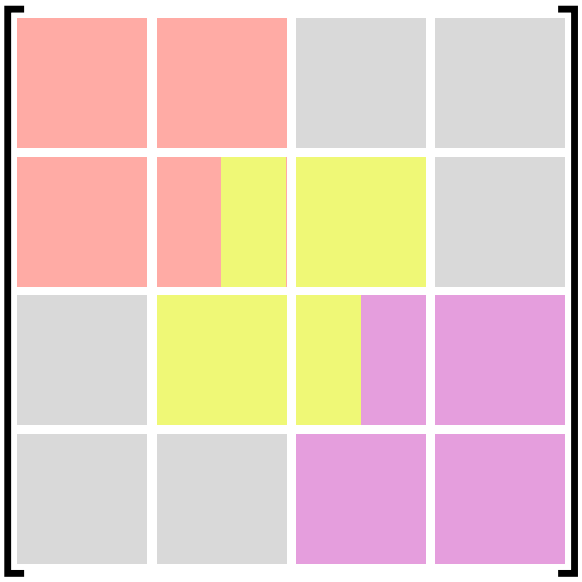

(b) Continuous Galerkin stiffness matrix representation of the structure above.

Figure 3.3: Continuous Galerkin.

Figure 3.3b illustrates how the structure shown in Figure 3.3a is assembled into a global stiffness

matrix, where each block represents a 3×3 submatrix. It is evident that nodes are shared between elements, as connected elements contribute to the same entries in the matrix. These entries reflect the physical connections in the actual structure. For n elements, the stiffness matrix has dimensions $3(n+1) \times 3(n+1)$.

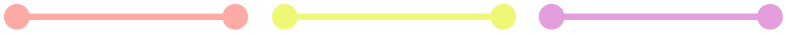

(a) Three beam elements with disconnected nodes.

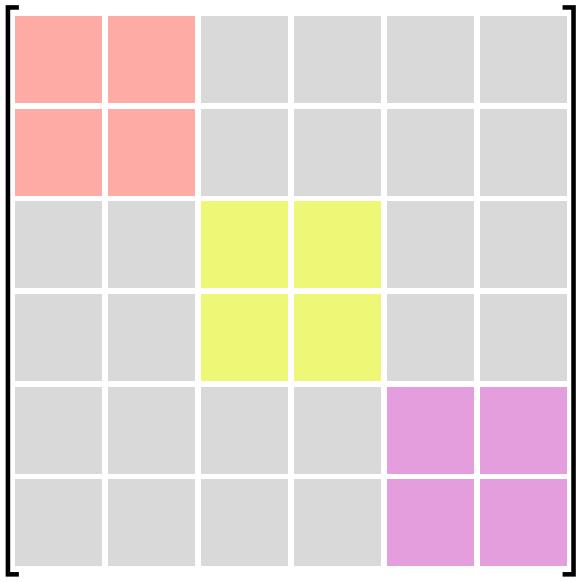

(b) Discontinuous Galerkin stiffness matrix representation of the structure above.

Figure 3.4: Discontinuous Galerkin.

As before, Figure 3.4b illustrates how the structure shown in Figure 3.4a is assembled into a global stiffness matrix, with each block still representing a 3×3 submatrix. It is immediately apparent that the size of the global stiffness matrix has increased, with many zero entries. In comparison with the stiffness matrix in Figure 3.3b, it is clear that elements no longer share nodes, as there are no entries with contributions from more than one element. The stiffness matrix now has dimensions $6n \times 6n$.

As noted in [11, 19], an issue with shear-flexible shells is the phenomenon known as locking. Locking occurs when the discretized shell structure becomes excessively stiff as its thickness decreases, especially when dealing with shear-flexible elements. This happens because the elements cannot accurately capture the bending deformation when the transverse shear strains should vanish, as expected in Kirchhoff-Love shells [33].

In an ideal thin shell model, the energy associated with transverse shear should approach zero. However, in many finite element formulations, this does not occur due to how the displacement and rotation fields are handled. Each node in the mesh typically has five unknowns—three displacements and two rotations—that use the same shape functions. For thin shells, the director should remain perpendicular to the mid-surface, expressed as $\theta = \nabla u$. This means that the space of the displacement field, denoted $\boldsymbol{U}_h$, and the rotation space, denoted $\boldsymbol{\Theta}_h$, must be compatible. The problem arises when the gradient of the displacement field, $\nabla \boldsymbol{U}_h$, is not contained within the rotation space $\boldsymbol{\Theta}_h$, a situation expressed mathematically as $\nabla \boldsymbol{U}_h \not\subseteq \boldsymbol{\Theta}_h$. This lack of compatibility prevents the finite element approximation from accurately representing the displacement field, resulting in displacements that are too small [33]. The transverse shear strain, defined as the difference between the displacement gradient and the rotation (see Equation 3.42), cannot reduce to zero as the shell's thickness decreases. This overestimation of shear stiffness leads to locking, where the shell artificially resists deformation.

$$\gamma = \nabla u - \theta \tag{3.42}$$

The Discontinuous Galerkin method utilizes more flexible function spaces that allow the displacement and rotation fields to be represented by independent function spaces. To prevent shear locking, θ must equal ∇u, so the order of the shape functions $\mathcal{P}$ in the rotation space $\boldsymbol{\Theta}_h$ must be exactly one order lower than those in the displacement space $\boldsymbol{U}_h$, due to the fact that the rotations are derived from the gradients of the displacements. This necessitates the use of different nodes and thus different elements for the rotation field compared to the displacement field. With this, the compatibility equation, expressed mathematically as $\nabla \boldsymbol{U}_h \subseteq \boldsymbol{\Theta}_h$, is satisfied.

3.3.1. Mid-Surface Position Interpolation

Each element $E \in \mathcal{T}_h$ corresponds to a transformation of a master element $\hat{E} \subseteq \mathbb{R}^2$ through the position mapping $E = \boldsymbol{\varphi}(\hat{E}) \in \boldsymbol{X}_h$, see Figure 3.5. The Discontinuous Galerkin function space for positions, denoted as $\boldsymbol{X}_h$, is formed by discrete elemental function spaces $\boldsymbol{X}_h^E$, defined as:

$$\boldsymbol{X}_h = \prod_{E \in \mathcal{T}_h} \boldsymbol{X}_h^E \tag{3.43}$$

Where the element-wise spaces $\boldsymbol{X}_h^E$ are defined as $\boldsymbol{X}_h^E = \mathcal{P}_k(\hat{E})$, with $k \geq 2$ representing the degree of polynomial. It is worth pointing out that with this definition, the position vector will likely exhibit discontinuities on the internal boundaries $\partial_I E$. As usual, functions in $\boldsymbol{X}_h$ must satisfy the essential boundary conditions on $\partial_{\boldsymbol{\varphi}} \mathcal{A}$. This shows the flexibility of the Discontinuous Galerkin method, since each element can have its own function space $\boldsymbol{X}_h^E$.

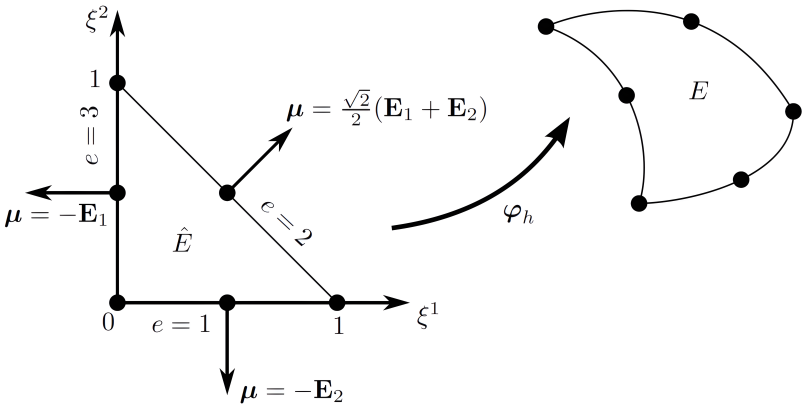

Figure 3.5: The master element denoted by the area $\hat{E}$ and the mapped area E using the mapping $\boldsymbol{\varphi}_h$ [19, 69, 70].

A conventional Lagrange polynomial basis is utilized, with N_A representing the basis functions of $\boldsymbol{X}_h^E$. The mid-surface position is interpolated as:

$$\boldsymbol{\varphi}_h(\xi_1, \xi_2) = \sum_{A=1}^{N_x} N_A(\xi_1, \xi_2)\bar{\mathbf{x}}_A = \sum_{A=1}^{n_x} N_A(\xi_1, \xi_2)\bar{\mathbf{x}}_A \tag{3.44}$$

$$\ddot{\boldsymbol{\varphi}}_h(\xi_1, \xi_2) = \sum_{A=1}^{N_x} N_A(\xi_1, \xi_2)\bar{\mathbf{x}}_A = \sum_{A=1}^{n_x} N_A(\xi_1, \xi_2)\ddot{\bar{\mathbf{x}}}_A \tag{3.45}$$

Here, $n_x = \frac{(k+1)(k+2)}{2}$ denotes the total number of position nodes for each element, and $\bar{\mathbf{x}}_A$ represents the nodal positions of the mid-surface. Since the mid-surface interpolation must be one order higher than the rotations, the lowest order that satisfies this condition is $k = 2$. The symbol N_x is introduced to denote the total number of position nodes in $\mathcal{T}_h$. Since Discontinuous Galerkin basis functions only exist

on a single element, the summation can be written on a per element basis. Variations of the mid-surface position are given by:

$$\delta\boldsymbol{\varphi}\left(\xi_1,\xi_2\right)=\sum_{A=1}^{N_x}N_A(\xi_1,\xi_2)\delta\bar{\mathbf{x}}_A=\sum_{A=1}^{n_x}N_A(\xi_1,\xi_2)\delta\bar{\mathbf{x}}_A \tag{3.46}$$

Where the shape functions N_A are given by:

$$N_1=(1-\xi_1-\xi_2)\,(1-2\xi_1-2\xi_2) \tag{3.47a}$$
$$N_2=\xi_1\,(2\xi_1-1) \tag{3.47b}$$
$$N_3=\xi_2\,(2\xi_2-1) \tag{3.47c}$$
$$N_4=4\xi_1\,(1-\xi_1-\xi_2) \tag{3.47d}$$
$$N_5=4\xi_1\xi_2 \tag{3.47e}$$
$$N_6=4\xi_2\,(1-\xi_1-\xi_2) \tag{3.47f}$$

Figure 3.6 shows what these functions look like.

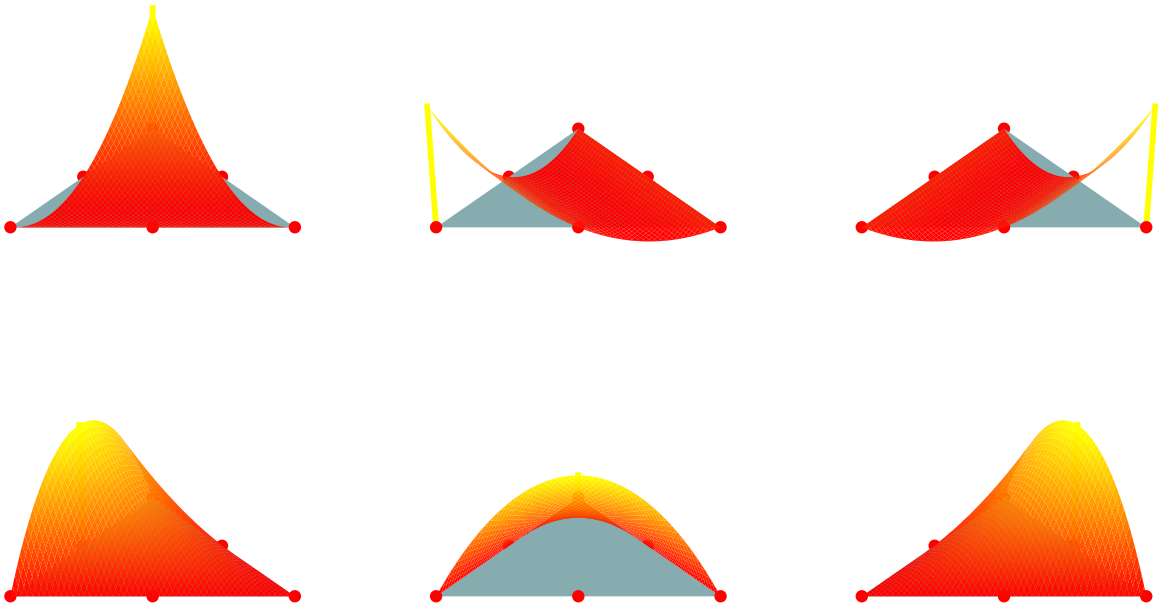

Figure 3.6: Shape functions N_A quadratic triangular element.

3.3.2. Director Interpolation

The director space is represented by $\boldsymbol{T}_h$. Similar to the mid-surface position, the Discontinuous Galerkin space is formed from discrete elemental spaces $\boldsymbol{T}_h^E$:

$$\boldsymbol{T}_h=\prod_{E\in\mathcal{T}_h}\boldsymbol{T}_h^E,\quad \boldsymbol{T}_h^E=\mathcal{P}_{k-1}(\hat{E}) \tag{3.48}$$

As for the mid-surface interpolation, Lagrange polynomials are used for representing the discrete director field $\mathbf{t}_h$. The interpolation is written using the basis functions L_A of $\boldsymbol{T}_h^E$:

$$\mathbf{t}_h(\xi_1,\xi_2)=\sum_{A=1}^{N_T}L_A(\xi_1,\xi_2)\mathbf{t}_A=\sum_{A=1}^{n_T}L_A(\xi_1,\xi_2)\mathbf{t}_A \tag{3.49}$$

Where $\mathbf{t}_A\in S^2$ are nodal director values, and $n_T=\frac{k(k+1)}{2}$ denotes the total number of nodes of each element used to interpolate the director. Here, N_T refers to the complete set of director nodes in the mesh. A kinematic update procedure is used to strictly enforce the unit length constraint on the nodal

directors ($\|\mathbf{t}_h\| = 1$), more about this in Section 3.8. The director in the reference configuration is given by:

$$\mathbf{t} = \mathbf{\Lambda}\mathbf{E}_3 \tag{3.50}$$

The rotation tensor with the rotation axis orthogonal to $\mathbf{E}_3$ has an explicit representation in the undeformed configuration using Rodrigues' formula, as shown in Appendix C.2:

$$\mathbf{\Lambda} = (\mathbf{t}\cdot\mathbf{E}_3)\boldsymbol{I} + (\widehat{\mathbf{E}_3\times\mathbf{t}}) + \frac{1}{1+\mathbf{t}\cdot\mathbf{E}_3}(\mathbf{E}_3\times\mathbf{t})\otimes(\mathbf{E}_3\times\mathbf{t}) \tag{3.51}$$

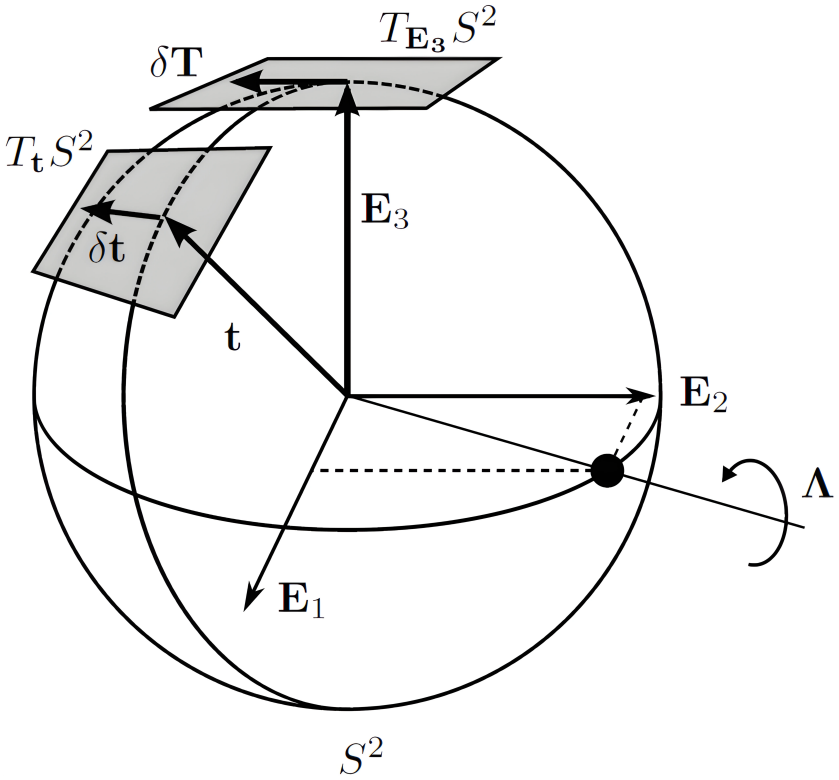

Figure 3.7: Illustration of the unit sphere and its tangent space, the director $\mathbf{t}$ is obtained by rotating $\mathbf{E}_3$ using the exact rotation $\mathbf{\Lambda}$ [19, 69, 70].

As mentioned in Appendix C.3, the subset of rotations with rotation axis $\delta\boldsymbol{\theta}$ perpendicular to the director $\mathbf{t}$ in the deformed or spatial configuration, have director variations $\delta\mathbf{t}$ equal to $\delta\boldsymbol{\theta}\times\mathbf{t}$. This follows from the unit length constraint on the director which results in variations being perpendicular to both the rotation axis and the director. The rotation axis $\delta\boldsymbol{\theta} = \mathbf{\Lambda}\delta\mathbf{\Theta}$, where $\delta\mathbf{\Theta}$ is the rotation axis in the material or rotated description. Using this relation between the rotation axes, the director variation can be rewritten using the material director variation $\delta\mathbf{T}$ in the tangent plane $T_{\mathbf{E}_3}S^2$. Any $\delta\mathbf{T}\in T_{\mathbf{E}_3}S^2$, which when multiplied by the rotation matrix $\mathbf{\Lambda}$ gives the spatial director variation $\delta\mathbf{t}$, is defined as:

$$\delta\mathbf{t} = \mathbf{\Lambda}\delta\mathbf{\Theta}\times\mathbf{\Lambda}\mathbf{E}_3 = \tilde{\mathbf{\Lambda}}\delta\mathbf{T} \tag{3.52}$$

Where $\tilde{\mathbf{\Lambda}}$ are the first 2 columns of $\mathbf{\Lambda}$:

$$\tilde{\mathbf{\Lambda}} = \Lambda^i_\alpha \mathbf{E}_i\otimes\mathbf{E}^\alpha \tag{3.53}$$

Since the material director variation is perpendicular to $\mathbf{E}_3$, see Figure 3.7, the drill degree of freedom along $\mathbf{E}_3$ can be excluded allowing one to write:

$$\delta\mathbf{T} = \delta T^1\mathbf{E}_1 + \delta T^2\mathbf{E}_2 \tag{3.54}$$

Using the material director variation thus removes one nodal unknown from the system making it computationally favorable and the only reason it is used, note that even though it is called the *material* director variation it is unrelated to the undeformed or reference configuration. The actual spatial nodal director values are then given by:

$$\delta \mathbf{t}_A = \tilde{\mathbf{\Lambda}}_A \delta \mathbf{T}_A \tag{3.55}$$

where $\tilde{\mathbf{\Lambda}}_A$ is computed for all director nodes using equation 3.51. Using these nodal values, the director, its acceleration and variation are interpolated using shape functions L_A:

$$\mathbf{t}_h(\xi_1, \xi_2) = \sum_{A=1}^{N_T} L_A(\xi_1, \xi_2)\mathbf{t}_A = \sum_{A=1}^{n_T} L_A(\xi_1, \xi_2)\tilde{\mathbf{\Lambda}}_A \mathbf{T}_A \tag{3.56a}$$

$$\ddot{\mathbf{t}}_h(\xi_1, \xi_2) = \sum_{A=1}^{N_T} L_A(\xi_1, \xi_2)\ddot{\mathbf{t}}_A = \sum_{A=1}^{n_T} L_A(\xi_1, \xi_2)\tilde{\mathbf{\Lambda}}_A \ddot{\mathbf{T}}_A \tag{3.56b}$$

$$\delta\mathbf{t}(\xi_1, \xi_2) = \sum_{A=1}^{N_T} L_A(\xi_1, \xi_2)\delta\mathbf{t}_A = \sum_{A=1}^{n_T} L_A(\xi_1, \xi_2)\tilde{\mathbf{\Lambda}}_A \delta\mathbf{T}_A \tag{3.56c}$$

Where the shape functions are given by:

$$L_1 = (1 - \xi_1 - \xi_2) \tag{3.57a}$$

$$L_2 = \xi_1 \tag{3.57b}$$

$$L_3 = \xi_2 \tag{3.57c}$$

As before, the shape functions can be seen in Figure 3.8.

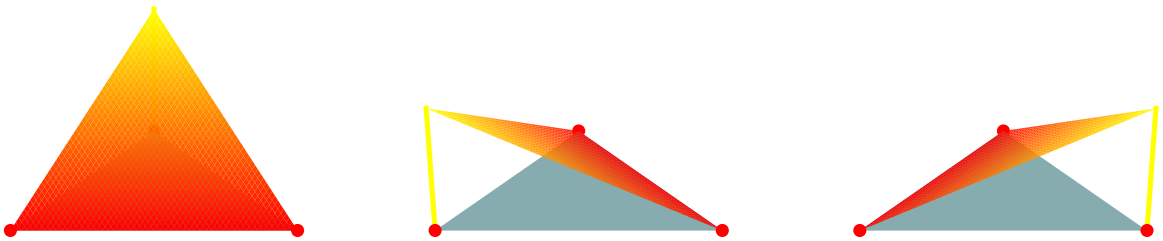

Figure 3.8: Shape functions L_A linear triangular element.

3.4. Stabilization and Consistency Terms

The *Principle of Virtual Power* is the first variation of the potential energy functional where standard Discontinuous Galerkin stabilization terms are included. The functional is defined as:

$$J_h(\mathcal{V}) = \int_{\mathcal{S}^0} \psi(\partial_\alpha \boldsymbol{\varphi}_h, \mathbf{t}_h, \partial_\alpha \mathbf{t}_h)\, d\mathcal{S} - W_{\text{Ext}}(\delta\mathcal{V}) + \frac{1}{2}\mathcal{W}_{\text{x, Stab}}(\boldsymbol{\varphi}_h, \delta\boldsymbol{\varphi}_h) + \frac{1}{2}\mathcal{W}_{\text{T, Stab}}(\mathbf{t}_h, \delta\mathbf{t}_h) \tag{3.58}$$

$\mathcal{W}_{\text{x, Stab}}$ and $\mathcal{W}_{\text{T, Stab}}$ are the stabilization terms added to the functional to ensure that elements do not move relative to their neighbor at the interface. The explicit expressions for all elemental stiffness matrices can be found in [19] and will not be repeated in this work, the only stiffness matrix that will be discussed here is the new out-of-plane interface stiffness matrix. These stabilization terms are used to define new connections between different layers, defined as the scalar products:

$$\mathcal{W}_{\text{x, Stab}}(\boldsymbol{\varphi}_h, \delta\boldsymbol{\varphi}_h) = \int_{\mathcal{S}} \frac{\beta_x}{h_e} [\![\boldsymbol{\varphi}_h]\!] \cdot [\![\delta\boldsymbol{\varphi}_h]\!]\, d\mathcal{S}, \quad \boldsymbol{\varphi}_h, \delta\boldsymbol{\varphi}_h \in \boldsymbol{X}_h \tag{3.59a}$$

$$\mathcal{W}_{\text{T, Stab}}(\mathbf{t}_h, \delta\mathbf{t}_h) = \int_{\mathcal{S}} \frac{\beta_T}{h_e} [\![\mathbf{t}_h]\!] \cdot [\![\delta\mathbf{t}_h]\!]\, d\mathcal{S}, \quad \mathbf{t}_h, \delta\mathbf{t}_h \in \boldsymbol{T}_h \tag{3.59b}$$

Jump and Average Operator

The jump operator captures the discontinuities in quantities, such as displacement, that naturally arise at the kth interface. The average operator calculates the mean value of these quantities at the kth interface, explicitly:

$$[\![\bullet]\!]^{(k)} = \left(\bullet^{(k)} - \bullet^{(k-1)}\right) \tag{3.60a}$$

$$\{\bullet\}^{(k)} = \frac{1}{2}\left(\bullet^{(k)} + \bullet^{(k-1)}\right) \tag{3.60b}$$

Where:

- h_e represents the characteristic mesh length, such as the length of an edge.
- $\beta_x = c_x \frac{Eh}{h_e}$ and $\beta_T = c_T \frac{Eh^3}{12h_e}$ are the penalty parameters, where h is the shell thickness, E is the Young's modulus, and c_x and c_T are sufficiently large positive constants.

The jump in mid-surface position and its variation can be written as:

$$[\![\boldsymbol{\varphi}_h]\!] = \sum_{A=1}^{n_x} N_A \left(\bar{\mathbf{x}}_A^{(k)} - \bar{\mathbf{x}}_A^{(k-1)}\right) = \sum_{A=1}^{n_x} N_A [\![\bar{\mathbf{x}}_A]\!] \tag{3.61a}$$

$$[\![\delta\boldsymbol{\varphi}]\!] = \sum_{A=1}^{n_x} N_A \left(\delta\bar{\mathbf{x}}_A^{(k)} - \delta\bar{\mathbf{x}}_A^{(k-1)}\right) = \sum_{A=1}^{n_x} N_A [\![\delta\bar{\mathbf{x}}_A]\!] \tag{3.61b}$$

Similarly, the jump in the director and its variation can be written as:

$$[\![\mathbf{t}_h]\!] = \sum_{A=1}^{n_T} L_A \tilde{\boldsymbol{\Lambda}}_A \left(\mathbf{T}_A^{(k)} - \mathbf{T}_A^{(k-1)}\right) = \sum_{A=1}^{n_T} L_A \tilde{\boldsymbol{\Lambda}}_A [\![\mathbf{T}_A]\!] \tag{3.62a}$$

$$[\![\delta\mathbf{t}_h]\!] = \sum_{A=1}^{n_T} L_A \tilde{\boldsymbol{\Lambda}}_A \left(\delta\mathbf{T}_A^{(k)} - \delta\mathbf{T}_A^{(k-1)}\right) = \sum_{A=1}^{n_T} L_A \tilde{\boldsymbol{\Lambda}}_A [\![\delta\mathbf{T}_A]\!] \tag{3.62b}$$

The elemental stabilization forces are obtained by inserting Equation 3.61 and Equation 3.62 into Equation 3.59:

$$[\mathbf{f}^e_{\mathrm{x,\,Stab}}]_A = \pm \int_{\mathcal{S}^e} \frac{\beta_x}{h_e} [\![\boldsymbol{\varphi}_h]\!] \, N_A \, d\mathcal{S} \tag{3.63a}$$

$$[\mathbf{f}^e_{\mathrm{T,\,Stab}}]_A = \pm \int_{\mathcal{S}^e} \left(\tilde{\boldsymbol{\Lambda}}_A\right)^T \frac{\beta_T}{h_e} [\![\mathbf{t}_h]\!] \, L_A \, d\mathcal{S} \tag{3.63b}$$

The elemental stiffness matrix for the new out-of-plane interface elements are then:

$$[\mathbf{k}^e_{\mathrm{xx,\,Stab}}]_{AB} = \pm \int_{\mathcal{S}^e} \frac{\beta_x}{h_e} N_A N_B \, d\mathcal{S} \tag{3.64a}$$

$$[\mathbf{k}^e_{\mathrm{TT,\,Stab}}]_{AB} = \pm \int_{\mathcal{S}^e} \frac{\beta_T}{h_e} L_A L_B \, d\mathcal{S} \tag{3.64b}$$

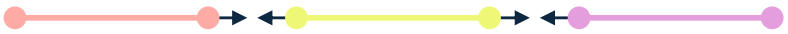

(a) Three beam elements with disconnected nodes and interface forces.

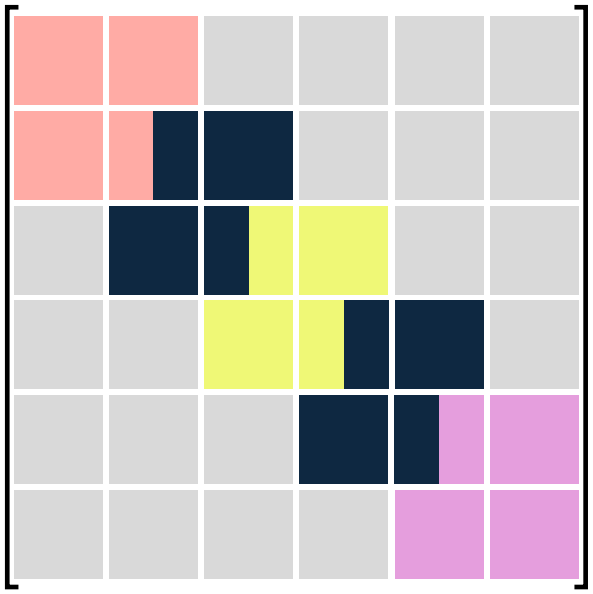

(b) Discontinuous Galerkin stiffness matrix representation of the structure above.

Figure 3.9: Discontinuous Galerkin including interface forces.

The stiffness matrix shown in Figure 3.3b lacks connections between elements needed to actually solve the system of equations. However, the elemental stiffness contribution for the out-of-plane interface elements adds these contributions. This is shown in Figure 3.9b, which is based on the structure in Figure 3.9a, where, as before, each block represents a 3×3 submatrix. The interface forces connect the elements and provide a simple approach to create cracks by simply removing these terms.

Note that these are new additions to the weak form, which work in tandem with the existing interface terms for in-plane connectivity. the main difference between these two interface terms is the integration domain, note that in this case its the entire surface $\mathcal{S}$ and not just line integrals over s. Equilibrium configurations are given by the stationary points of the discrete energy functional $J_h(\mathcal{V})$, e.g., first variations of the energy potential are equal to zero. The equilibrium equations follow from:

$$\langle DJ_h(\mathcal{V}), \delta\mathcal{V} \rangle = 0 \tag{3.65}$$

The first variation of the energy functional given in Equation 3.58, usually called the residual, is then given by:

$$\langle DJ_h(\mathcal{V}), \delta\mathcal{V}\rangle = \mathcal{W}_{\text{Int}}(\mathcal{V}, \delta\mathcal{V}) - \mathcal{W}_{\text{Ext}}(\delta\mathcal{V}) + \mathcal{W}_{\text{x, Stab}}(\boldsymbol{\varphi}_h, \delta\boldsymbol{\varphi}_h) + \mathcal{W}_{\text{T, Stab}}(\mathbf{t}_h, \delta\mathbf{t}_h) = 0, \quad \forall\delta\mathcal{V} \in \mathbb{V} \tag{3.66}$$

This equation is the virtual work equation for the geometrically exact shell that needs to be satisfied by all possible admissable variations $\delta\mathcal{V}$.

In the Discontinuous Galerkin method, additional terms naturally arise from integration by parts due to the use of discontinuous shape functions (see Appendix A). To handle these discontinuities effectively, fluxes at the interfaces between elements are introduced. These flux terms ensure that the weak form is consistent with the strong form of the PDE, so that when returning from the weak form to the strong form, the same solution is obtained. The inclusion of fluxes at the element boundaries ensures that the solution accurately represents the PDE across discontinuous interfaces, capturing the internal forces transmitted between adjacent elements. The consistency terms resulting from the derivation can be written as:

$$\pm \int_{\mathcal{S}} [\![\delta\boldsymbol{\varphi}_h]\!] \cdot \{\boldsymbol{P}\} \cdot \mathbf{t}\, \mu d\mathcal{S} \pm \int_{\mathcal{S}} [\![\delta\mathbf{t}_h]\!] \cdot \{\boldsymbol{P}\} \cdot \mathbf{t}\, \mu d\mathcal{S} \tag{3.67}$$

It is worth noting that these terms do not actually contribute to the weak form but are instead used to evaluate the material failure, the stabilization integrals are sufficient to keep the elements from physically separating.

3.5. Constitutive Law

The stress resultants acting on the shell element are given by:

$$\begin{Bmatrix} \widetilde{n}_{11} \\ \widetilde{n}_{22} \\ \widetilde{n}_{12} \\ \widetilde{n}_{21} \\ \widetilde{m}_{11} \\ \widetilde{m}_{22} \\ \widetilde{m}_{12} \\ \widetilde{m}_{21} \\ \widetilde{q}_1 \\ \widetilde{q}_2 \end{Bmatrix} = \int_{-\frac{h}{2}}^{\frac{h}{2}} \begin{Bmatrix} \bar{\mathbf{S}}_{11}\left(1+\frac{\xi_3}{R_2}\right) \\ \bar{\mathbf{S}}_{22}\left(1+\frac{\xi_3}{R_1}\right) \\ \bar{\mathbf{S}}_{12}\left(1+\frac{\xi_3}{R_1}\right) \\ \bar{\mathbf{S}}_{12}\left(1+\frac{\xi_3}{R_2}\right) \\ \xi_3\bar{\mathbf{S}}_{11}\left(1+\frac{\xi_3}{R_2}\right) \\ \xi_3\bar{\mathbf{S}}_{22}\left(1+\frac{\xi_3}{R_1}\right) \\ \xi_3\bar{\mathbf{S}}_{12}\left(1+\frac{\xi_3}{R_1}\right) \\ \xi_3\bar{\mathbf{S}}_{12}\left(1+\frac{\xi_3}{R_2}\right) \\ \kappa\bar{\mathbf{S}}_{13}\left(1+\frac{\xi_3}{R_2}\right) \\ \kappa\bar{\mathbf{S}}_{23}\left(1+\frac{\xi_3}{R_1}\right) \end{Bmatrix} d\xi_3 \tag{3.68}$$

In general, for shells $\widetilde{n}_{\alpha\beta} \neq \widetilde{n}_{\beta\alpha}$, and similarly $\widetilde{m}_{\alpha\beta} \neq \widetilde{m}_{\beta\alpha}$. However, for shallow shells the terms $\frac{\xi_3}{R_1}$ and $\frac{\xi_3}{R_2}$ can be neglected [33]:

$$\begin{Bmatrix} \widetilde{n}_{11} \\ \widetilde{n}_{22} \\ \widetilde{n}_{12} \\ \widetilde{m}_{11} \\ \widetilde{m}_{22} \\ \widetilde{m}_{12} \\ \widetilde{q}_1 \\ \widetilde{q}_2 \end{Bmatrix} = \int_{-\frac{h}{2}}^{\frac{h}{2}} \begin{Bmatrix} \bar{\mathbf{S}}_{11} \\ \bar{\mathbf{S}}_{22} \\ \bar{\mathbf{S}}_{12} \\ \xi_3\bar{\mathbf{S}}_{11} \\ \xi_3\bar{\mathbf{S}}_{22} \\ \xi_3\bar{\mathbf{S}}_{12} \\ \kappa\bar{\mathbf{S}}_{13} \\ \kappa\bar{\mathbf{S}}_{23} \end{Bmatrix} d\xi_3 \tag{3.69}$$

3.5.1. Isotropic Material

The free energy $\psi(\partial_\alpha \boldsymbol{\varphi}_h, \mathbf{t}_h, \partial_\alpha \mathbf{t}_h)$ can be thought of as consisting of membrane, shear, and bending strain energies:

$$\psi(\partial_\alpha \boldsymbol{\varphi}_h, \mathbf{t}_h, \partial_\alpha \mathbf{t}_h) = \psi_m(\epsilon_{\alpha\beta}) + \psi_s(\zeta_\alpha) + \psi_b(\rho_{\alpha\beta}) \tag{3.70}$$

As usual these individual strain energies are quadratic in the corresponding strains:

$$\psi_m = \frac{h}{2}\epsilon_{\alpha\beta}C_{\alpha\beta\gamma\delta}\epsilon_{\gamma\delta} \tag{3.71a}$$

$$\psi_b = \frac{1}{2}\frac{h^3}{12}\rho_{\alpha\beta}C_{\alpha\beta\gamma\delta}\rho_{\gamma\delta} \tag{3.71b}$$

$$\psi_s = \frac{h}{2}\kappa G\zeta_\alpha a^{0\alpha\beta}\zeta_\beta \tag{3.71c}$$

Where h is the thickness, μ is the shear modulus, κ is the shear reduction coefficient, and $C_{\alpha\beta\gamma\delta}$ is the plane stress elastic tensor given by:

$$C_{\alpha\beta\gamma\delta} = \frac{\mu}{2}(a^{0\alpha\gamma}a^{0\beta\delta} + a^{0\alpha\delta}a^{0\beta\gamma}) + \frac{E\nu}{1-\nu^2}a^{0\alpha\beta}a^{0\gamma\delta} \tag{3.72}$$

Where $a^{0\alpha\beta}$ is the inverse of the metric tensor in the reference configuration. The stress resultants are related to the free energy based on the following definitions:

$$\widetilde{n}_{\alpha\beta} = 2\frac{\partial \psi}{\partial a_{\alpha\beta}} \tag{3.73a}$$

$$\widetilde{m}_{\alpha\beta} = \frac{\partial \psi}{\partial \kappa_{\alpha\beta}} \tag{3.73b}$$

$$\widetilde{q}_{\alpha} = \frac{\partial \psi}{\partial \gamma_{\alpha}} \tag{3.73c}$$

However, since the geometry is already accounted for when calculating the strains through the kinematic assumptions, the standard constitutive law can be applied directly:

$$S_{\alpha\beta} = C_{\alpha\beta\gamma\delta} E_{\gamma\delta} \tag{3.74}$$

In plane stress ($S_{33} = 0$), the stiffness matrix is written as:

$$\boldsymbol{C} = \frac{E}{(1-\nu^2)} \begin{bmatrix} 1 & \nu & 0 & 0 & 0 \\ \nu & 1 & 0 & 0 & 0 \\ 0 & 0 & \frac{1-\nu}{2} & 0 & 0 \\ 0 & 0 & 0 & \frac{1-\nu}{2} & 0 \\ 0 & 0 & 0 & 0 & \frac{1-\nu}{2} \end{bmatrix} \tag{3.75}$$

The expressions for the stress resultants then become:

$$\widetilde{n}_{\alpha\beta} = hC_{\alpha\beta\gamma\delta}\epsilon_{\gamma\delta} \tag{3.76a}$$

$$\widetilde{m}_{\alpha\beta} = \frac{h^3}{12} C_{\alpha\beta\gamma\delta}\rho_{\gamma\delta} \tag{3.76b}$$

$$\widetilde{q}_{\alpha} = h\kappa\mu\zeta_{\alpha} \tag{3.76c}$$

Where $\mu = \frac{E}{2(1+\nu)}$ is the shear modulus. Combining all stress resultants into a vector, this can be expressed as:

$$\begin{Bmatrix} \widetilde{n}_{11} \\ \widetilde{n}_{22} \\ \widetilde{n}_{12} \\ \widetilde{m}_{11} \\ \widetilde{m}_{22} \\ \widetilde{m}_{12} \\ \widetilde{q}_{1} \\ \widetilde{q}_{2} \end{Bmatrix} = \begin{bmatrix} A_{11} & \nu A_{11} & 0 & 0 & 0 & 0 & 0 & 0 \\ \nu A_{11} & A_{11} & 0 & 0 & 0 & 0 & 0 & 0 \\ 0 & 0 & \frac{1-\nu}{2}A_{11} & 0 & 0 & 0 & 0 & 0 \\ 0 & 0 & 0 & D_{11} & \nu D_{11} & 0 & 0 & 0 \\ 0 & 0 & 0 & \nu D_{11} & D_{11} & 0 & 0 & 0 \\ 0 & 0 & 0 & 0 & 0 & \frac{1-\nu}{2}D_{11} & 0 & 0 \\ 0 & 0 & 0 & 0 & 0 & 0 & h\kappa\mu & 0 \\ 0 & 0 & 0 & 0 & 0 & 0 & 0 & h\kappa\mu \end{bmatrix} \begin{Bmatrix} \epsilon_{11} \\ \epsilon_{22} \\ 2\epsilon_{12} \\ \rho_{11} \\ \rho_{22} \\ 2\rho_{12} \\ \zeta_{1} \\ \zeta_{2} \end{Bmatrix} \tag{3.77}$$

Where:

$$A_{11} = \frac{Eh}{1-\nu^2}, \quad D_{11} = \frac{Eh^3}{12(1-\nu^2)} \tag{3.78}$$

3.5.2. Composite Material

The constitutive lamina compliance matrix for orthotropic material is given as:

$$\boldsymbol{S} = \begin{bmatrix} \frac{1}{E_1} & -\frac{\nu_{21}}{E_2} & -\frac{\nu_{31}}{E_3} & 0 & 0 & 0 \\ -\frac{\nu_{12}}{E_1} & \frac{1}{E_2} & -\frac{\nu_{32}}{E_3} & 0 & 0 & 0 \\ -\frac{\nu_{13}}{E_1} & -\frac{\nu_{23}}{E_2} & \frac{1}{E_3} & 0 & 0 & 0 \\ 0 & 0 & 0 & \frac{1}{G_{23}} & 0 & 0 \\ 0 & 0 & 0 & 0 & \frac{1}{G_{13}} & 0 \\ 0 & 0 & 0 & 0 & 0 & \frac{1}{G_{12}} \end{bmatrix} \tag{3.79}$$

Here, E_1, E_2, and E_3 represent the Young's moduli in the principal material directions, ν_{12}, ν_{23}, and ν_{13} are the corresponding Poisson's ratios, and G_{12}, G_{23}, and G_{13} are the shear moduli for the respective planes. The compliance matrix can be split in two parts, the first of which corresponds to in-plane strains:

$$\boldsymbol{S} = \begin{bmatrix} \frac{1}{E_1} & -\frac{\nu_{21}}{E_2} & 0 \\ -\frac{\nu_{12}}{E_1} & \frac{1}{E_2} & 0 \\ 0 & 0 & \frac{1}{G_{12}} \end{bmatrix} \tag{3.80}$$

Now taking the inverse of this matrix results in:

$$\boldsymbol{Q} = \begin{bmatrix} \frac{E_1}{(1-\nu_{12}\nu_{21})} & \frac{\nu_{21}E_1}{(1-\nu_{12}\nu_{21})} & 0 \\ \frac{\nu_{12}E_2}{(1-\nu_{12}\nu_{21})} & \frac{E_2}{(1-\nu_{12}\nu_{21})} & 0 \\ 0 & 0 & G_{12} \end{bmatrix} \tag{3.81}$$

These are the equations for a transversely isotropic lamina in the the material coordinates, however, in the global laminate coordinates the stiffness matrix components are given by [33]:

$$\bar{Q}_{11} = Q_{11}\cos^4(\theta) + 2(Q_{12} + 2Q_{66})\cos^2(\theta)\sin^2(\theta) + Q_{22}\sin^4(\theta) \tag{3.82a}$$
$$\bar{Q}_{12} = (Q_{11} + Q_{22} - 4Q_{66})\cos^2(\theta)\sin^2(\theta) + Q_{12}(\sin^4(\theta) + \cos^4(\theta)) \tag{3.82b}$$
$$\bar{Q}_{22} = Q_{11}\sin^4(\theta) + 2(Q_{12} + 2Q_{66})\sin^2(\theta)\cos^2(\theta) + Q_{22}\cos^4(\theta) \tag{3.82c}$$
$$\bar{Q}_{16} = (Q_{11} - Q_{12} - 2Q_{66})\sin(\theta)\cos^3(\theta) + (Q_{12} - Q_{22} + 2Q_{66})\sin^3(\theta)\cos(\theta) \tag{3.82d}$$
$$\bar{Q}_{26} = (Q_{11} - Q_{12} - 2Q_{66})\sin^3(\theta)\cos(\theta) + (Q_{12} - Q_{22} + 2Q_{66})\sin(\theta)\cos^3(\theta) \tag{3.82e}$$
$$\bar{Q}_{66} = (Q_{11} + Q_{22} - 2Q_{12} - 2Q_{66})\sin^2(\theta)\cos^2(\theta) + Q_{66}(\sin^4(\theta) + \cos^4(\theta)) \tag{3.82f}$$

Finally, the stiffness matrix components corresponding to the out of plane shear strains are given in laminate coordinates by [33]:

$$\bar{Q}_{44} = Q_{44}\cos^2(\theta) + Q_{55}\sin^2(\theta) \tag{3.83a}$$
$$\bar{Q}_{45} = (Q_{55} - Q_{44})\cos(\theta)\sin(\theta) \tag{3.83b}$$
$$\bar{Q}_{55} = Q_{44}\sin^2(\theta) + Q_{55}\cos^2(\theta) \tag{3.83c}$$

Combining this into the well-known and loved ABD matrix using Equation 3.69 [33]:

$$\begin{Bmatrix} \widetilde{n}_{11} \\ \widetilde{n}_{22} \\ \widetilde{n}_{12} \\ \widetilde{m}_{11} \\ \widetilde{m}_{22} \\ \widetilde{m}_{12} \\ \widetilde{q}_1 \\ \widetilde{q}_2 \end{Bmatrix} = \begin{bmatrix} A_{11} & A_{12} & A_{16} & B_{11} & B_{12} & B_{16} & 0 & 0 \\ A_{12} & A_{22} & A_{26} & B_{12} & B_{22} & B_{26} & 0 & 0 \\ A_{16} & A_{26} & A_{66} & B_{16} & B_{26} & B_{66} & 0 & 0 \\ B_{11} & B_{12} & B_{16} & D_{11} & D_{12} & D_{16} & 0 & 0 \\ B_{12} & B_{22} & B_{26} & D_{12} & D_{22} & D_{26} & 0 & 0 \\ B_{16} & B_{26} & B_{66} & D_{16} & D_{26} & D_{66} & 0 & 0 \\ 0 & 0 & 0 & 0 & 0 & 0 & A_{55} & A_{45} \\ 0 & 0 & 0 & 0 & 0 & 0 & A_{45} & A_{44} \end{bmatrix} \begin{Bmatrix} \epsilon_{11} \\ \epsilon_{22} \\ 2\epsilon_{12} \\ \rho_{11} \\ \rho_{22} \\ 2\rho_{12} \\ \zeta_1 \\ \zeta_2 \end{Bmatrix} \tag{3.84}$$

In this work, only symmetric laminates are modeled, with each lamina represented as a single orthotropic layer. This approach simplifies the expression described above:

$$A_{ij} = \bar{Q}_{ij} h, \quad B_{ij} = 0, \quad D_{ij} = \frac{\bar{Q}_{ij} h^3}{12}, \quad A_{44} = \bar{Q}_{44} h, \quad A_{45} = \bar{Q}_{45} h, \quad A_{55} = \bar{Q}_{55} h \tag{3.85}$$

The $\boldsymbol{B}$ matrix thus disappears from the formulation, the offset of the layers is taken into account in the $\boldsymbol{D}$ matrix. The corresponding strain energy terms are:

$$\psi_m = \frac{1}{2} \epsilon_{\alpha\beta} \widetilde{n}_{\alpha\beta} \tag{3.86a}$$

$$\psi_b = \frac{1}{2} \rho_{\alpha\beta} \widetilde{m}_{\alpha\beta} \tag{3.86b}$$

$$\psi_s = \frac{1}{2} \zeta_\alpha \widetilde{q}_\alpha \tag{3.86c}$$

3.6. Implementation

3.6.1. Creation of new layers

In this work, the process of generating multiple layers for shell elements is designed to avoid the need for manual updates to the mesh file for each configuration. Initially, the mesh for the first layer of elements is created using Gmsh, serving as the foundational mesh upon which all subsequent layers are based. For cases where only a single layer is required, the additions developed in this thesis remain unused. However, if more than one layer is requested, the program enters a loop to continuously generate additional layers until the maximum requested number is reached.

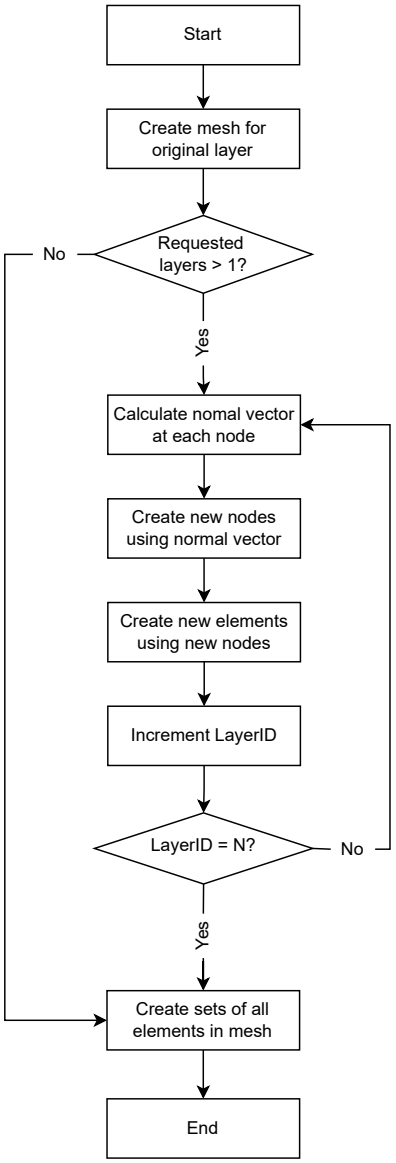

Figure 3.10: Flow chart illustrating the process of creating new layers.

For each new layer, the program calculates the normal vector at each node of the existing mesh. This normal vector is used to offset the node positions according to the specified layer thickness, ensuring that the method is applicable to shell structures of any shape or curvature. New nodes are created based on this offset, and these new nodes are then used to define new elements corresponding to the additional layer. After each iteration, the new layer ID is incremented, and the process is checked to

ensure that the correct number of layers has been generated (i.e., when the layer ID equals the desired number of layers N).

Once the desired number of layers has been reached, interface elements are created between all layers to model the interaction between them. The creation of interface elements follows a similar process as for the layers, offsetting nodes and creating elements, with the primary difference being that the new nodes are offset to sit between the newly created bulk elements. Finally, a set of all newly created out-of-plane interface elements is generated. The entire process is summarized in Figure 3.10.

3.6.2. Inertia Correction

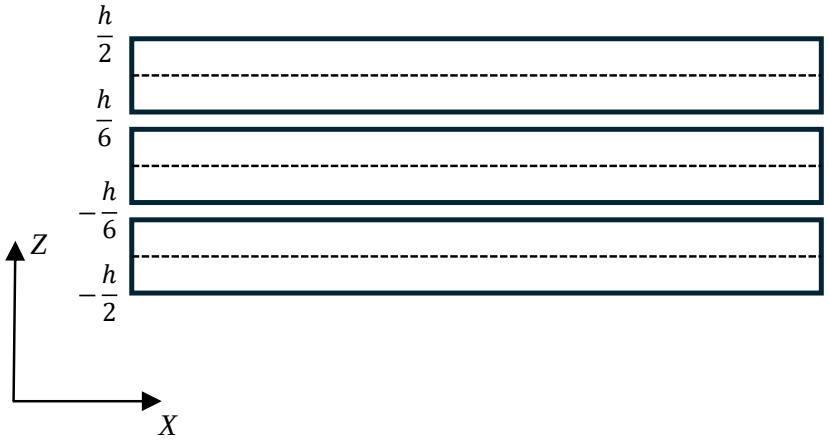

Figure 3.11: Inertia correction.

Section 3.2 introduced the variables $\bar{\rho}$ and $\bar{I}$ without giving explicit representations, that is because it depends on the number of layers to be modeled. $\bar{\rho}^0$ denotes the translational inertia, and $\bar{I}$ represents the rotary inertia, they are integrated over the thickness of the laminate, from $-h/2$ to $h/2$.

$$\bar{\rho} = \int_h \rho^0 \, d\xi_3 \tag{3.87a}$$

$$\bar{I} = \int_h \rho^0 \xi_3^2 \, d\xi_3 \tag{3.87b}$$

$$\bar{\rho} = \int_{-\frac{h}{2}}^{\frac{h}{2}} \rho^0 \, d\xi_3 = \left(\int_{-\frac{h}{2}}^{-\frac{h}{6}} \rho^0 \, d\xi_3 + \int_{-\frac{h}{6}}^{\frac{h}{6}} \rho^0 \, d\xi_3 + \int_{\frac{h}{6}}^{\frac{h}{2}} \rho^0 \, d\xi_3 \right) = \rho^0 h \tag{3.88a}$$

$$\bar{I} = \int_{-\frac{h}{2}}^{\frac{h}{2}} \rho^0 \xi_3^2 \, d\xi_3 = \left(\int_{-\frac{h}{2}}^{-\frac{h}{6}} \rho^0 \xi_3^2 \, d\xi_3 + \int_{-\frac{h}{6}}^{\frac{h}{6}} \rho^0 \xi_3^2 \, d\xi_3 + \int_{\frac{h}{6}}^{\frac{h}{2}} \rho^0 \xi_3^2 \, d\xi_3 \right) = \frac{\rho^0 h^3}{12} \tag{3.88b}$$

This can be rewritten using the parallel axis theorem, the rotational inertia must be calculated with respect to a common mid-surface. This theorem is expressed as:

$$\bar{I} = I_c + \rho^0 h d^2 \tag{3.89}$$

In this equation, I_c is the rotational inertia about each shells's own mid-surface, $\rho^0 h$ is the density per unit thickness of each shell, and d is the distance from each shell's mid-surface to the common mid-surface.

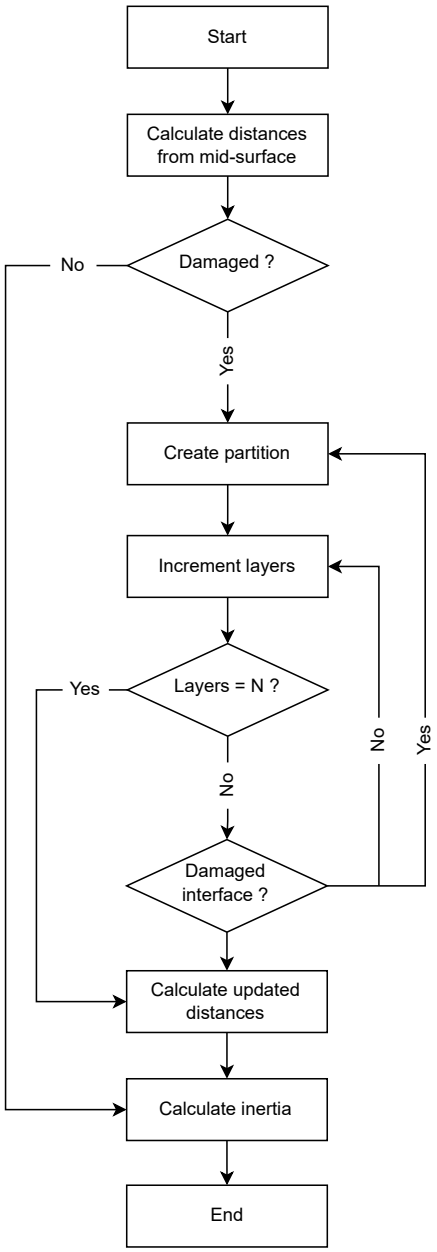

Figure 3.12: Flow chart illustrating the proposed computational workflow for the rotational inertia calculation in multi-layered structures.

Before the simulation begins, the inertia for all elements within the thickness is calculated, assuming no damage. This calculation uses the predefined thickness, inertia ($\bar{I}$), and density per unit thickness (m), determining the inertia with respect to each layer's mid-surface. If damage were present, the calculation would need to be updated for all elements within the thickness, as damage to one element would affect the inertia of all layers within the partition it belongs to. For example, in a scenario with three layers, see Figure 3.11, if the second interface were damaged, the structure would be divided into two partitions: one with two layers and one with a single layer. The distance to the mid-plane of each partition would then be updated accordingly. The process for calculating inertia with damaged interfaces involves two main steps. First, the number of partitions is identified by iterating through the layers and checking for damaged interfaces. Partitions are sections of layers separated by damaged interfaces. Starting at the bottom, the process increments the current partition count for each layer until a damaged interface is encountered or the top layer is reached. This partition is then stored, and the count is reset for the next partition. Second, the inertia for each element within the identified partitions is recalculated. This

involves iterating through the partitions and calculating the distance to the mid-plane of each partition, starting from the bottom layer. For each layer in the partition, the element inertia is updated using the rotary inertia, the calculated distance squared, and the density per unit thickness. This ensures that the inertia is accurately calculated with respect to the common mid-surface for each partition. Although the current model assumes no damage, this two-step process would be crucial for maintaining accurate inertia calculations in the presence of damage, ensuring that the simulation results remain reliable. The proposed computational workflow is illustrated in Figure 3.12.

3.6.3. The Four Pillars of Summit

C++ was selected for its support of Object-Oriented Programming (OOP) paradigms, which are extremely beneficial. The language's object-oriented features—such as abstraction, encapsulation, inheritance, and polymorphism—enable efficient organization and manipulation of complex algorithms essential for finite element simulations. For instance, the weak form can be split into separate files, each responsible for calculating its own contribution, rather than implementing all calculations within a single, monolithic file. This approach allows the finite element framework summit to maintain a modular and easily extensible codebase, which was crucial for adding the out-of-plane contribution. An overview of summit is given in Figure 3.13.

Summit

The finite element framework employed in this research is known as summit, it contains the geometrically exact shell element developed by researchers at the Massachusetts Institute of Technology, primarily by Talamini and Radovitzky. Summit is implemented in C++, an OOP language that is well-suited for high-performance computational tasks.

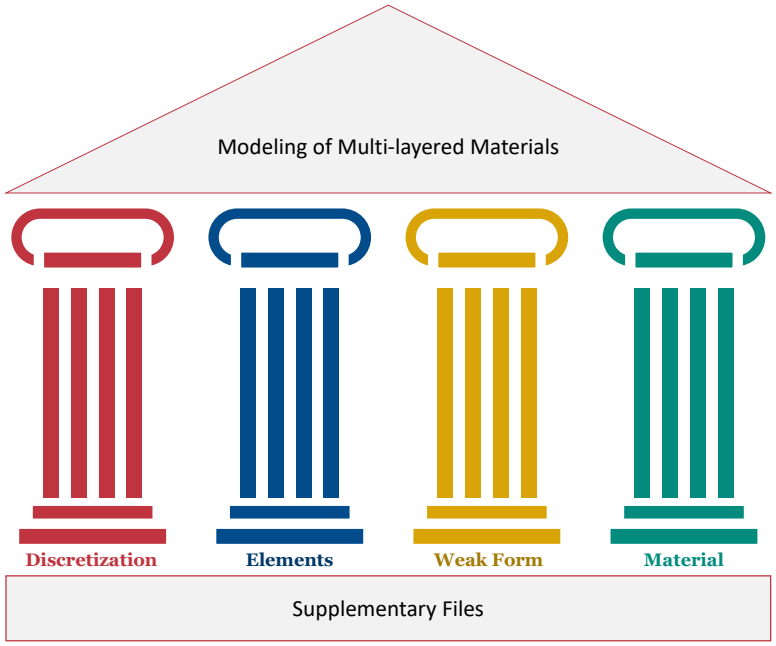

Figure 3.13: The four pillars of summit that form the foundation of this work.

- **Discretization:** Refers to the process of creating new layers within the multi-layered structure using the Discontinuous Galerkin method.
- **Elements:** Refers to the geometrically exact shell element utilized along with the corresponding interface elements.
- **Weak Form:** Refers to the contribution of the new out-of-plane stabilization terms from Equation 3.59.
- **Material:** Refers to the isotropic material and the newly implemented composite material.

3.7. Solving Incremental Variations

3.7.1. Iterative Newton Solver

For a nonlinear system of equations $\langle DJ_h(\mathcal{V}), \delta\mathcal{V}\rangle = 0$, writing the increment $\Delta\mathcal{U} := (\Delta\mathbf{u}, \Delta\mathbf{t})$, the linearized system is then given by:

$$\langle DJ_h(\mathcal{V}), \delta\mathcal{V}\rangle + \langle D^2J_h(\mathcal{V}), \delta\mathcal{V}, \Delta\mathcal{U}\rangle = 0, \quad \forall\delta\mathcal{V} \in \mathbb{V} \tag{3.90}$$

The tangent stiffness matrix $\boldsymbol{K}$ represents the linearization of the system of equations around an initial estimate. Using the Newton-Raphson method, the correction $\Delta\mathcal{U}$ is obtained by solving the system:

$$\langle D^2J_h(\mathcal{V}), \delta\mathcal{V}, \Delta\mathcal{U}\rangle = -\langle DJ_h(\mathcal{V}), \delta\mathcal{V}\rangle \tag{3.91}$$

D^2J_h corresponds to the second variation of the energy functional J_h, and is used to define the tangent stiffness matrix. This leads to a bilinear form:

$$\langle D^2J_h(\mathcal{V}), \delta\mathcal{V}, \Delta\mathcal{U}\rangle = \delta\mathcal{V}^T\boldsymbol{K}\Delta\mathcal{U} \tag{3.92}$$

Where:

$$\Delta\mathcal{U} := \begin{bmatrix} \Delta\mathbf{u}_1 \\ \Delta\mathbf{T}_1 \\ \vdots \\ \Delta\mathbf{u}_{N_x} \\ \Delta\mathbf{T}_{N_T} \end{bmatrix} \tag{3.93}$$

Each nodal $\Delta\mathbf{u}_i$ is a 3×1 vector and each nodal $\Delta\mathbf{T}_i$ is a 2×1 vector. Therefore, the combined elemental vector is 24×1, considering there are six displacement nodes and three director nodes. As usual the tangent stiffness matrix consists of a material part and a geometric part, however, a third part related to the stability term also exists:

$$\boldsymbol{K} = \boldsymbol{K}^{\text{Mat}} + \boldsymbol{K}^{\text{Geo}} + \boldsymbol{K}^{\text{Stab}} \tag{3.94}$$

3.7.2. Time Integration

Substituting the field interpolations into the principle of virtual power, as shown in Section 3.2, results in the following two expressions:

$$\sum_{B=1}^{N_X} \mathbf{M}_{AB}\ddot{\bar{\mathbf{x}}}_B = \left[\mathbf{f}_{\text{x, Ext}}(t)\right]_A - \left[\mathbf{f}_{\text{x, Int}}\left(\bar{\mathbf{x}}_B, \dot{\bar{\mathbf{x}}}_B\right)\right]_A - \left[\mathbf{f}_{\text{x, Stab}}\left(\bar{\mathbf{x}}_B\right)\right]_A, \quad \forall A \in [1, N_X], \quad \forall t \in T \tag{3.95a}$$

$$\sum_{B=1}^{N_T} \mathbf{I}_{AB}\ddot{\mathbf{T}}_B = \left[\mathbf{f}_{\text{T, Ext}}(t)\right]_A - \left[\mathbf{f}_{\text{T, Int}}\left(\mathbf{t}_B, \dot{\mathbf{t}}_B\right)\right]_A - \left[\mathbf{f}_{\text{T, Stab}}\left(\mathbf{t}_B\right)\right]_A, \quad \forall A \in [1, N_T], \quad \forall t \in T \tag{3.95b}$$

In the following incremental displacements $\Delta\mathbf{u}_B$ are defined as $\bar{\mathbf{x}}_B^{n+1} - \bar{\mathbf{x}}_B^n$. The incremental displacement and the velocity predictor are marched in time using:

$$\Delta\mathbf{u}_B = \Delta t\dot{\bar{\mathbf{x}}}_B^n + \frac{1}{2\Delta t^2}\ddot{\bar{\mathbf{x}}}_B^n \tag{3.96a}$$

$$\dot{\bar{\mathbf{x}}}_B^{n+1} = \dot{\bar{\mathbf{x}}}_B^n + (1-\gamma)\Delta t\ddot{\bar{\mathbf{x}}}_B^n \tag{3.96b}$$

The nodal accelerations are then solved for using these quantities:

$$\sum_{A=1}^{N_x} \mathbf{M}_{AB}\ddot{\bar{\mathbf{x}}}_B^{n+1} = \left[\mathbf{f}_{\text{x, Ext}}\left(t^{n+1}\right)\right]_A - \left[\mathbf{f}_{\text{x, Int}}\left(\bar{\mathbf{x}}_B^{n+1}, \dot{\bar{\mathbf{x}}}_B^{n+1}\right)\right]_A - \left[\mathbf{f}_{\text{x, Stab}}\left(\bar{\mathbf{x}}_B^{n+1}\right)\right]_A \tag{3.97}$$

Here, a lumped mass matrix is used to avoid having to invert the mass matrix. Finally, the corrector is applied to the velocities as follows:

$$\dot{\mathbf{x}}_B^{n+1} = \dot{\mathbf{x}}_B^n + (1-\gamma)\Delta t \ddot{\mathbf{x}}_B^n + \gamma \Delta t \ddot{\mathbf{x}}_B^{n+1} \tag{3.98}$$

Second order accuracy is only obtained when γ is set to $\frac{1}{2}$, this corresponds to an explicit Newmark integration scheme, also known as the central difference method. The same approach is used to obtain the incremental material director variations $\Delta \mathbf{T}_B$ defined as $\mathbf{T}_B^{n+1} - \mathbf{T}_B^n$, and the predicted material velocity:

$$\Delta \mathbf{T}_B = \Delta t \dot{\mathbf{T}}_B^n + \frac{1}{2\Delta t^2} \ddot{\mathbf{T}}_B^n \tag{3.99a}$$

$$\dot{\mathbf{T}}_B^{n+1} = \dot{\mathbf{T}}_B^n + (1-\gamma)\Delta t \, \dot{\mathbf{T}}_B^n \tag{3.99b}$$

At this point the kinematic update algorithm is used to obtain the new director $\mathbf{t}_B^{n+1}$ and rotation matrix $\mathbf{\Lambda}_B^{n+1}$. The spatial director velocity is obtained by multiplying with the rotation matrix $\mathbf{\Lambda}_B^{n+1} \in \mathrm{SO}(3)$:

$$\dot{\mathbf{t}}_B^{n+1} = \mathbf{\Lambda}_B^{n+1} \dot{\mathbf{T}}_B^{n+1} \tag{3.100}$$

And the material accelerations are solved for using:

$$\sum_{B=1}^{N_T} \mathbf{I}_{AB} \ddot{\mathbf{T}}_B = \left[\mathbf{f}_{\mathrm{T,\,Ext}} \left(t^{n+1} \right) \right]_A - \left[\mathbf{f}_{\mathrm{T,\,Int}} \left(\mathbf{t}_B^{n+1}, \dot{\mathbf{t}}_B^{n+1} \right) \right]_A - \left[\mathbf{f}_{\mathrm{T,\,Stab}} \left(\dot{\mathbf{t}}_B^{n+1} \right) \right]_A \tag{3.101}$$

The final step is correcting the material velocity using:

$$\dot{\mathbf{T}}_A^{n+1} = \dot{\mathbf{T}}_B^n + (1-\gamma)\Delta t \, \dot{\mathbf{T}}_B^n + (1-\gamma)\Delta t \, \ddot{\mathbf{T}}_A^{n+1} \tag{3.102}$$

It can be seen that the process is the same for both the displacements and material director, hence, both are combined in a single vector for computational ease.

Stable Time Step

The stability of the numerical system relies on choosing a time step that is smaller than a specified maximum value. This critical time step is determined using the material's celerity c, which represents the speed of sound in the material, the characteristic mesh length h_e and the density ρ. The formula for the critical time step is given by:

$$\Delta t \leqslant \Delta t_{\mathrm{crit}} = \beta \frac{h_e}{c} \tag{3.103}$$

In this equation, β is an additional safety factor introduced by the Discontinuous Galerkin method, it ranges from 0 to 1 and is determined by $\frac{1}{\sqrt{max(c_x, c_T)}}$. The Discontinuous Galerkin method thus imposes a stricter time step size constraint on top of the significant increase in the number of nodes and resulting degrees of freedom, this is somewhat mitigated by the method's high scalability. However, this scalability is not investigated in this work.

For isotropic materials, the celerity c is defined as:

$$c = \sqrt{\frac{B}{\rho}} = \sqrt{\frac{\frac{E}{1-\nu^2}}{\rho}} \tag{3.104}$$

Where:

- $B = \frac{E}{1-\nu^2}$ is the effective modulus under plane stress conditions.
- E is the Young's modulus.
- ν is the Poisson's ratio.
- ρ is the material's density.

For composite materials the longitudinal speed of sound c in a composite material can be calculated using an equivalent elastic modulus which takes into account the material's longitudinal and transverse modulus, shear modulus, and plane stress or strain condition [17]. This equivalent modulus replaces the isotropic elastic modulus in the equation for wave speed, assuming plane stress:

$$B = \frac{1}{\sqrt{\frac{S_{11}S_{33}}{2}}\sqrt{\sqrt{\frac{S_{33}}{S_{11}}} + \frac{2S_{31}+S_{55}}{2S_{11}}}} \tag{3.105}$$

Where S_{ij} are the compliance matrix components.

3.8. Kinematic Update

The exponential mapping is used to map director variations $\Delta\mathbf{t}_A \in S^2$ onto the unit sphere S^2, thus enforcing the unit length constraint by design. Given any point $\mathbf{t}_A^k \in S^2$ and corresponding variation $\Delta\mathbf{t}_A \in T_{\mathbf{t}_A^k} S^2$ there exists a unique arc which start at $\mathbf{t}_A^k$ and tangent to $\Delta\mathbf{t}_A \in T_{\mathbf{t}_A^k} S^2$ at $\mathbf{t}_A^k$. Essentially the variation $\Delta\mathbf{t}_A$ results in straight lines starting from $\mathbf{t}_A^k$ in the direction of $\Delta\mathbf{t}_A$ and the exponential mapping projects this straight line onto the unit circle resulting in an arc equal to the rotation angle in radians since the radius is one [41].

The derivation of the exponential map can be found in Appendix C.3, the equation might look complex at first but becomes easier when noticing that $\mathbf{t}_A^{k+1}$ lies in the plane spanned by $\mathbf{t}_A^k$ and $\frac{\Delta\mathbf{t}_A}{\|\Delta\mathbf{t}_A\|}$. Figure 3.14 illustrates this intuitively. From this, it can be shown that:

$$\mathbf{t}_A^k \cdot \mathbf{t}_A^{k+1} = \cos\|\Delta\mathbf{t}_A\| \tag{3.106a}$$

$$\frac{\Delta\mathbf{t}_A}{\|\Delta\mathbf{t}_A\|} \cdot \mathbf{t}_A^{k+1} = \sin\|\Delta\mathbf{t}_A\| \tag{3.106b}$$

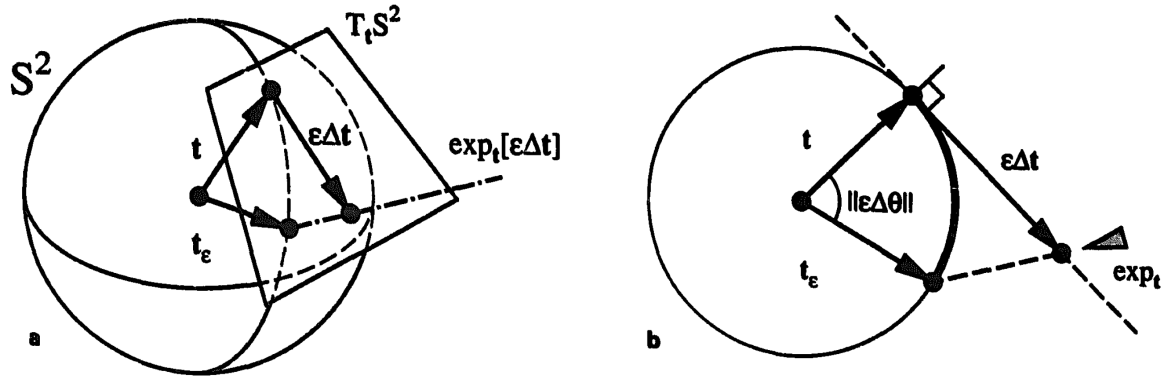

Figure 3.14: (a) The geodesic starting at $\mathbf{t}_A^k \in S^2$ and tangent to $\Delta\mathbf{t}_A \in T_{\mathbf{t}_A^k} S^2$. This curve, which is an arc of great circle, is the image of the straight line $\mathbf{t}_A^k + \varepsilon\Delta\mathbf{t}_A$. (b) 2D representation of the exponential map [41].

The process of updating the nodal director field, using director increments determined in Section 3.7, can be understood geometrically as following the director along the unit sphere S^2. During each iteration k, the director $\mathbf{t}_A^k \in S^2$ is updated based on the given increment $\Delta\mathbf{t}_A \in T_{\mathbf{t}_A^k} S^2$ and the previous director using the exponential map $\exp_{\mathbf{t}_A^k} : T_{\mathbf{t}_A^k} S^2 \to S^2$. Each director node has its own unit sphere on which it can trace curves made up of arcs of geodesics (great circles) on S^2. Since no assumptions about the deformation have been made, this method updates the director exactly even when the incremental rotation $\Delta\mathbf{t}_A \in T_{\mathbf{t}_A^k} S^2$ is large, this in contrast with standard plate and shell theory. The update procedure follows the following steps: the spatial (deformed configuration) and material (undeformed configuration) director

increments are related by $\Delta\mathbf{t}_A = \mathbf{\Lambda}_A^k \Delta\mathbf{T}_A$, where $\mathbf{E}_3 \mapsto \mathbf{t}_A^k = \mathbf{\Lambda}_A^k \mathbf{E}_3 \in S^2$. It is important to note that $\Delta\mathbf{t}_A \in T_{\mathbf{t}_A^k} S^2$ because, by definition:

$$\mathbf{t}_A^{k+1} \cdot \Delta\mathbf{t}_A = \tilde{\mathbf{\Lambda}}_A^k \mathbf{E}_3 \cdot \tilde{\mathbf{\Lambda}}_A^k \Delta\mathbf{T}_A = \mathbf{E}_3 \cdot \Delta\mathbf{T}_A = 0 \tag{3.107}$$

Because the director is always tracing curves on the unit circle it is trivial to note that its norm is always one, therefore enforcing the *inextensibility* constraint. After updating the nodal director field, the orthogonal transformation $\mathbf{\Lambda}_A^k$ is updated using the relation $\mathbf{\Lambda}_A^{k+1} = \Delta\mathbf{\Lambda}_A^k \mathbf{\Lambda}_A^k$, where $\Delta\mathbf{\Lambda}_A^k \in \mathrm{SO}(3)$ is the unique orthogonal transformation that rotates $\mathbf{t}_A^k \in S^2$ to $\mathbf{t}_A^{k+1} \in S^2$, see Figure 3.15. The update problem, summarized in Algorithm 1, can now be defined.

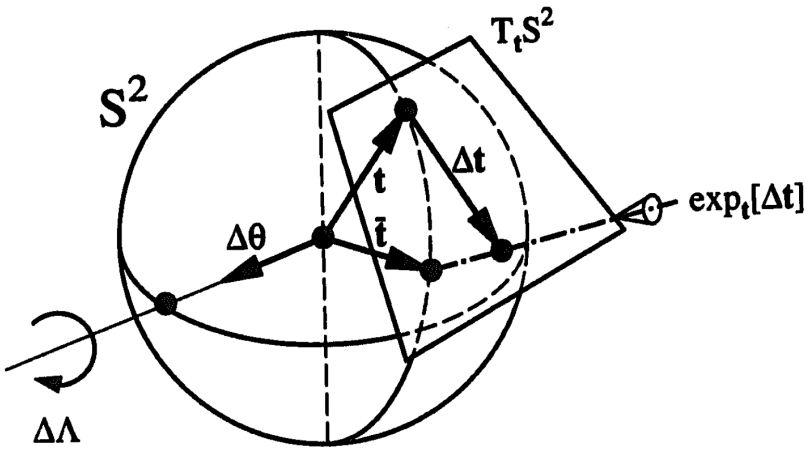

Figure 3.15: The rotation increment $\Delta\mathbf{\Lambda}_A \in \mathrm{SO}(3)$ which is used to rotate $\mathbf{t}_A^k$ to $\mathbf{t}_A^{k+1}$ [41].

Update problem

(i) Given a configuration at the kth iteration, defined by:

$$(\mathbf{x}_A^k, \mathbf{t}_A^k) \in \mathbb{R}^3 \times S^2; \quad \mathbf{\Lambda}_A^k \in \mathrm{SO}(3)$$

(ii) Given (nodal) increments

$$(\Delta\mathbf{u}_A, \Delta\mathbf{T}_A) \in \mathbb{R}^3 \times T_{\mathbf{E}_3} S^2$$

(iii) Obtain $\mathbf{x}_A^{k+1}, \mathbf{t}_A^{k+1}$ in $\mathbb{R}^3 \times S^2$

(iv) Update $\mathbf{\Lambda}_A^k \mapsto \mathbf{\Lambda}_A^{k+1} \in \mathrm{SO}(3)$

Table 3.1: Algorithm 1: Geometrically exact kinematic update procedure [19, 41]

Algorithm 1: Kinematic Update Procedure

1: Update nodal positions by simple addition:

$$\bar{\mathbf{x}}_A^{k+1} = \bar{\mathbf{x}}_A^k + \Delta\mathbf{u}_A \tag{3.108}$$

2: Compute spatial director increment:

$$\Delta\mathbf{t}_A = \tilde{\mathbf{\Lambda}}_A^k \Delta\mathbf{T}_A \tag{3.109}$$

3: Update directors using exponential map:

$$\mathbf{t}_A^{k+1} = \exp_{\mathbf{t}_A^k}(\Delta\mathbf{t}_A) := \cos\|\Delta\mathbf{t}_A\|\,\mathbf{t}_A^k + \frac{\sin\|\Delta\mathbf{t}_A\|}{\|\Delta\mathbf{t}_A\|}\Delta\mathbf{t}_A \tag{3.110}$$

4: Compute orthogonal transformation increment:

$$\Delta\mathbf{\Lambda}_A = \cos\|\Delta\mathbf{t}_A\|\boldsymbol{I} + \frac{\sin\|\Delta\mathbf{t}_A\|}{\|\Delta\mathbf{t}_A\|}\widehat{(\mathbf{t}_A^k \times \Delta\mathbf{t}_A)} + \frac{1-\cos\|\Delta\mathbf{t}_A\|}{\|\Delta\mathbf{t}_A\|^2}(\mathbf{t}_A^k \times \Delta\mathbf{t}_A)\otimes(\mathbf{t}_A^k \times \Delta\mathbf{t}_A) \tag{3.111}$$

5: Update orthogonal transformation:

$$\mathbf{\Lambda}_A^{k+1} = \Delta\mathbf{\Lambda}_A\mathbf{\Lambda}_A^k \tag{3.112}$$

3.9. Through-the-Thickness Stretching

The following set defines the ***extensible*** *one-director Cosserat surface* [73]:

$$\mathscr{C} := \left\{(\boldsymbol{\varphi}, \mathbf{d}) : \mathcal{A} \subset \mathbb{R}^2 \to \mathbb{R}^3 \times \mathbb{R}^3 \,|\, \mathbf{d}\cdot[a_1 \times a_2] > 0\right\} \tag{3.113}$$

Where:

- The map $\boldsymbol{\varphi} : \mathcal{A} \to \mathbb{R}^3$ is used to define the mid-surface position.
- The map $\mathbf{d} : \mathcal{A} \to \mathbb{R}^3$ is used to define an extensible normal vector at any point in the mid-surface.

The shell is once again subjected to prescribed Dirichlet boundary conditions, given by:

$$\boldsymbol{\varphi}(\xi_\alpha, t) = \bar{\boldsymbol{\varphi}}(\xi_\alpha, t) \quad \text{on} \quad \partial_\varphi\mathcal{A}\times[0,T] \tag{3.114a}$$

$$\mathbf{d}(\xi_\alpha, t) = \bar{\mathbf{d}}(\xi_\alpha, t) \quad \text{on} \quad \partial_\mathbf{d}\mathcal{A}\times[0,T] \tag{3.114b}$$

Any configuration of the extensible shell is described as:

$$\mathcal{B} := \left\{\mathbf{x}\in\mathbb{R}^3 \,|\, \mathbf{x} = \mathbf{\Phi}(\xi_1,\xi_2,\xi_3) \;\text{ for }\; (\xi_1,\xi_2,\xi_3)\in\mathscr{C}\right\} \tag{3.115}$$

Just as in the inextensible case, an exact description for the reference configuration exists:

$$\mathcal{B}^0 := \left\{\mathbf{X}\in\mathbb{R}^3 \,|\, \mathbf{X} = \mathbf{\Phi}^0(\xi_1,\xi_2,\xi_3) \;\text{ for }\; (\xi_1,\xi_2,\xi_3)\in\mathscr{C}\right\} \tag{3.116}$$

Any material point in $\mathcal{B}$ is located using the director field $\mathbf{d} : \mathcal{A} \to \mathbb{R}^3$, where now the assumption of unit length is relaxed. This means that the director can take any value in $\mathbb{R}^3$. Points $\mathbf{x}$ in $\mathcal{B}$ are thus described by the mapping:

$$\mathbf{x} = \mathbf{\Phi}(\xi_1,\xi_2,\xi_3) := \boldsymbol{\varphi}(\xi_1,\xi_2) + \xi_3\mathbf{d}(\xi_1,\xi_2) \tag{3.117}$$

Points $\mathbf{X}$ in the undeformed configuration $\mathcal{B}^0$ are described by:

$$\mathbf{X} = \mathbf{\Phi}^0(\xi_1, \xi_2, \xi_3) := \boldsymbol{\varphi}^0(\xi_1, \xi_2) + \xi_3 \mathbf{d}^0(\xi_1, \xi_2) \tag{3.118}$$

$$\lambda(\xi_1, \xi_2) := \|\mathbf{d}(\xi_1, \xi_2)\| > 0 \text{ for } (\xi_1, \xi_2) \in \mathcal{A} \tag{3.119}$$

The removal of the inextensibility assumption on the director field means that the director variations are no longer confined to be tangent to the unit sphere. When the director field $\mathbf{d}$ is inextensible, the magnitude of the director vector remains constant. Mathematically, this can be expressed as $\|\mathbf{d}\| = 1$. This constraint ensures that any variation in the director field, denoted as $\delta\mathbf{d}$, must be tangent to the unit sphere. In other words, $\delta\mathbf{d} \cdot \mathbf{d} = 0$, meaning the variation is orthogonal to the director itself. Now the director vector is no longer restricted to have a constant magnitude (i.e., $\|\mathbf{d}\| \neq 1$). This implies that the variations in the director field are not necessarily tangent to the unit sphere. Consequently, the variation $\delta\mathbf{d}$ is no longer orthogonal to the director field $\mathbf{d}$.

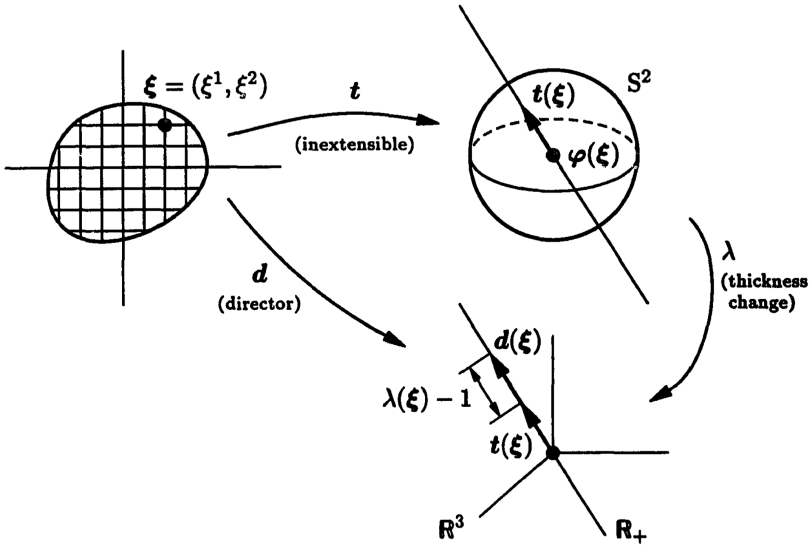

Figure 3.16: Multiplicative decomposition of the director field $\mathbf{d}$ into stretching λ and inextensible part $\mathbf{t}$ [73].

A multiplicative decomposition of the director is employed to treat bending deformations separately from thickness stretching, as shown in Figure 3.16. Thus making it an addition to the inextensible director part. Mathematically, this can be expressed as:

$$\mathbf{d}(\xi_1, \xi_2) = \lambda(\xi_1, \xi_2)\, \mathbf{t}(\xi_1, \xi_2) \text{ , with } \|\mathbf{t}(\xi_1, \xi_2)\| = 1 \text{ and } \lambda(\xi_1, \xi_2) > 0 \tag{3.120}$$

As before, a set is defined to state the new kinematic assumptions:

$$\mathscr{C} := \left\{ \mathbf{\Phi} = (\boldsymbol{\varphi}, \mathbf{t}, \lambda) : \mathcal{A} \subset \mathbb{R}^2 \rightarrow \mathbb{R}^3 \times S^2 \times \mathbb{R}_+ | \, \mathbf{t} \cdot [a_1 \times a_2] > 0 \right\} \tag{3.121}$$

The decomposed stress resultants are now given by:

$$\mathbf{n}^\alpha = \widetilde{n}_{\alpha\beta} \partial_\beta \boldsymbol{\varphi} + \widetilde{m}_{\alpha\beta} \partial_\beta \mathbf{d} + \widetilde{q}_\alpha \mathbf{d} \tag{3.122a}$$

$$\tilde{\mathbf{m}}^\alpha = \widetilde{m}_{\alpha\beta} \partial_\alpha \boldsymbol{\varphi} + \widetilde{m}^{3\alpha} \mathbf{d} \tag{3.122b}$$

$$\mathbf{l} = \widetilde{q}_\alpha \partial_\alpha \boldsymbol{\varphi} + \widetilde{m}^{3\alpha} \partial_\alpha \mathbf{d} + \widetilde{l}^3 \mathbf{d} \tag{3.122c}$$

When thickness stretch is included, the stress resultants no longer contain indeterminate components. Compare Equation 3.122, which presents the new equations that account for thickness stretch, with Equation 3.38, which presents the previous equations without thickness stretch. Differentiating Equation 3.120 with respect to the parametric coordinates, the following is obtained:

$$\partial_\alpha \mathbf{d}(\xi_1,\xi_2) = \partial_\alpha \boldsymbol{\lambda}(\xi_1,\xi_2)\,\mathbf{t}(\xi_1,\xi_2) + \boldsymbol{\lambda}(\xi_1,\xi_2)\,\partial_\alpha \mathbf{t}(\xi_1,\xi_2) = \boldsymbol{\lambda}\left[\mu_\alpha \mathbf{t} + \partial_\alpha \mathbf{t}\right] \tag{3.123}$$

And for the variation:

$$\delta\mathbf{d}(\xi_1,\xi_2) = \delta\boldsymbol{\lambda}(\xi_1,\xi_2)\,\mathbf{t}(\xi_1,\xi_2) + \boldsymbol{\lambda}(\xi_1,\xi_2)\,\delta\mathbf{t}(\xi_1,\xi_2) = \boldsymbol{\lambda}\left[\delta\mu\mathbf{t} + \delta\mathbf{t}\right] \tag{3.124}$$

Introducing the logarithmic stretch $\boldsymbol{\mu}$, its variation $\delta\boldsymbol{\mu}$ and the stretch gradient $\boldsymbol{\mu}_\alpha$:

$$\boldsymbol{\mu} = \ln\boldsymbol{\lambda} \tag{3.125a}$$
$$\delta\boldsymbol{\mu} = \delta\boldsymbol{\lambda}/\boldsymbol{\lambda} \tag{3.125b}$$
$$\boldsymbol{\mu}_\alpha = \partial_\alpha\boldsymbol{\lambda}/\boldsymbol{\lambda} = \partial_\alpha\boldsymbol{\mu} \tag{3.125c}$$

Using these variables the strains can be written as:

$$\epsilon_{\alpha\beta} = \frac{1}{2}\left(a_{\alpha\beta} - a^0_{\alpha\beta}\right) \tag{3.126a}$$
$$\zeta_\alpha = \gamma_\alpha - \gamma^0_\alpha \tag{3.126b}$$
$$\rho_{\alpha\beta} = \kappa_{\alpha\beta} - \kappa^0_{\alpha\beta} \tag{3.126c}$$
$$\chi_\alpha = \partial_\alpha \ln\boldsymbol{\lambda} - \partial_\alpha \ln\boldsymbol{\lambda}^0 = \partial_\alpha \ln\left(\boldsymbol{\lambda}/\boldsymbol{\lambda}^0\right) \tag{3.126d}$$
$$\chi = \ln\boldsymbol{\lambda} - \ln\boldsymbol{\lambda}^0 = \ln\left(\boldsymbol{\lambda}/\boldsymbol{\lambda}^0\right) \tag{3.126e}$$

Where the membrane strain $\epsilon_{\alpha\beta}$, the bending strain $\rho_{\alpha\beta}$ and the transverse shear strain ζ_α are defined as before. χ_α is the newly introduced thickness stretch gradient and χ defines the thickness stretch. The space of admissible variations now becomes:

$$\mathbb{V} = \left\{\delta\mathcal{V} := (\delta\boldsymbol{\varphi}, \delta\mathbf{t}, \delta\boldsymbol{\lambda}) \in \mathcal{A} \to \mathbb{R}^3 \times T_{\mathbf{t}}S^2 \times \mathbb{R} : \delta\boldsymbol{\varphi}|_{\partial_\varphi\mathcal{A}} = 0 \text{ and } \delta\mathbf{t}|_{\partial_{\mathbf{t}}\mathcal{A}} = 0 \text{ and } \delta\boldsymbol{\lambda}|_{\partial_\lambda\mathcal{A}} = 0\right\} \tag{3.127}$$

and the internal power becomes:

$$\mathcal{W}_{\text{int}}(\delta\mathcal{V}) := \int_{\mathcal{S}} \left(\widetilde{n}_{\alpha\beta}\delta\epsilon_{\alpha\beta} + \widetilde{m}_{\alpha\beta}\delta\rho_{\alpha\beta} + \widetilde{q}_\alpha\delta\zeta_\alpha + \widetilde{m}^{3\alpha}\delta\chi_\alpha + \widetilde{l}^3\delta\chi\right) d\mathcal{S} \tag{3.128}$$

The strains in Equation 3.21 remain the same along with the following additions:

$$\chi = \begin{bmatrix} \mu_1 - \mu^0_1 \\ \mu_2 - \mu^0_2 \\ \mu - \mu^0 \end{bmatrix} \tag{3.129}$$

The logarithmic thickness stretch $\boldsymbol{\mu}$ associated with $\delta\chi$, and expanding power through $\widetilde{l}^3$ is interpolated using nodal values as:

$$\boldsymbol{\mu}(\xi_1,\xi_2) = \sum_{A=1}^{N_T} N_A(\xi_1,\xi_2)\boldsymbol{\mu}_A = \sum_{A=1}^{n_T} N_A(\xi_1,\xi_2)\boldsymbol{\mu}_A \tag{3.130}$$

Where its variations are interpolated as before:

$$\delta\boldsymbol{\mu}(\xi_1,\xi_2) = \sum_{A=1}^{N_T} N_A(\xi_1,\xi_2)\delta\boldsymbol{\mu}_A = \sum_{A=1}^{n_T} N_A(\xi_1,\xi_2)\delta\boldsymbol{\mu}_A \tag{3.131}$$

The logarithmic strains $\partial_\alpha\boldsymbol{\mu}$ associated with $\delta\chi_\alpha$, and expending power through $\widetilde{m}^{3\alpha}$ are:

$$\partial_\alpha \boldsymbol{\mu}(\xi_1, \xi_2) = \sum_{A=1}^{N_T} \partial_\alpha N_A(\xi_1, \xi_2) \boldsymbol{\mu}_A = \sum_{A=1}^{n_T} \partial_\alpha N_A(\xi_1, \xi_2) \boldsymbol{\mu}_A \tag{3.132}$$

With variation:

$$\delta\partial_\alpha \boldsymbol{\mu}(\xi_1, \xi_2) = \sum_{A=1}^{N_T} \partial_\alpha N_A(\xi_1, \xi_2) \delta\boldsymbol{\mu}_A = \sum_{A=1}^{n_T} \partial_\alpha N_A(\xi_1, \xi_2) \delta\boldsymbol{\mu}_A \tag{3.133}$$

The updated kinematic formulation now includes an additional step for updating the thickness stretch, which can be expressed as:

Table 3.2: Algorithm 2: Geometrically exact kinematic update procedure including thickness stretch [41, 73]

Algorithm 2: Kinematic Update Procedure Including Thickness Stretching

1: Update nodal positions by simple addition:

$$\bar{\mathbf{x}}_A^{k+1} = \bar{\mathbf{x}}_A^k + \Delta\mathbf{u}_A$$

2: Compute spatial director increment:

$$\Delta\mathbf{t}_A = \tilde{\boldsymbol{\Lambda}}_A^k \Delta\mathbf{T}_A$$

3: Update directors using exponential map:

$$\mathbf{t}_A^{k+1} = \exp_{\mathbf{t}_A^k}(\Delta\mathbf{t}_A) := \cos\|\Delta\mathbf{t}_A\|\,\mathbf{t}_A^k + \frac{\sin\|\Delta\mathbf{t}_A\|}{\|\Delta\mathbf{t}_A\|}\Delta\mathbf{t}_A$$

4: Compute orthogonal transformation increment:

$$\Delta\boldsymbol{\Lambda}_A = \cos\|\Delta\mathbf{t}_A\|\boldsymbol{I} + \frac{\sin\|\Delta\mathbf{t}_A\|}{\|\Delta\mathbf{t}_A\|}\widehat{(\mathbf{t}_A^k \times \Delta\mathbf{t}_A)} + \frac{1-\cos\|\Delta\mathbf{t}_A\|}{\|\Delta\mathbf{t}_A\|^2}(\mathbf{t}_A^k \times \Delta\mathbf{t}_A) \otimes (\mathbf{t}_A^k \times \Delta\mathbf{t}_A)$$

5: Update orthogonal transformation:

$$\boldsymbol{\Lambda}_A^{k+1} = \Delta\boldsymbol{\Lambda}_A \boldsymbol{\Lambda}_A^k$$

6: Update logarithmic stretch:

$$\boldsymbol{\mu}_A^{k+1} = \boldsymbol{\mu}_A^k + \Delta\boldsymbol{\mu}_A \tag{3.134}$$

The final stretch is then obtained by:

$$\boldsymbol{\lambda}_{\text{final}} = \exp[\boldsymbol{\mu}_{\text{final}}] \tag{3.135}$$

Chapter 4

Results and Discussion

This chapter presents the results of numerical simulations conducted to verify and analyze the behavior of multi-layered shells under various loading conditions. The key scenarios examined include free vibration, post-buckling behavior, and torsional effects. The findings confirm that explicitly modeling each layer yields accurate results in most of the verification cases cases. However, an error related to the stability term has been observed.

4.1. Verification

To verify the implemented multi-layered shell model, several problems including the free vibration problem are selected. The free vibration problem involves computing the natural frequencies and mode shapes of the structure without external forces, which can be compared against the well-known analytical solution. The natural frequencies and mode shapes depend on the mass distribution and stiffness of the shell, making them ideal for verifying whether the model accurately represents the physical behavior of the system.

4.1.1. Free Vibration of Clamped Beam

The equation of motion for an undamped free vibration assuming small deflections can be written as [75]:

$$\frac{\partial^4}{\partial x^4}u(x,t) + \beta^4 \frac{\partial^2}{\partial t^2}u(x,t) = 0 \tag{4.1}$$

This equation of motion has the general solution:

$$u(x,t) = \sum_{n=1}^{\infty} u_n(x)\left(A_n \sin \omega_n t + B_n \cos \omega_n t\right) \tag{4.2}$$

Where $u_n(x)$ are the mode shapes:

$$u_n(x) = \left[\cosh(\beta_n x) - \cos(\beta_n x) + \left(\frac{\cos(\beta_n a) + \cosh(\beta_n a)}{\sin(\beta_n a) + \sinh(\beta_n a)}\right)\left(\sin(\beta_n x) - \sinh(\beta_n x)\right)\right] \tag{4.3}$$

The eigenvalues of the system β_n are given by:

$$\beta_n^4 = \frac{\hat{\rho}\omega_n^2}{EI} \tag{4.4}$$

Where:

- E is the Young's modulus of the material,
- I is the second moment of area (or the moment of inertia) of the beam's cross-section $\frac{bh^3}{12}$.
- b is the width of the beam.
- h is the thickness of the beam.
- $\hat{\rho}$ is the linear mass density ρhb

The eigenvalue of the first mode is expressed as $\beta_1 = \frac{1.875104}{a}$, where a is the length of the beam. The associated natural frequency is:

$$\omega_1 = \beta_1^2 \sqrt{\frac{EI}{\hat{\rho}}} \tag{4.5}$$

The initial conditions are given as:

$$u(x,0) = 0 \tag{4.6a}$$

$$\frac{\partial}{\partial t} u(x,0) = v(x,0) = u_1(x) V_0 \tag{4.6b}$$

Using these initial conditions, the response of the beam is limited to its first mode:

$$u(x,t) = u_1(x) \frac{V_0}{\omega_1} \sin(\omega_1 t) \tag{4.7}$$

The equations of motion were solved over one time period T of the exact solution, where $T = \pi/\omega_1$. Figure 4.1a presents the models used throughout this thesis, featuring one, two, four, and eight layers, each maintaining the same total thickness. The figure illustrates the position of each layer along the z-axis.

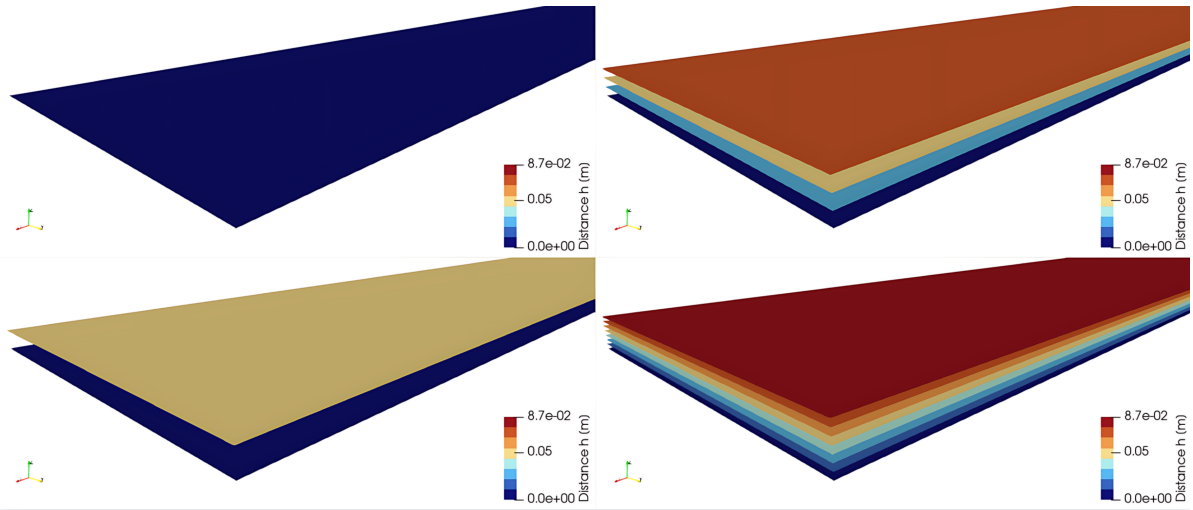

(a) The models used throughout the remainder of this thesis consist of one, two, four, and eight layers, all maintaining the same total thickness.

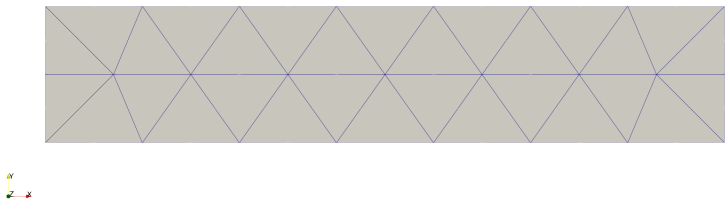

(b) Mesh used in the free vibration problem.

Figure 4.1: Free vibration verification problem.

First, a convergence study on the penalty parameters c_x and c_T has been performed, as shown in Figure 4.2. Values in the range of 1 to 10 yield good results, with a slight shift to the left. It has been decided to use the value 5 for both parameters in all models.

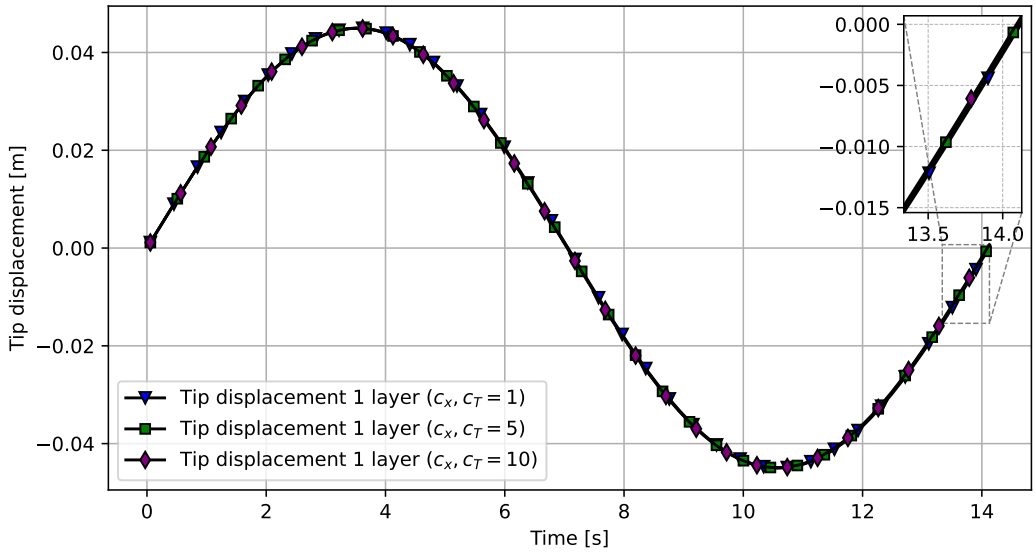

Figure 4.2: Convergence study evaluating the effect of c_x and c_T. Increasing these parameters shifts the curve slightly to the left, indicating a marginal but observable impact on the system's response.

The parameters used in this problem can be seen in Table 4.1.

Table 4.1: Simulation parameters for the free vibration of a cantilever beam.

Parameter	Value
E	12×10^6 Pa
ν	0
ρ	1000 kg/m^3
a	5 m
b	1 m
h	0.1 m
V_0	0.01 m/s
c_x	5
c_T	5

Figure 4.3 investigates the effect of the inertia correction. First, the results for one layer with thicknesses of 0.1 and 0.05 have been plotted. As expected, the response of the single layer with half the thickness exhibits a lower frequency and double the amplitude compared to the layer with double the thickness, indicating it is less stiff. Two layers with a combined thickness of 0.1, without correcting the inertia, match the result of the more flexible single layer rather than the response of the thicker single layer. The code essentially treats both layers as a single layer with half the thickness. When the inertia of both layers is corrected, the response now perfectly matches that of the thicker single layer.

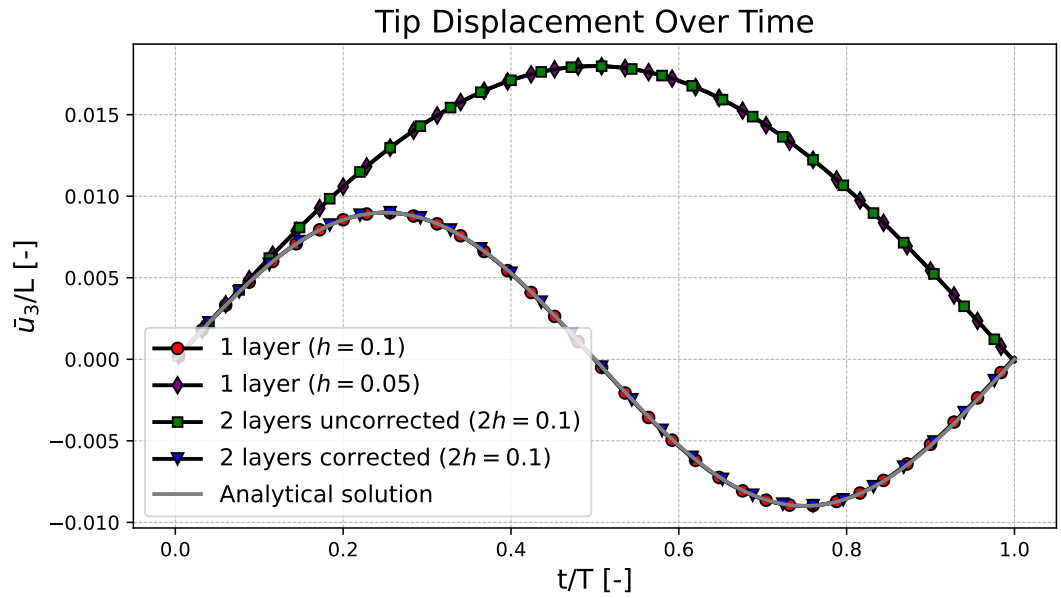

Figure 4.3: Comparison of results between a single layer with thickness $h = 0.1$ and $h = 0.05$, and two coupled layers with uncorrected and corrected rotational inertia of the bulk elements. The results of the two coupled layers now align closely with those of the single layer with thickness $h = 0.1$. The uncorrected results correspond to that of a single layer with thickness $h = 0.05$.

Finally, Figure 4.4 compares the results of all models shown in Figure 4.1a, an excellent match between all these models is observed in this case. Note that the same initial condition has been applied to all layers.

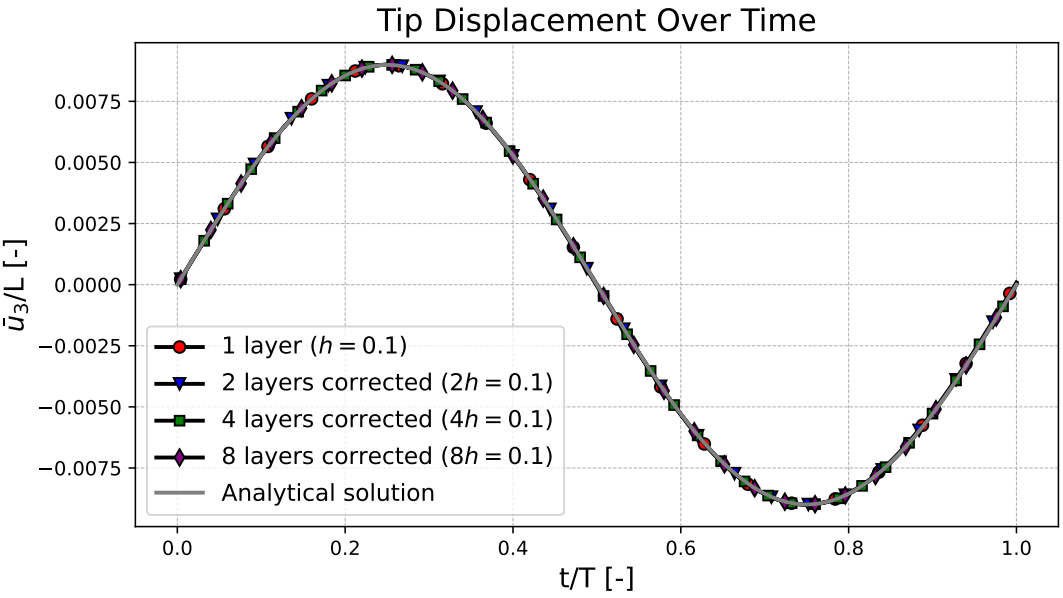

Figure 4.4: Comparison of the same problem using multiple layers with the same combined thickness, the results is exactly the same in all models.

4.1.2. Post-buckling of Clamped beam

This section models the post-buckling behavior of a beam using the Euler buckling load. The model is shown in Figure 4.5a, and the mesh used is illustrated in Figure 4.5b. It is clamped on one edge and the buckling load F is applied on the other, since this is a numerical model, an out-of-plane perturbation P has to be applied in order for buckling to occur, the magnitude of this perturbation is very small compared to the buckling load.

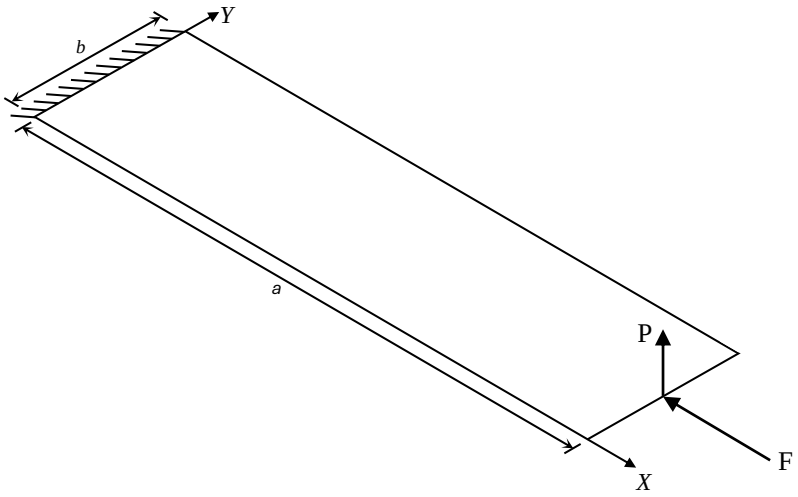

(a) Boundary conditions and applied forces of the beam post-buckling where a small out-of-plane load must be added to ensure that the shell will buckle at the buckling load F_{cr}.

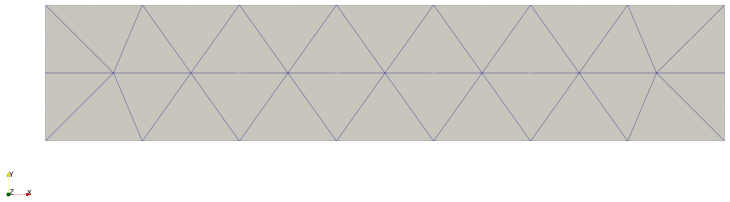

(b) Mesh used in the post-buckling problem.

Figure 4.5: Beam post-buckling problem.

Euler's theory predicts that a shell clamped at one end and free at the other, buckles at the the critical buckling load F_{cr}, which is given by:

$$F_{cr} = \frac{\pi^2 EI}{4a^2} \tag{4.8}$$

Where:

- E is the Young's modulus of the material,
- I is the second moment of area (or the moment of inertia) of the beam's cross-section,
- a is the length of the beam or shell.

The parameters used in this case are shown in Table 4.2.

Table 4.2: Simulation parameters for the beam post-buckling problem [2, 76].

Parameter	Value
E	75×10^9 Pa
ν	0.316
ρ	2700 kg/m^3
a	0.3 m
b	0.06 m
h	6×10^{-3} m
P	1.25 N
F	$2.75F_{\text{cr}}$ N
c_x	5
c_T	5

Figure 4.6 illustrates several configurations of the beam during the simulation. The total applied load remains the same in all four models, with the force evenly divided among the layers.

Figure 4.6: Several configurations of the post-buckled beam with eight layers.

Figure 4.7 shows the non-dimensional force $\left(\frac{F}{F_{\text{cr}}}\right)$ against the non-dimensional tip displacement $\left(\frac{u_3}{a}\right)$ for all four models. As before, a strong match can be observed. The results have been compared to existing literature, and a good agreement is noted.

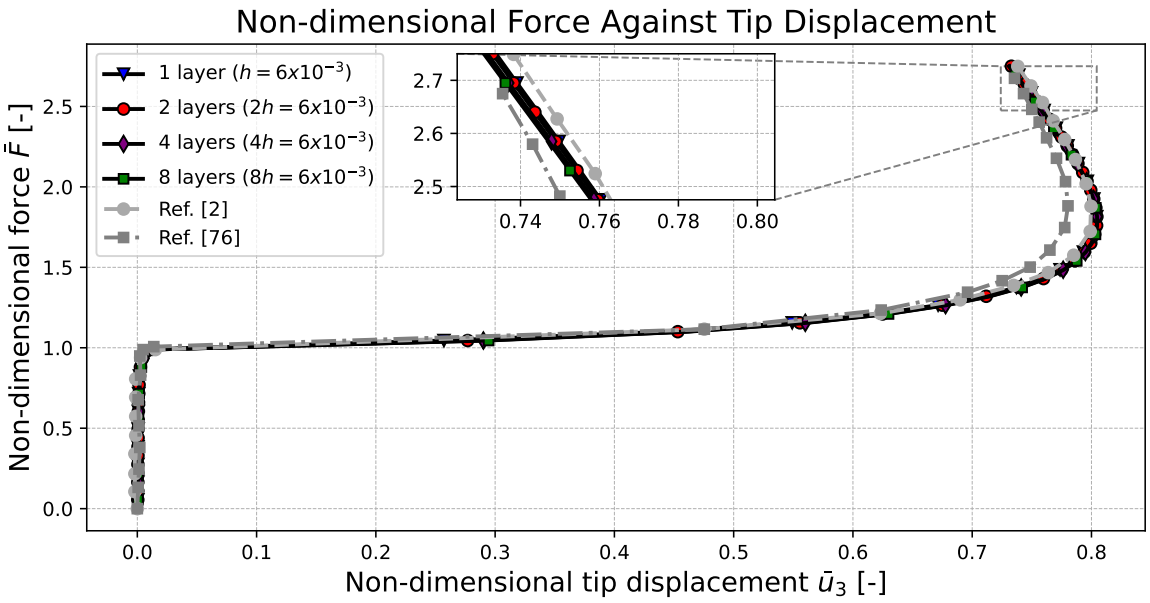

Figure 4.7: Comparison of the same post-buckling problem using multiple layers with the same combined thickness, The obtained graphs have a great match with literature [2, 76].

4.1.3. Twisting of Clamped Beam

The twisting of an initially clamped beam with length a, width b, and thickness h, is analyzed under an applied torque T at its tip (see Figure 4.8a). The mesh used for this analysis is shown in Figure 4.8b, and the problem parameters are listed in Table 4.3. This example represents a thick shell, with a thickness-to-width ratio of $h/b = 0.2$. Since this model is subjected to an applied torque, the torque is distributed among the layers based on their contribution to the inertia. The outer layers experience a higher torque compared to the inner layers, the combined torque on all layers is constant.

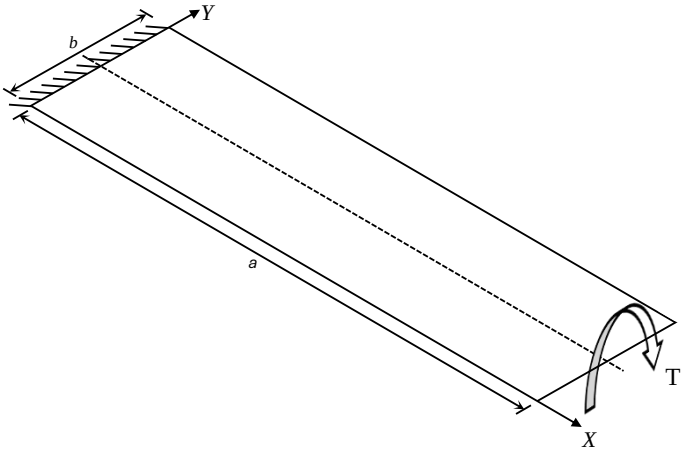

(a) Boundary conditions and applied moment of the beam twist problem.

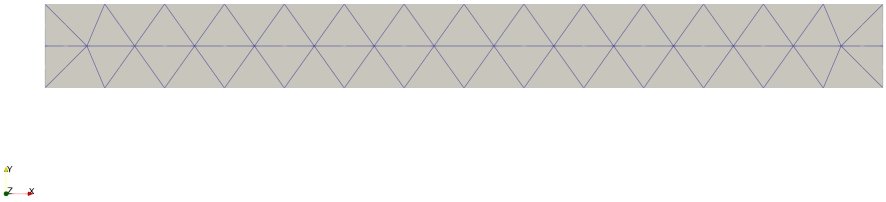

(b) Mesh used in the beam twist problem

Figure 4.8: Twisting of beam.

Table 4.3: Simulation parameters for the beam twist problem.

Parameter	Value
E	12×10^6 Pa
ν	0
ρ	$1.0\,\mathrm{kg/m^3}$
a	10 m
b	1 m
h	0.2 m
T	20×10^3 Nm
c_x	5
c_T	5

The final state of twist for all four models is shown in Figure 4.9. It is evident that the four-layer and eight-layer models rotate slightly further than the single-layer model. This is likely due to an issue with the stability term allowing the layers to pass through each other.

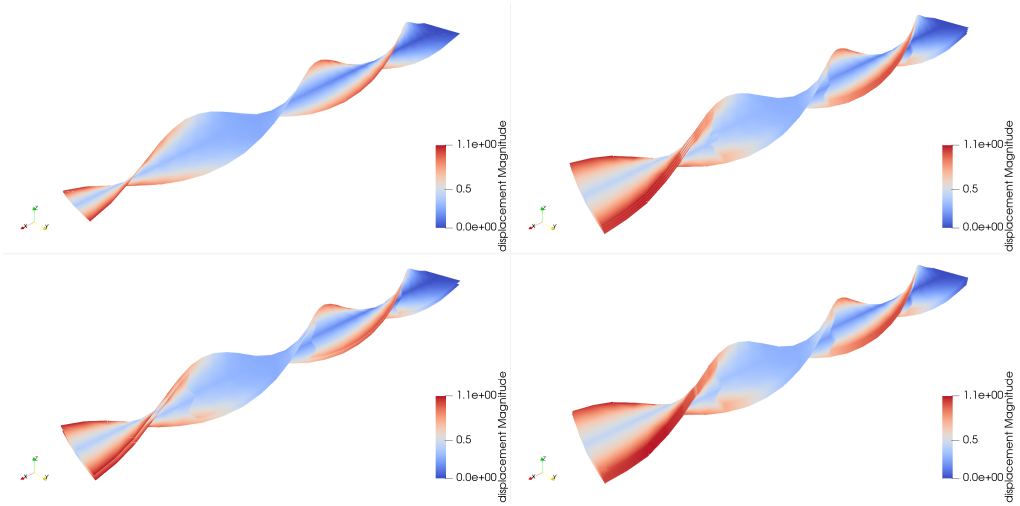

Figure 4.9: For the final state of twist in the one, two, four, and eight-layer models, it was observed that the layers move through each other instead of maintaining the appropriate thickness offset. Additionally, the final state of the two-layer model slightly deviates from that of the single-layer model. Both the four-layer and eight-layer models stopped converging at approximately the same time.

A close-up of this issue is shown in Figure 4.10. In the current implementation, the mid-surface displacements are constrained by enforcing zero relative displacement. However, the displacements at the interfaces should be coupled while accounting for the layer thicknesses. It is expected that modifying the stabilization term to reflect this will resolve the issue. Currently the stabilization parameter preserves the correct distance between mid-surface nodes, however this is not along the direction aligned with the director. Due of this and the applied moments, each shell essentially rotate in place, preventing the bottom layer from transitioning to the uppermost position after a full twist (see Figure 4.11). This preserves the original orientation of the layers, which is unintended. This results in displacements progressively becoming worse as the simulation progresses since initial discrepancies compound in larger errors.

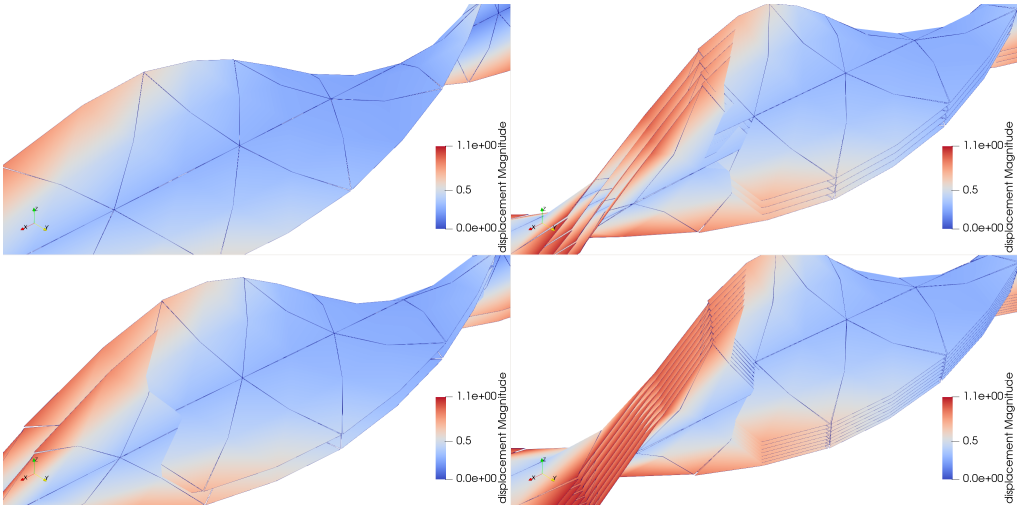

Figure 4.10: A close-up view of the layers shows them interpenetrating, with the same issue occurring in the middle and near the clamp, causing the orientation of the layers to remain unchanged near the tip. This behavior indicates an error with the stabilization terms.

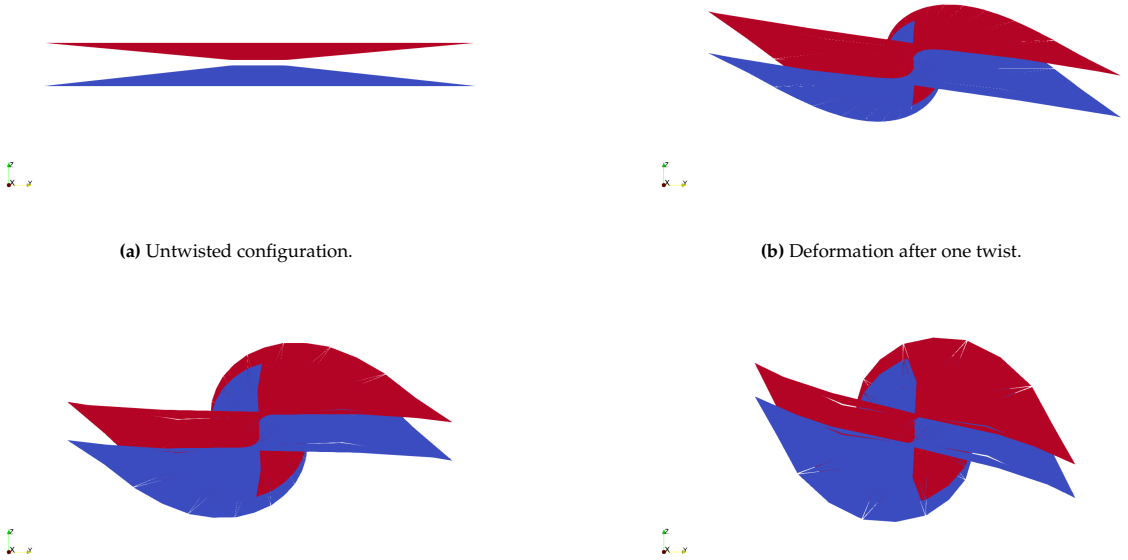

(a) Untwisted configuration.

(b) Deformation after one twist.

(c) Deformation after two twists.

(d) Final deformation after three twists.

Figure 4.11: Twisting of two-layer model where blue corresponds to the first layer and red corresponds to the second layer, it can be observed that the blue layer never transitions to the top position and always rotates in place. Additionally, the interpenetration of layers can clearly be seen.

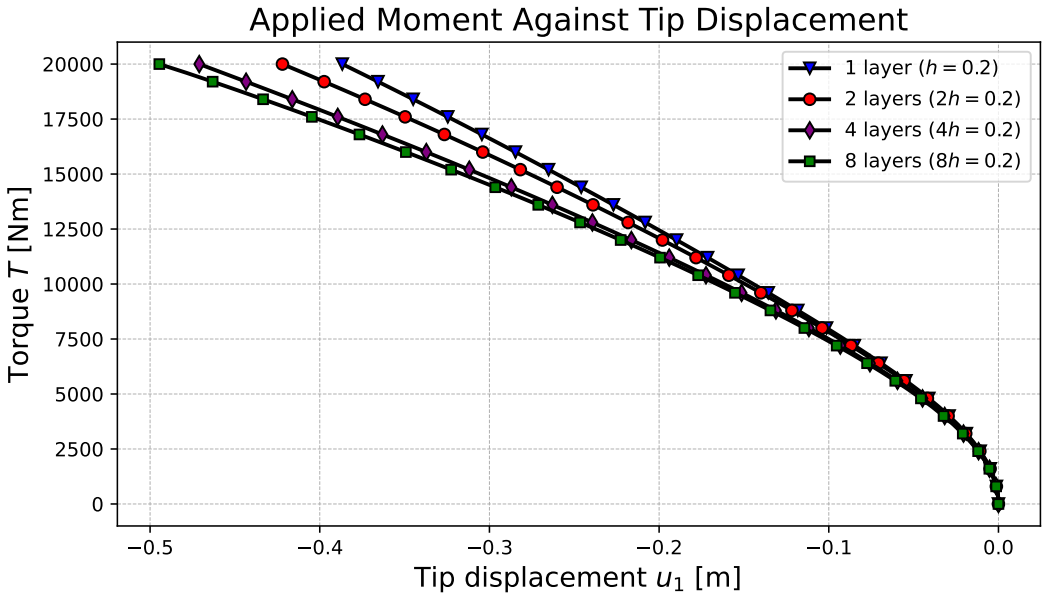

(a) Torque against displacement u_1.

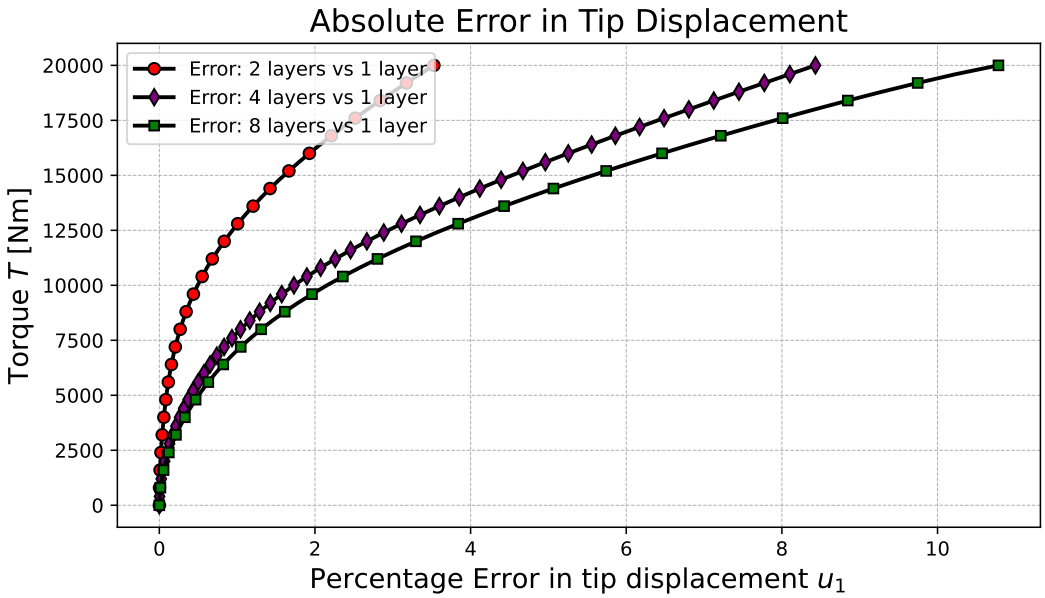

(b) The absolute error in displacement u_1 increases throughout the simulation, reaching a maximum of 3.5% for the two-layer model. The four-layer and eight-layer models exhibit much larger errors, indicating that the issue with the stability term actually impacts the results rather than just affecting visualization.

Figure 4.12: Displacement u_1 under applied torque T and the absolute error compared to a single layer.

Figure 4.12a compares the u_1-displacement of all four models, while the absolute error with respect to the single-layer model is plotted in Figure 4.12b. The match is not as accurate as in the previous cases, with errors reaching up to 3.5%. The four-layer and eight-layer models behave similarly but exhibit significantly larger errors compared to the single-layer model. It is believed that this is due to the stability term not working properly since the layers do not deform as would be expected, the bottom layer remains the bottom layer during the entire simulation.

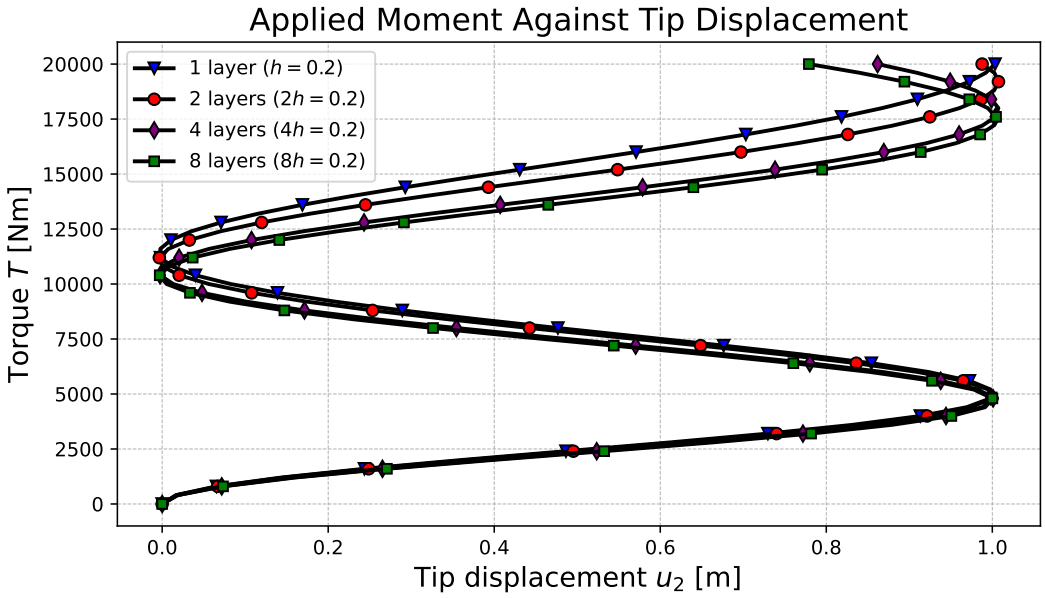

(a) Torque against displacement u_2.

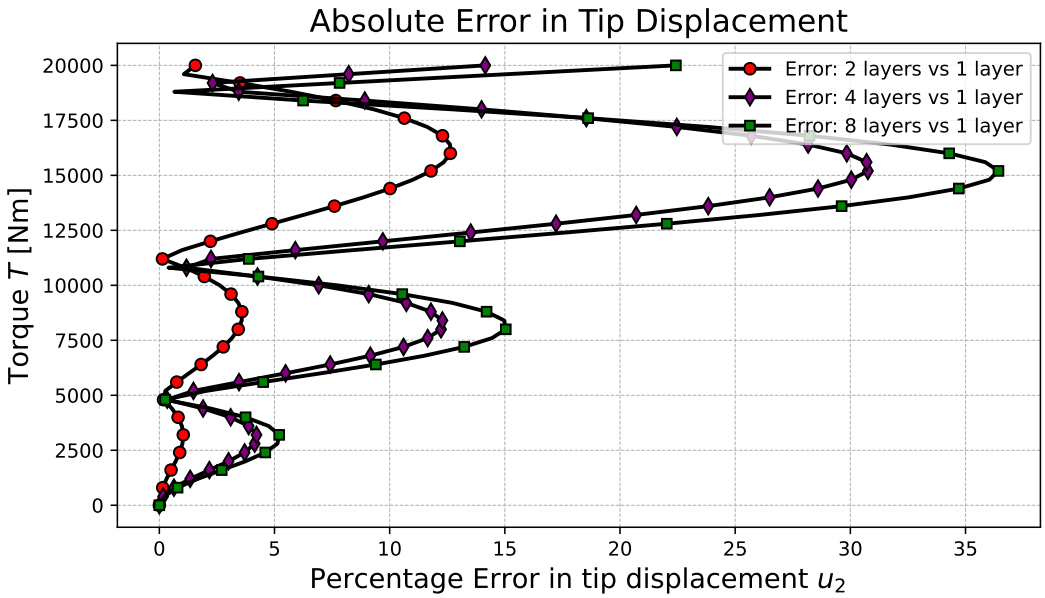

(b) The absolute error in displacement u_2 is much larger compared to that of the u_1 component, which makes sense since the deformation due to the moment is primarily focused in the yz-plane. It is observed that the absolute error is zero at two points for all models, with maximum errors occurring between these two points. These are the points of maximum displacement; naturally, these should match in all models. Additionally, the error increases with each turn, each time the layers fail to switch orientation.

Figure 4.13: Displacement u_2 under applied torque T and the absolute error compared to a single layer.

Figure 4.13a compares the u_2-displacement of all four models. As before, the absolute error with respect to the single-layer model is plotted in Figure 4.13b. The u_2 displacement component matches relatively well in all cases; however, the error increases with each turn. It is clearly visible that the model undergoes three turns. As in previous cases, the four-layer and eight-layer models show similar behavior, but the error in these models increases much faster than in the two-layer model. Interestingly, there exist two points at which the error is close to zero in between the turns, these are the extremes reached during the simulation.

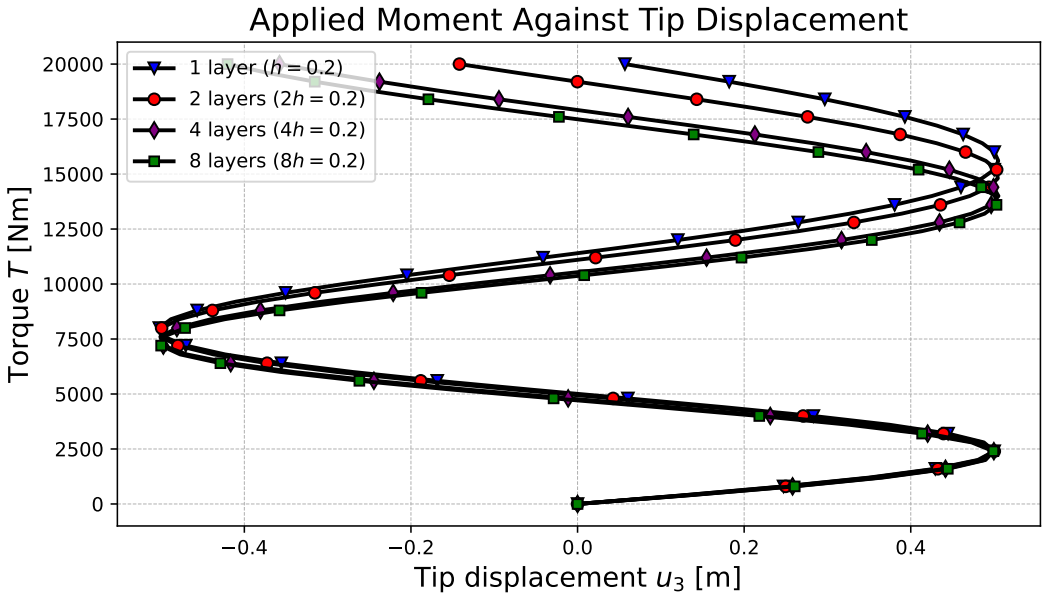

(a) Torque against displacement u_3.

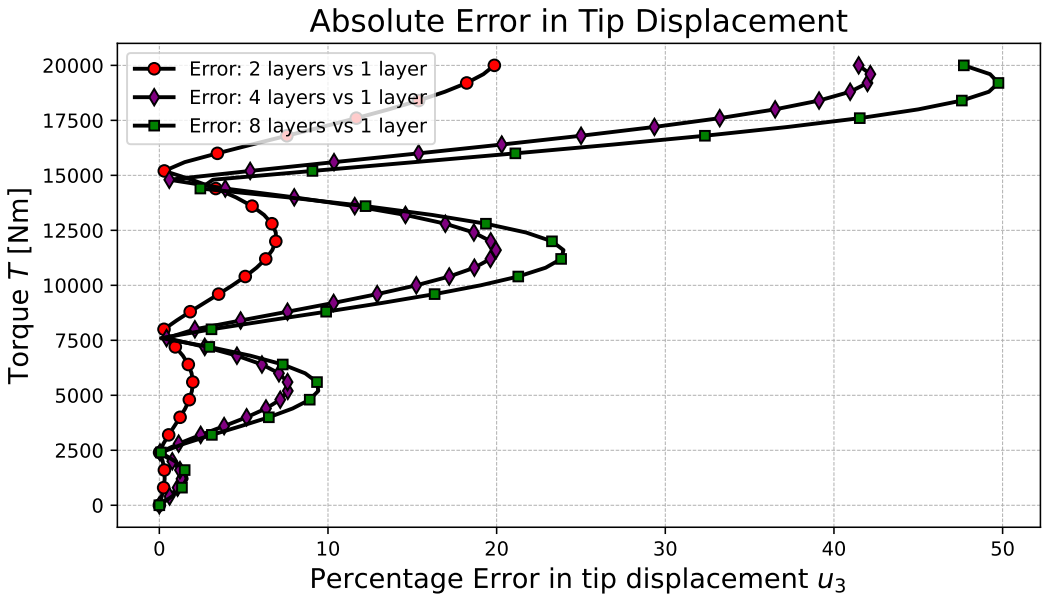

(b) The absolute error in the displacement component u_3 is the largest compared to the previous two components, reaching values of 50%. As for the u_2 displacement, points with errors close to zero exist here as well which are the extremes reached during the deformation.

Figure 4.14: Displacement u_3 under applied torque T and the absolute error compared to a single layer.

Finally, Figure 4.14a compares the u_3-displacement of all four models, with the absolute error relative to the single-layer model plotted in Figure 4.14b. Every observation made about the u_2 displacement curves applies here as well: large errors up to 50% that increase with each turn, while reaching the same maximum displacement.

4.1.4. Roll-up of Clamped Beam

The classic roll-up problem involves an initially flat cantilever beam with length a, width b, and thickness h, subjected to a moment M applied at its tip (see Figure 4.15a). The mesh used for this problem is shown in Figure 4.15b. Based on Euler's theory, the beam should roll up into a complete circle when the moment reaches $M = \frac{2\pi EI}{a}$, where $I = \frac{bh^3}{12}$ is the second moment of the area [41]. The parameters of the problem are indicated in Table 4.4. As in the twisting problem, the moment is distributed according to each layer's contribution to the moment of inertia.

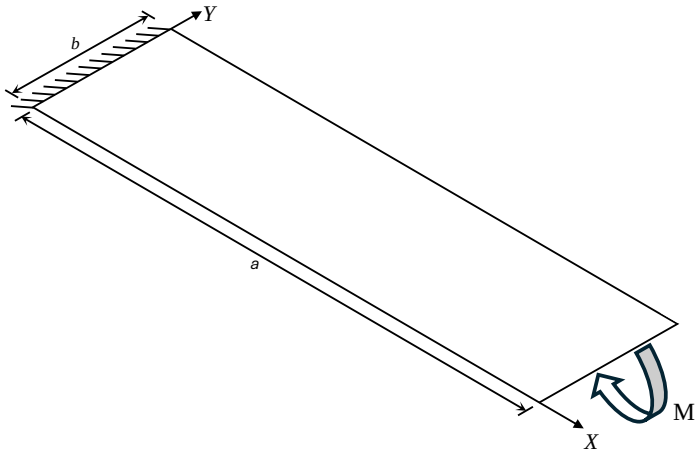

(a) Boundary conditions and applied moment of the beam roll-up problem.

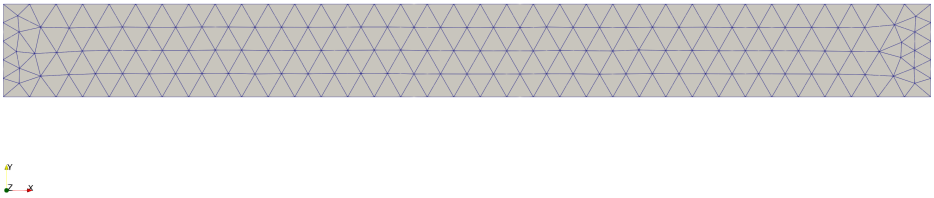

(b) Mesh of the beam

Figure 4.15: Beam roll-up problem.

Table 4.4: Simulation parameters for the beam roll-up problem.

Parameter	Value
E	12×10^6 Pa
ν	0
ρ	$1.0\,\mathrm{kg/m^3}$
a	10 m
b	1 m
h	0.1 m
M	200π Nm
c_x	5
c_T	5

Figure 4.16 shows the final configurations of the same problem modeled with one and eight layers.

(a) Several configurations of the single layer beam during the simulation.

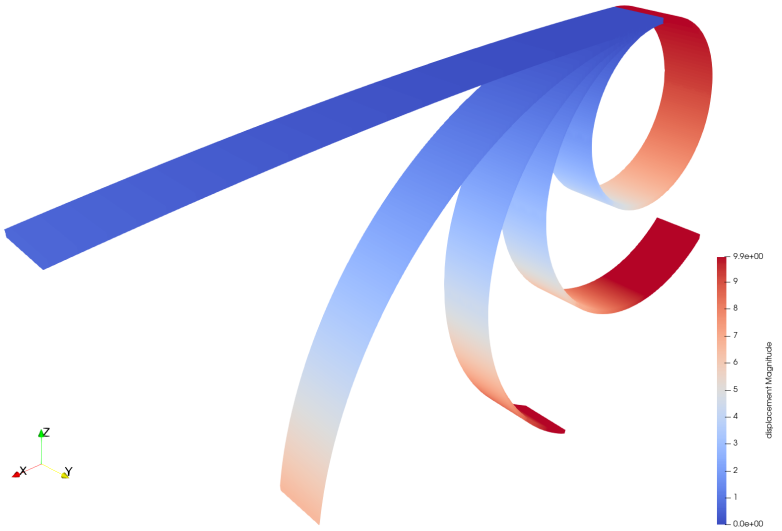

(b) Several configurations of the eight-layer beam during the simulation.

Figure 4.16: Beam roll-up configurations for one and eight layers.

Plotting the displacement components for all four models—shown in Figure 4.18 for the u_1-displacement, Figure 4.19 for the u_2-displacement, and Figure 4.20 for the u_3-displacement—demonstrates an excellent match between the models. Interestingly, the same issue as observed in the twist model, where the layers move through each other, is also present (see Figure 4.17); however, this did not result in big errors. This can be explained by the fact that twisting is a complex deformation involving all three displacement components, and the interpenetration of layers leads to inconsistencies in how they respond to the applied loads, as the layers are no longer in their correct positions. In the roll-up problem, the deformation is simple bending where the orientation/position of the layers does not matter as much. Nevertheless, a discrepancy is observed in the u_2-displacement (see Figure 4.19), although it is insignificant compared to the dimensions and has been included only for completeness.

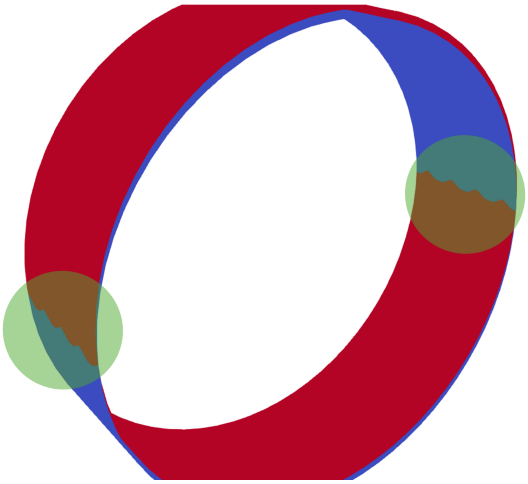

Figure 4.17: As in the beam twist problem, there is an issue where one layer moves through the other, failing to maintain the correct separation and thickness. This occurs again towards the end of the simulation, leading the layers to return to their original positions after effectively swapping places twice, resulting in the correct final configuration.

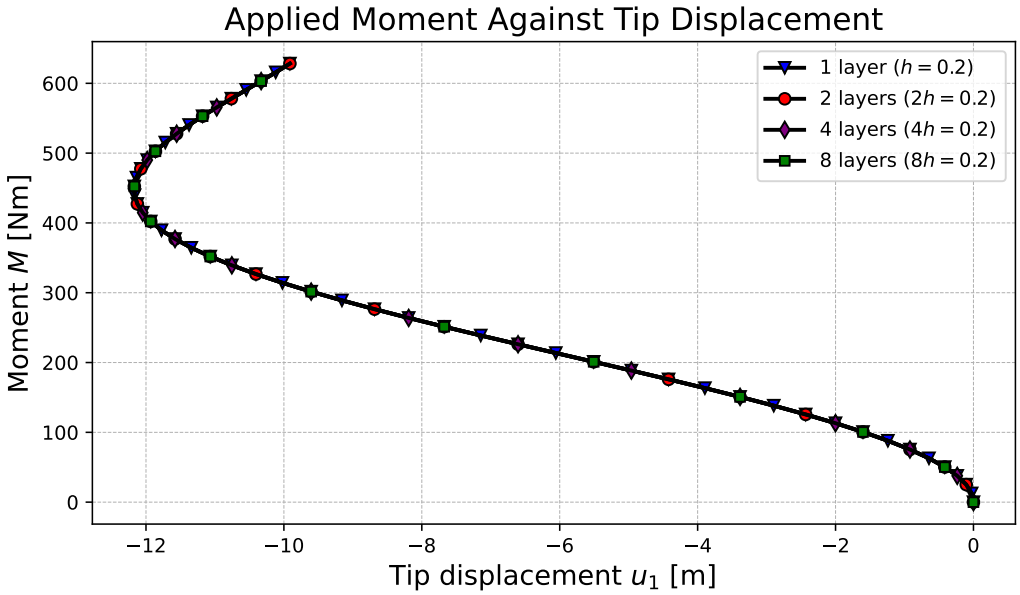

Figure 4.18: The moment M against displacement u_1 shows a strong match for all models. Despite the interpenetration of layers, the models remain equivalent to the single-layer model.

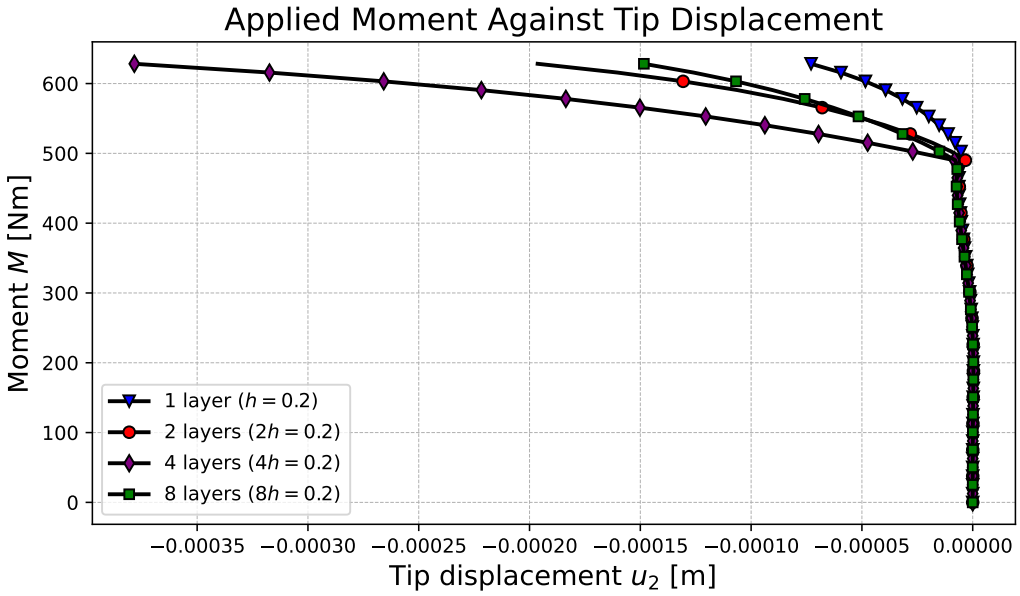

Figure 4.19: The moment M against displacement u_2 also shows a good match in all models. However, near the end of the simulation some discrepancies are observed. Note that the absolute values are negligible compared to the other two displacement components and have only been included for completeness.

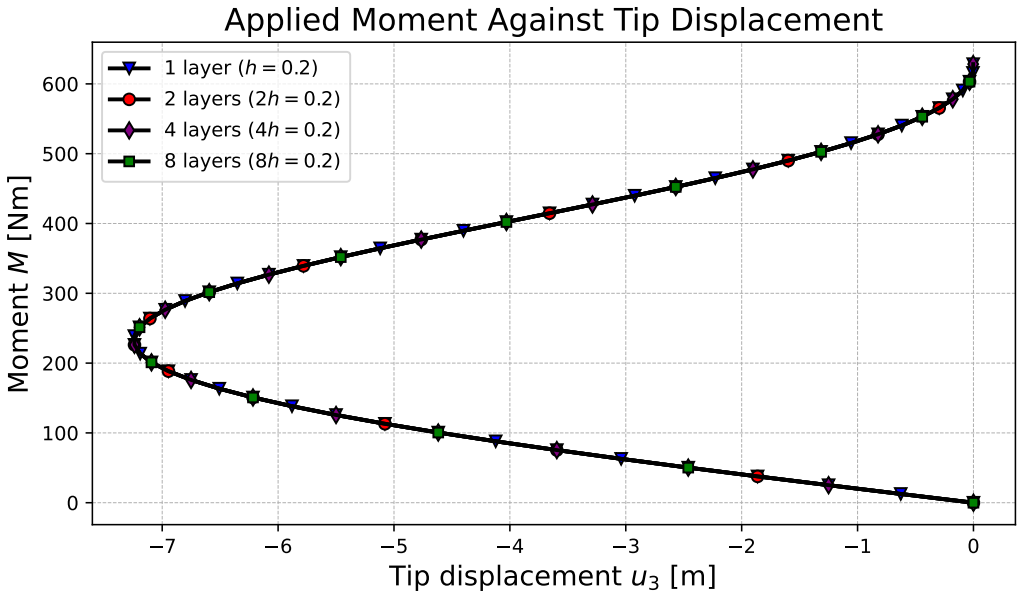

Figure 4.20: The moment M against displacement u_3, similar to the u_1 displacement, shows a good match across all models.

4.2. Computational Experiments

4.2.1. Composite Strip

A straightforward test for evaluating the added composite material is the bend-twist coupling. The test model is illustrated in Figure 4.21a, where the fiber angle is defined as a positive rotation around the z-axis. The mesh used for this analysis is depicted in Figure 4.21b. A point load is applied at the midpoint of the right edge, resulting in unresisted twisting. The parameters of the problem are indicated in Table 4.5.

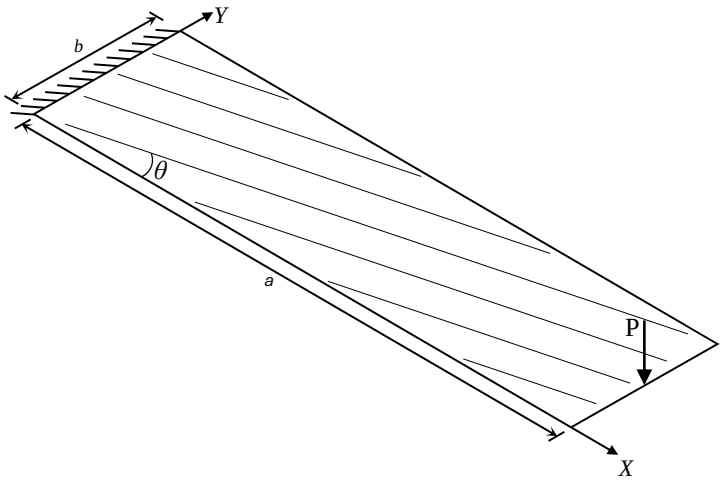

(a) Boundary conditions and applied load of the composite strip problem.

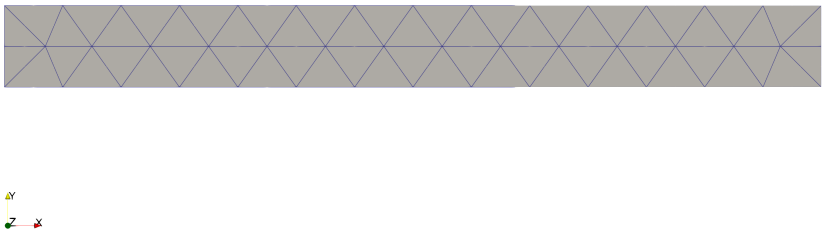

(b) Mesh of the composite strip.

Figure 4.21: Composite strip problem.

Table 4.5: Simulation parameters for the composite strip problem [77].

Parameter	Value
E_1	113×10^9 Pa
E_2	9×10^9 Pa
ν_{12}	0.37
G_{12}	3.82×10^9 Pa
G_{23}	3.446×10^9 Pa
ρ	$1580\,\mathrm{kg/m^3}$
a	0.2 m
b	0.02 m
h	1.5×10^{-4} m
P	0.5 N
c_x	5
c_T	5

Figure 4.22a illustrates the out-of-plane displacement for the laminate $[\theta^\circ/\theta^\circ]_{2S}$ across four cases: $\theta = 0^\circ$, $\theta = 30^\circ$, $\theta = 60^\circ$, and $\theta = 90^\circ$. It can be observed that the $\theta = 30^\circ$ model exhibits the greatest twist, while the $\theta = 60^\circ$ model shows only a slight twist. As expected, the $\theta = 0^\circ$ and $\theta = 90^\circ$ models exhibit no twist. However, the out-of-plane displacement is significantly higher in the $\theta = 90^\circ$ model. Figure 4.22b provides a front view to better visualize the twist.

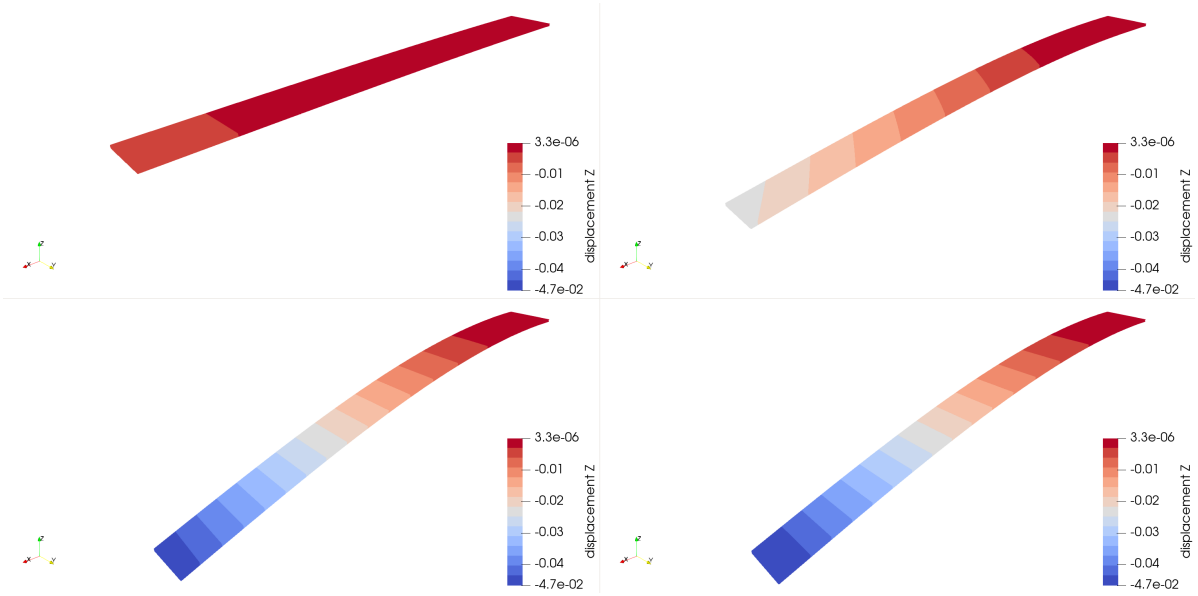

(a) The out-of-plane displacement for the eight-layer laminate $[\theta^\circ/\theta^\circ]_{2S}$ is depicted for fiber orientations $\theta = 0^\circ$ (top left), 30° (top right), 60° (bottom left), and 90° (bottom right). A clear twist is observed in the 30° model, with a slight twist in the 60° model. As expected, the 0° model barely deforms since the fibers provide significant strength in this direction. The 90° model, however, deforms considerably, as its response is entirely influenced by the matrix material.

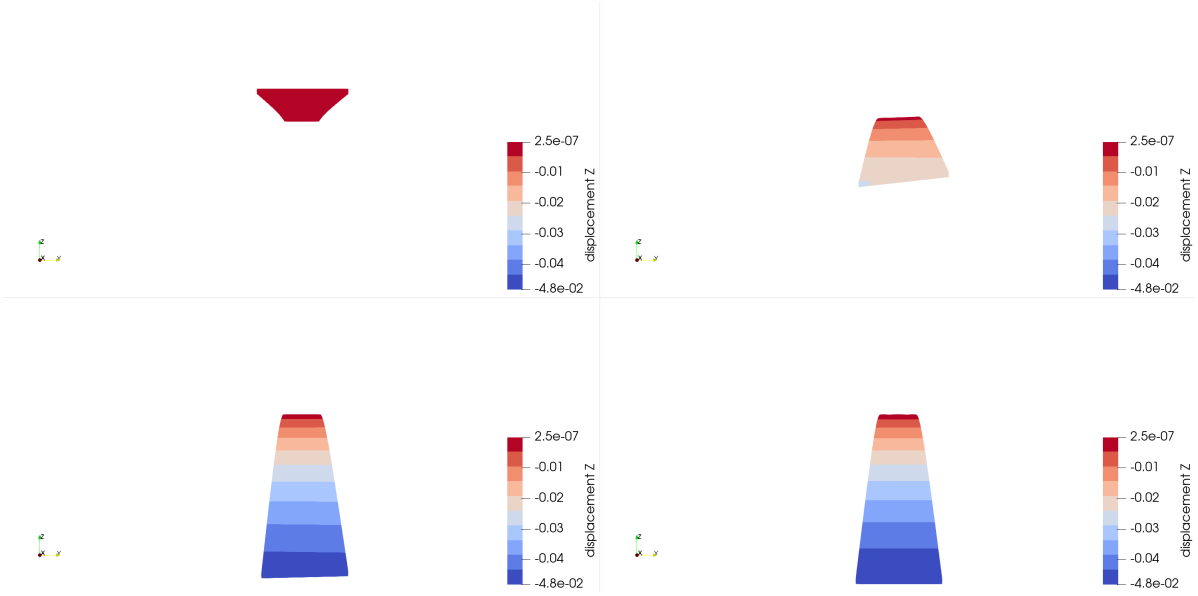

(b) Front-view out-of-plane displacement for the eight-layer laminate $[\theta^\circ/\theta^\circ]_{2S}$ depicted for fiber orientations $\theta = 0^\circ$ (top left), 30° (top right), 60° (bottom left), and 90° (bottom right).

Figure 4.22: The influence of fiber orientation on the out-of-plane displacement is demonstrated for the symmetric eight-layer laminate $[\theta^\circ/\theta^\circ]_{2S}$.

Finally, the layup $[30°/-30°/-30°/30°/-30°/30°/30°/-30°]$, which is symmetric in the upper and lower halves but unsymmetric overall, should not twist when bent. The resulting deformation is shown in Figure 4.23a, with a frontal view provided in Figure 4.23b. It can be observed that the correct behavior of antisymmetric layups is achieved, where opposite orientations and loads produce the same deformation without shear, as the resulting couples cancel each other out.

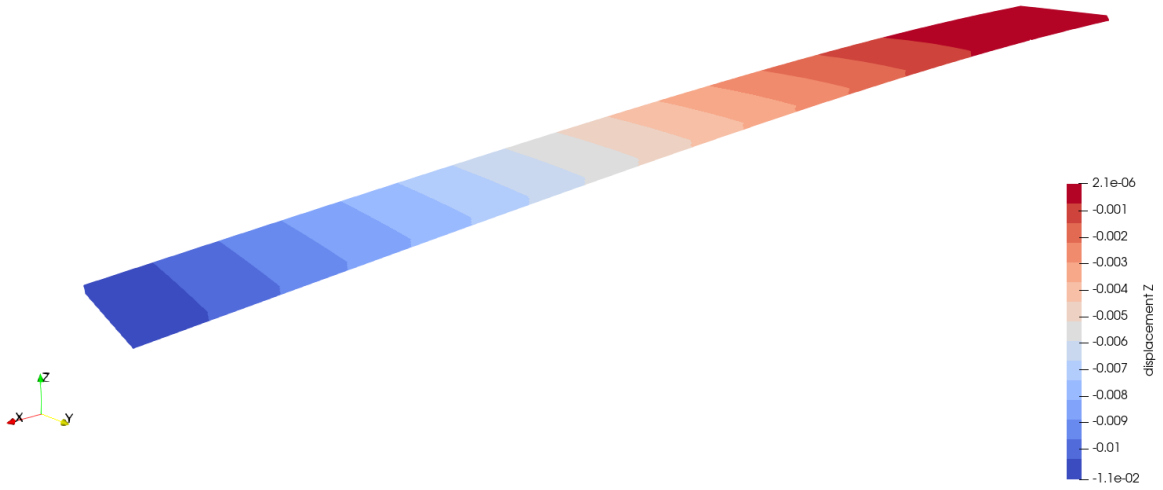

(a) Out-of-plane displacement u_3.

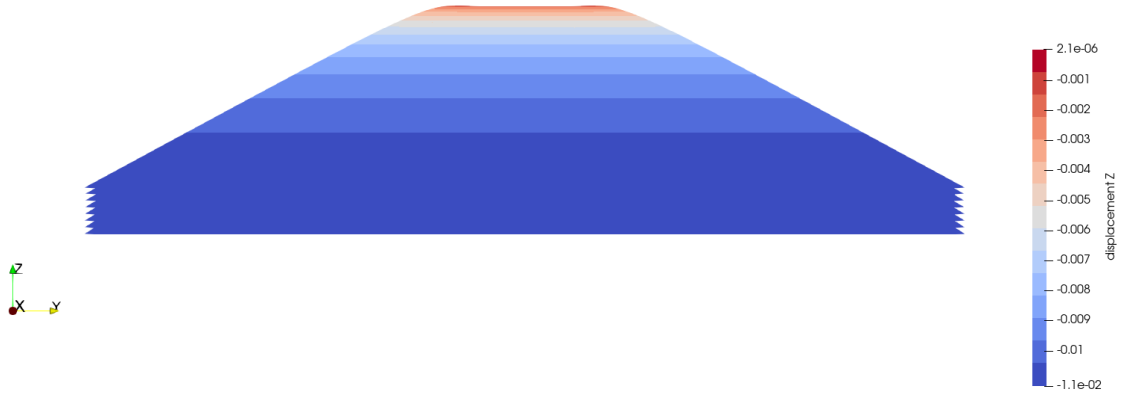

(b) Front view out-of-plane displacement u_3.

Figure 4.23: Displacement for the eight-layer laminate $[30°/-30°/-30°/30°/-30°/30°/30°/-30°]$ shows no twist, which is expected for an antisymmetric layup with symmetric upper and lower halves. Layers with opposite orientations and loads tend to show similar deformations, as the resulting couples negate the total shear due to their equal and opposite nature.

4.2.2. Open Hole Tension

The open hole test model is illustrated in Figure 4.24a, where, as before, the fiber angle is defined as a positive rotation around the z-axis. The mesh used for this analysis is shown in Figure 4.24b, with refinement around the hole to capture the stress concentrations. An axial tension load is applied at one edge, while the opposite edge is clamped. The parameters for this problem are detailed in Table 4.6. Due to time restrictions, the simulation completed approximately 22%, reaching a displacement of 5.5×10^{-5} m.

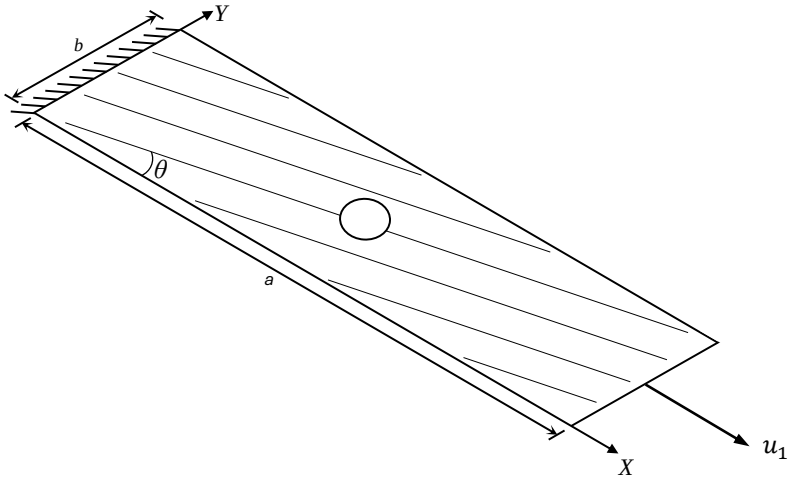

(a) Boundary conditions and applied load of the open hole tension strip.

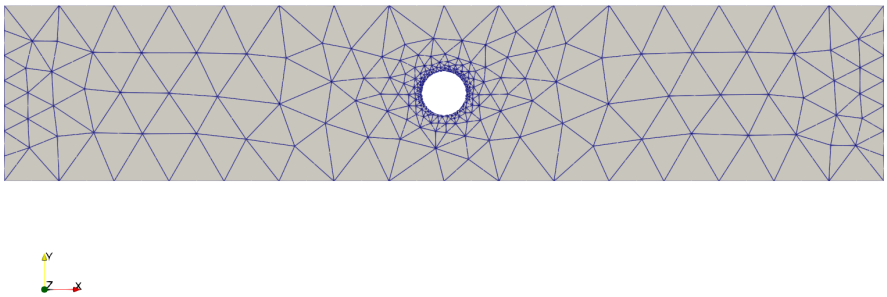

(b) Mesh of the open hole tension strip.

Figure 4.24: Open hole tension problem.

Table 4.6: Simulation parameters for the open hole tension problem [25].

Parameter	Value
E_1	139.835×10^9 Pa
E_2	8.515×10^9 Pa
ν_{12}	0.275
G_{12}	6.3×10^9 Pa
G_{23}	3.2×10^9 Pa
ρ	1580 kg/m^3
a	0.2 m
b	0.04 m
h	1.5×10^{-4} m
u_1	2.5×10^{-4} m
c_x	5
c_T	5

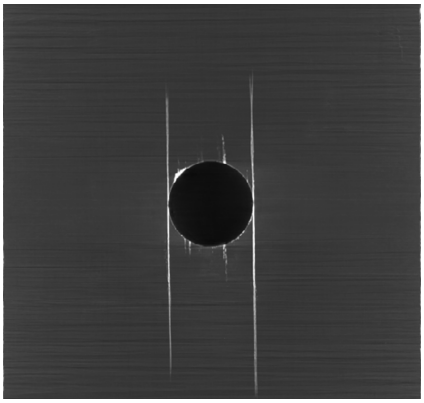

(a) Experimental matrix cracks in the 0° laminae.

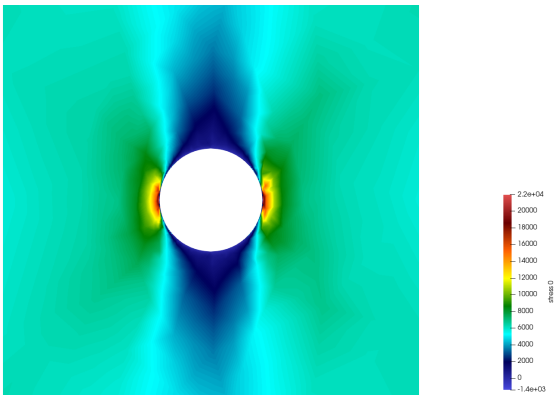

(b) Stress component $\widetilde{n}_{11}$ for the 0° laminae in the model.

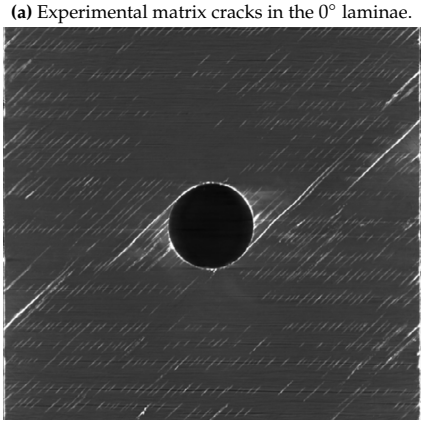

(c) Experimental matrix cracks in the 45° laminae.

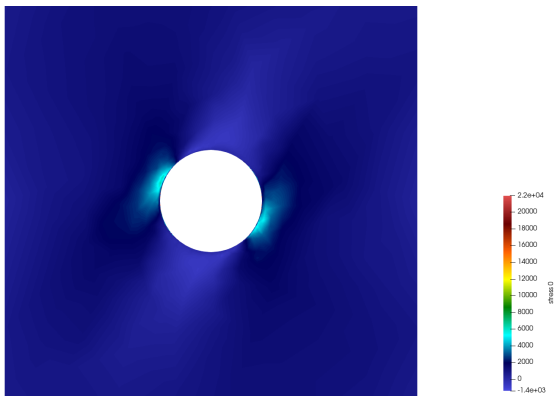

(d) Stress component $\widetilde{n}_{11}$ for the 45° laminae in the model.

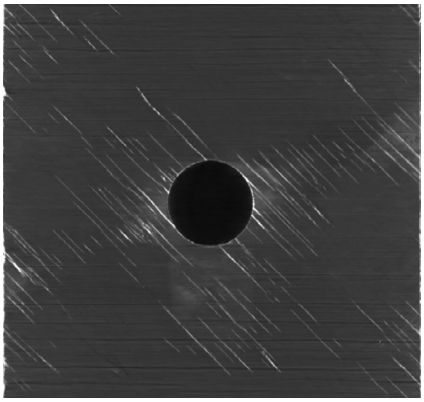

(e) Experimental matrix cracks in the −45° laminae.

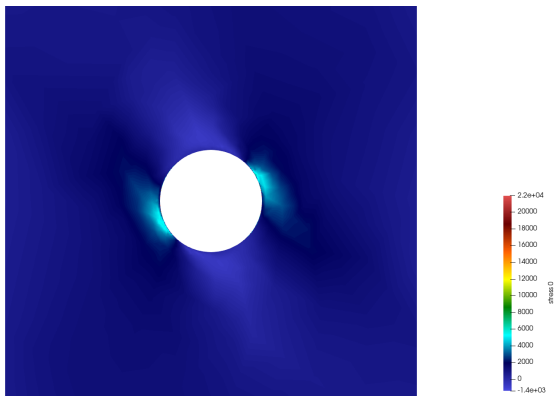

(f) Stress component $\widetilde{n}_{11}$ for the −45° laminae in the model.

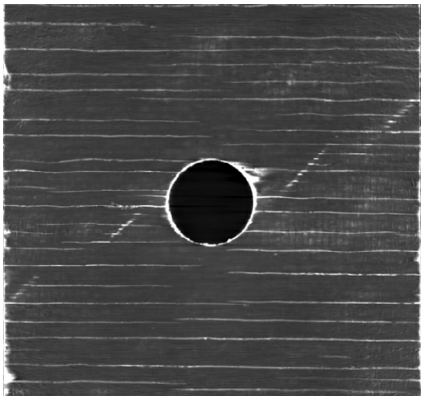

(g) Experimental matrix cracks in the −45° laminae.

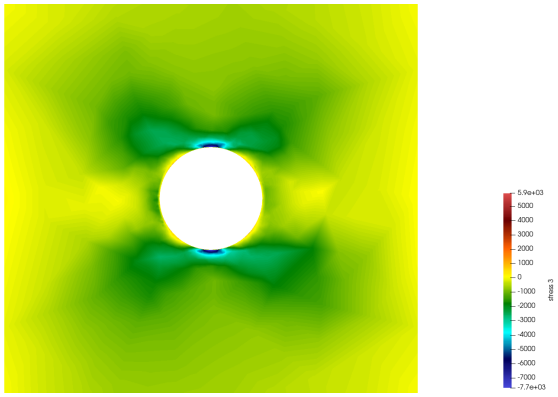

(h) Stress component $\widetilde{n}_{22}$ for the 90° laminae in the model.

Figure 4.25: Comparison of experimental matrix cracks [25] and model stress distributions for the 0°, 45°, −45°, and 90° laminae. For the 0°, 45°, and −45° laminae, the stress component $\widetilde{n}_{11}$ is analyzed; for the 90° lamina, the stress component $\widetilde{n}_{22}$ is considered. The model effectively illustrates the stress distributions that correspond to the observed matrix crack directions from the experiments.

The comparison of experimental matrix cracks and model stress distributions, as shown in Figure 4.25, illustrates the model's effectiveness in capturing the stress concentrations of various lamina orientations. The comparison focuses on the stress component $\widetilde{n}_{11}$ for the 0°, 45°, and −45° laminae, where the stress concentrations align closely with the direction of matrix cracking in the experimental results. For the 90° laminae, the stress component $\widetilde{n}_{22}$ is compared, as $\widetilde{n}_{11}$ is close to zero. This can be explained by the fact that stress is attracted to stiffness, and the 90° laminae lack stiffness in the x-direction.

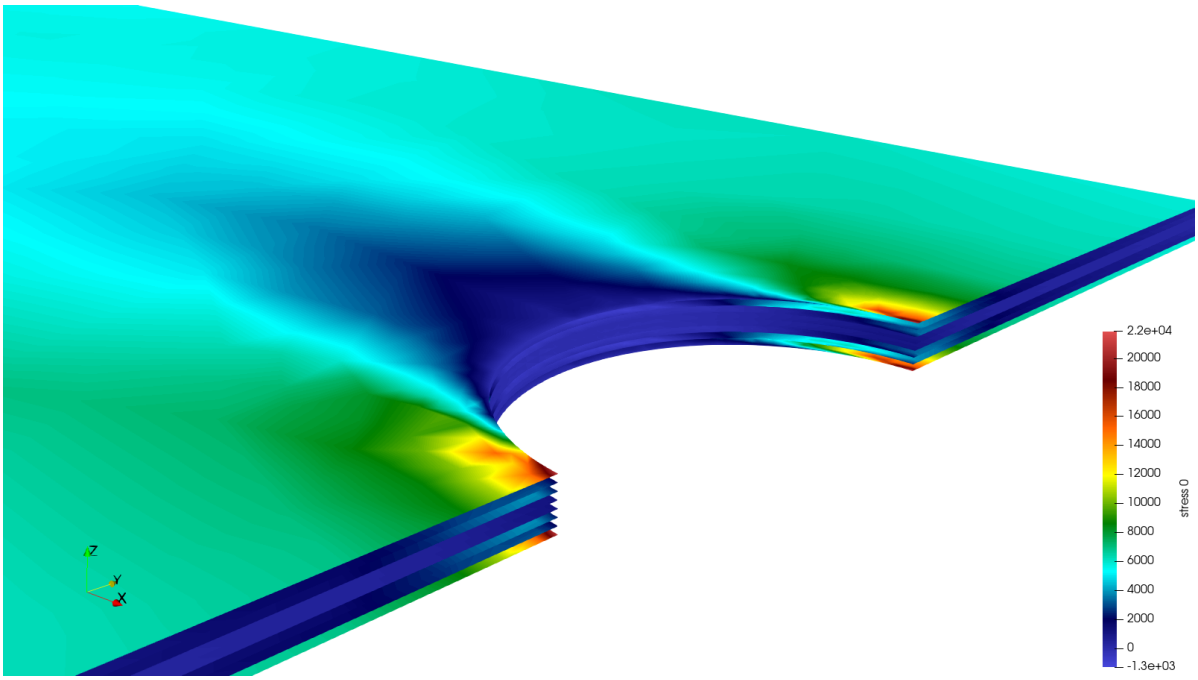

Figure 4.26: Open hole tension stress component $\widetilde{n}_{11}$ for the composite laminate layup [0°/45°/−45°/90°/90°/−45°/45°/0°]. The stress distribution is shown, illustrating the impact of the hole on the $\widetilde{n}_{11}$ stress field throughout the thickness of the laminate.

Figure 4.26 shows the complete model of the open hole tension test, visualizing the stress component $\widetilde{n}_{11}$ for the composite laminate layup [0°/45°/−45°/90°/90°/−45°/45°/0°]. The figure illustrates the impact of the hole on the $\widetilde{n}_{11}$ stress field throughout the thickness of the laminate. Notably, the stress concentrations around the hole reveal the influence of the fiber orientation on the stress distribution, with close to zero stress in the 90° laminae and very high stresses in the 0° laminae.

Chapter 5

Conclusion

The goal of this work was to develop a high-fidelity framework for modeling multi-layered composite structures by explicitly representing each layer. This approach allows for the accurate simulation of interlaminar interactions, particularly under large deformations and buckling conditions. By employing geometrically exact shell finite elements, this method enables the modeling of large deformations and buckling while effectively capturing the independent behavior of each layer. Consequently, the primary research objective previously stated is as follows:

Research Objective

To investigate the feasibility of high-fidelity Finite Element Methods for explicitly modeling each layer in multi-layered materials subjected to large deformations and buckling at the component level.

The research objective was achieved by employing the Discontinuous Galerkin method. This method is particularly well-suited for capturing the complexities of multi-layered composite structures, as it allows for the explicit representation of each individual layer, including their interlaminar interactions. By using the Discontinuous Galerkin method, the model effectively simulates these interactions under challenging conditions such as large deformations and buckling, which are critical for understanding the material's behavior in smart structures and buckling applications.

Sub-Question 1

Question

How can the Discontinuous Galerkin method be employed to model any number of layers through-the-thickness?

Answer

The Discontinuous Galerkin method can be applied to multi-layered structures by allowing for the explicit modeling of each layer through-the-thickness. By discretizing the equations for each layer and implementing interlaminar coupling, the method can capture the layer-specific behavior and interactions under various loading conditions.

To apply the Discontinuous Galerkin method through the thickness, two key aspects need to be addressed. First, each individual layer must be meshed using its own independent set of nodes (Subsection 3.6.1). Second, the interface forces between these layers must be incorporated into the weak form (Section 3.4).

To create any number of layers through the thickness, a base layer is first required. The mesh of this layer is then duplicated and shifted in the thickness direction until the desired number of layers is achieved. This process involves calculating the director at the nodes in the reference configuration and using it to offset each new layer, ensuring that any shape can be replicated without resorting to hardcoded geometries. Since each of these layers is meshed independently without the need for

added constraints, each layer maintains its own set of unknowns, effectively functioning as a Layerwise displacement field (Subsection 2.1.2).

It is important to note that the inertia of each layer must be adjusted to account for the new mass distribution. Simply adding layers without correcting the inertia would result in an inaccurate model. The parallel axis theorem must therefore be applied to ensure that the addition of layers does not alter the overall response of the structure (Subsection 3.6.2).

Sub-Question 2

Question

How do the multi-layer predictions from the proposed method compare to Equivalent Single Layer configurations across several benchmarks?

Answer

The proposed method can be compared to Equivalent Single Layer configuration using numerical benchmarks, such as the free vibration of a beam, post-buckling of a beam, beam roll-up, and beam twist. The four models are set-up to compare several aspects of the model: the first confirms proper rotational inertia calculation, the second ensures that distributing the load across all layers produces the same post-buckling response as a single-layer model, the third model tests performance under large torsional deformation, and the fourth evaluates large deformations in the classic Euler beam roll-up problem. the method showed good agreement with Equivalent Single Layer models, although some discrepancies, like in the beam twist case, may arise due to factors such as the incorrect stability parameter and load application.

To verify the proposed method, several benchmarks were created. The models included the free vibration of a beam, the beam roll-up problem, the beam twist problem, and the beam post-buckling problem. In most cases, a strong match was observed, with no visible error compared to the single-layer model. These four benchmarks were designed to verify key aspects of the overall modeling approach. The first model excites the shell using its first mode shape, allowing for a comparison with the analytical solution to confirm the correct calculation of rotational inertia for each layer. The second model assesses how the four configurations respond to the buckling load from a single-layer model, ensuring that load distribution across layers yields the same post-buckling response. The third model examines the behavior of a thick shell under an applied torque, evaluating its performance during significant torsional deformation. Lastly, the fourth model uses the classic Euler beam roll-up problem, where a moment is applied at the shell's tip, rolling it into a complete circle.

The beam twist exhibited significant absolute errors in displacement, reaching up to 50%. This discrepancy can be attributed to the stabilization parameter and the method of load application. Currently, the stabilization parameter maintains the correct distance between mid-surface nodes; however, this distance is not aligned with the director. It is believed that ensuring the correct distance between the mid-surface nodes in the direction of the director will resolve the issue of layer interpenetration. Additionally, in all models, the total load was distributed across all layers: membrane loads were divided equally among the layers, while moments were allocated based on each layer's contribution to the moment of inertia. This approach, combined with the stabilization term, may explain why, in one benchmark, the layers rotated in place instead of following the rotation of adjacent layer.

Sub-Question 3

Question

What adjustments are needed for the proposed method for it to be able to model interlaminar damage effectively along any interface using the Discontinuous Galerkin approach?

Answer

To model interlaminar damage effectively, modifications such as incorporating cohesive zone models at the interfaces is required. These adjustments will allow the Discontinuous Galerkin approach to account for the initiation and propagation of damage between layers, providing a more accurate simulation of interlaminar failure.

Since an extrinsic cohesive element is used, delamination initiation cannot be directly modeled. To address this, an initiation criterion must be employed, particularly a stress-based criterion. However, this requires capturing out-of-plane stresses on both sides of the interface. In the current implementation, a plane stress state is assumed, meaning out-of-plane normal stresses are absent. The out-of-plane shear stresses are captured due to the use of shear-flexible shells. It is possible, however, to incorporate out-of-plane normal stresses while maintaining the geometrically exact nature of the elements. This can be achieved by relaxing the inextensibility constraint on the directors. By introducing additional unknowns for the director stretch, out-of-plane normal stresses will be present, alongside the drilling moments (see Section 3.9).

When these stresses are available, a stress-based delamination failure criterion must be used to evaluate delamination initiation. While simple maximum stress criteria can be applied, more complex models that account for the interaction of out-of-plane stress components are also possible. The necessary stresses can be easily obtained from the implemented composite constitutive matrix on both the left and right sides of the interface. The average of these stresses is then combined with the out-of-plane normal vector in the consistency terms to evaluate fracture initiation (Section 3.4).

With all sub-questions addressed, the main research question can now be answered:

Main Research Question

How can high-fidelity Finite Element Methods be employed to investigate the feasibility of explicitly modeling each layer in multi-layered materials subjected to large deformations and buckling at the component level?

Answer Main Research Question

A high-fidelity Finite Element Method can be used to model interlaminar interactions in multi-layered materials by using the Discontinuous Galerkin approach. By discretizing each layer explicitly and implementing interlaminar coupling, the method captures layer-specific behavior under large deformations and buckling. Several numerical benchmarks demonstrate the method's ability to model each layer individually while producing accurate results at the component level. However, further adjustments—such as incorporating out-of-plane stresses and cohesive zone models—are required to accurately simulate interlaminar damage initiation and propagation at the interfaces. Additionally, modifications to the stability term are necessary to prevent layer interpenetration, which is believed to be the cause of the observed discrepancy.

The thesis demonstrates the applicability of the proposed method to model multi-layer composite components. It shows that a wide range of thicknesses can be effectively accommodated, from thick shells to very thin configurations. The use of second-order displacement elements and linear rotation elements ensured that no locking occurred, even at very small thicknesses, which is crucial for accurately modeling realistic composite structures. The bend-twist problem was modeled for the composite material, revealing a distinct twist when using a unidirectional symmetric layup. As anticipated,

the antisymmetric layup, characterized by symmetric upper and lower halves, exhibited no twisting, confirming that the mechanical behavior was accurately captured. Following this, the open hole tension test was conducted, demonstrating the influence of the fiber orientation on the stress concentrations around the hole compared to experimental results.

5.1. Recommendations for Future Work

If at this point there are still brave souls willing to take on this topic, several recommendations can be made for effectively modeling delaminations at arbitrary interface:

5.1.1. Through-the-Thickness Stretching

Including through-the-thickness stretching into shell models, as explained in Section 3.9, is essential for accurately capturing out-of-plane stresses, particularly if delaminations are to be modeled. Traditional shell theories, which assume an inextensible thickness, do not take into account the out-of-plane normal stress, leading to the model only being able to model shear delamination. By allowing the thickness stretch as an independent field, not constrained by the plane-stress condition, the three out-of-plane stresses can be used together in a failure criterion.

An advantage of shell models with thickness stretch is the implementation of full 3D constitutive models. Unlike the classical inextensible director theory, where the plane stress assumption must be explicitly enforced, formulations with an extensible director avoid this, allowing for direct use of 3D constitutive relations, while still recovering plane stress behavior for thin shells.

5.1.2. Integration of Cohesive Elements

Employing the Discontinuous Galerkin method to explicitly model each layer has proven feasible in this work. However, while cohesive elements for intralaminar damage are already established through the DG/CZM method, which has been successfully applied to homogeneous materials [19] and is currently under development for intralaminar damage in orthotropic materials [78], interlaminar cohesive elements should also be included. This addition will enable the modeling of delaminations within multi-layered composite structures along arbitrary interfaces without the artificial compliance observed in literature.

5.1.3. Support for Unsymmetric Laminates

The current framework is limited to symmetric laminates, see Subsection 3.5.2. However, unsymmetric laminates could provide more flexibility in tailoring stiffness. Unlike symmetric laminates, unsymmetric laminates introduce coupling between in-plane and out-of-plane loads, which leads to more complex behavior under mechanical loads. This complex coupling could be used to obtain a certain buckling shape. By including the possibility of unsymmetric laminates, the model will be able to capture important effects such as bending-shear and extension-twist coupling.

5.1.4. Parallel Implementation

By utilizing parallel computation, the workload can be distributed across multiple processors, thus reducing simulation time and enabling the analysis of larger, more detailed models that were previously not feasible. This approach will allow the current method to handle larger and more complex problems, making applications such as delamination modeling actually practical. The DG/CZM method leverages its well-established scalability, significantly reducing inter-processor communication. The only necessary communication occurs during the calculation of the interface stability term, requiring the exchange of the jump in displacement and directors across processor boundaries.

5.1.5. Shear Correction Factors

A shear correction factor of $\kappa = \frac{5}{6}$ was used in this work for all layers. While this is appropriate for isotropic materials, it is not generally valid for composite materials. As stated in Subsection 2.1.1, the shear correction factor depends on both the material properties and the layup [79]. Shear correction factors should be calculated for each layer, additionally both out-of-plane shear strains generally have different shear correction factors as well: $\kappa_{13} \neq \kappa_{23}$. The shear correction factor κ can be calculated by equating energies, as follows:

$$\kappa = \frac{\sum_{i=1}^{n} \kappa_i G_i h_i}{\sum_{i=1}^{n} G_i h_i} \tag{5.1}$$

In other words, the shear correction factor is the ratio between the corrected and uncorrected shear

stiffness. Here κ_i, G_i, and h_i represent the shear correction factors, shear modulus, and thickness of each layer, respectively. For certain layups, applying $\kappa = \frac{5}{6}$ uniformly across layers may still provide reasonable accuracy. However, for more complex layups or material properties, layer-specific shear correction factors are needed to capture the correct shear behavior.

Bibliography

[1] M. Cho and R. R. Parmerter. "An efficient higher-order plate theory for laminated composites". *Composite Structures* 20 (2 Jan. 1992), pp. 113–123. DOI: 10.1016/0263-8223(92)90067-M.

[2] G. Guarino and A. Milazzo. "A discontinuous Galerkin formulation for nonlinear analysis of multilayered shells refined theories". *International Journal of Mechanical Sciences* 255 (Oct. 2023). DOI: 10.1016/j.ijmecsci.2023.108426.

[3] H. M. Mourad, T. O. Williams, and F. L. Addessio. "Finite element analysis of inelastic laminated plates using a global-local formulation with delamination". *Computer Methods in Applied Mechanics and Engineering* 198 (3-4 Dec. 2008), pp. 542–554. DOI: 10.1016/j.cma.2008.09.006.

[4] D. Versino, H. M. Mourad, and T. O. Williams. "A global-local discontinuous Galerkin shell finite element for small-deformation analysis of multi-layered composites". *Computer Methods in Applied Mechanics and Engineering* 271 (Apr. 2014), pp. 269–295. DOI: 10.1016/j.cma.2013.12.007.

[5] D. Versino, H. M. Mourad, T. O. Williams, and F. L. Addessio. "A global-local discontinuous Galerkin finite element for finite-deformation analysis of multilayered shells". *Computer Methods in Applied Mechanics and Engineering* 283 (Jan. 2015), pp. 1401–1424. DOI: 10.1016/j.cma.2014.10.017.

[6] D. Li, S. Zhao, A. D. Ronch, J. Xiang, J. Drofelnik, Y. Li, L. Zhang, Y. Wu, M. Kintscher, H. P. Monner, A. Rudenko, S. Guo, W. Yin, J. Kirn, S. Storm, and R. D. Breuker. "A review of modelling and analysis of morphing wings". *Progress in Aerospace Sciences* 100 (June 2018), pp. 46–62. DOI: 10.1016/J.PAEROSCI.2018.06.002.

[7] H. P. Monner. "Realization of an optimized wing camber by using formvariable flap structures". *Aerospace Science and Technology* 5 (7 Oct. 2001), pp. 445–455. DOI: 10.1016/S1270-9638(01)01118-X.

[8] J. Zhang and C. Bisagni. "Buckling-driven mechanisms for twisting control in adaptive composite wings". *Aerospace Science and Technology* 118 (Nov. 2021), p. 107006. DOI: 10.1016/J.AST.2021.107006.

[9] C. G. Dávila and C. Bisagni. "Fatigue life and damage tolerance of postbuckled composite stiffened structures with initial delamination". *Composite Structures* 161 (Feb. 2017), pp. 73–84. DOI: 10.1016/J.COMPSTRUCT.2016.11.033.

[10] J. Action and F. A. Leone. "Progressive damage failure analysis of a multi-stringer post-buckled panel". *AIAA Scitech 2020 Forum* (2020). DOI: 10.2514/6.2020-1481.

[11] Y. Bazilevs, M. S. Pigazzini, A. Ellison, and H. Kim. "A new multi-layer approach for progressive damage simulation in composite laminates based on isogeometric analysis and Kirchhoff–Love shells. Part I: basic theory and modeling of delamination and transverse shear". *Computational Mechanics* 62 (3 Sept. 2018), pp. 563–585. DOI: 10.1007/s00466-017-1513-1.

[12] J. Tao and C. T. Sun. "Influence of Ply Orientation on Delamination in Composite Laminates". *Journal of Composite Materials* 32 (21 Nov. 1998), pp. 1933–1947. DOI: 10.1177/002199839803202103.

[13] H. Liu, B. G. Falzon, and W. Tan. "Predicting the Compression-After-Impact (CAI) strength of damage-tolerant hybrid unidirectional/woven carbon-fibre reinforced composite laminates". *Composites Part A: Applied Science and Manufacturing* 105 (Feb. 2018), pp. 189–202. DOI: 10.1016/J.COMPOSITESA.2017.11.021.

[14] C. Balzani and W. Wagner. "An interface element for the simulation of delamination in unidirectional fiber-reinforced composite laminates". *Engineering Fracture Mechanics* 75 (9 June 2008), pp. 2597–2615. DOI: 10.1016/j.engfracmech.2007.03.013.

[15] P. Ladeveze and E. LeDantec. "Damage modelling of the elementary ply for laminated composites". *Composites Science and Technology* 43 (3 Jan. 1992), pp. 257–267. DOI: 10.1016/0266-3538(92)90097-M.

[16] J. Reinoso, M. Paggi, and A. Blázquez. "A nonlinear finite thickness cohesive interface element for modeling delamination in fibre-reinforced composite laminates". *Composites Part B: Engineering* 109 (Jan. 2017), pp. 116–128. DOI: 10.1016/J.COMPOSITESB.2016.10.042.

[17] P. W. Harper and S. R. Hallett. "Cohesive zone length in numerical simulations of composite delamination". *Engineering Fracture Mechanics* 75 (16 Nov. 2008), pp. 4774–4792. DOI: 10.1016/j.engfracmech.2008.06.004.

[18] P. P. Camanho, C. G. Dávila, and M. F. D. Moura. "Numerical simulation of mixed-mode progressive delamination in composite materials". *Journal of Composite Materials* 37 (16 Jan. 2003), pp. 1415–1438. DOI: 10.1177/0021998303034505.

[19] B. Talamini. "Simulation of Deformation and Fracture in Very Large Shell Structures". PhD thesis. Massachusetts Institute of Technology, 2015.

[20] A. De-Andrés, J. L. Pérez, and M. Ortiz. "Elastoplastic finite element analysis of three-dimensional fatigue crack growth in aluminum shafts subjected to axial loading". *International Journal of Solids and Structures* 36 (15 May 1999), pp. 2231–2258. DOI: 10.1016/S0020-7683(98)00059-6.

[21] D. Bruno, F. Greco, and P. Lonetti. "Interaction Between Interlaminar and Intralaminar Damage in Fiber-Reinforced Composite Laminates". *International Journal for Computational Methods in Engineering Science and Mechanics* 9 (6 2008), pp. 358–373. DOI: 10.1080/15502280802365824.

[22] F. P. van der Meer, L. J. Sluys, S. R. Hallett, and M. R. Wisnom. "Computational modeling of complex failure mechanisms in laminates". *Journal of Composite Materials* 46 (5 Sept. 2011), pp. 603–623. DOI: 10.1177/0021998311410473.

[23] C. Bouvet, S. Rivallant, and J. J. Barrau. "Low velocity impact modeling in composite laminates capturing permanent indentation". *Composites Science and Technology* 72 (16 Nov. 2012), pp. 1977–1988. DOI: 10.1016/J.COMPSCITECH.2012.08.019.

[24] N. V. De Carvalho, B. Y. Chen, S. T. Pinho, J. G. Ratcliffe, P. M. Baiz, and T. E. Tay. "Modeling delamination migration in cross-ply tape laminates". *Composites Part A: Applied Science and Manufacturing* 71 (Apr. 2015), pp. 192–203. DOI: 10.1016/J.COMPOSITESA.2015.01.021.

[25] G. Vigueras, F. Sket, C. Samaniego, L. Wu, L. Noels, D. Tjahjanto, E. Casoni, G. Houzeaux, A. Makradi, J. M. Molina-Aldareguia, M. Vázquez, and A. Jérusalem. "An XFEM/CZM implementation for massively parallel simulations of composites fracture". *Composite Structures* 125 (July 2015), pp. 542–557. DOI: 10.1016/J.COMPSTRUCT.2015.01.053.

[26] K. Yun, S. Kwak, Z. Wang, M. Chang, J. Kim, J. Liu, and C. Ri. "A Damage Model Reflecting the Interaction between Delamination and Intralaminar Crack for Failure Analysis of FRP Laminates". *Applied Sciences* 9 (Jan. 2019), p. 314. DOI: 10.3390/app9020314.

[27] W. H. Reed and T. R. Hill. *"Triangular mesh methods for the neutron transport equation"*. Tech. rep. LA-UR-73-479. Los Alamos Scientific Laboratory, Oct. 1973.

[28] L. Noels and R. Radovitzky. "An explicit discontinuous Galerkin method for non-linear solid dynamics. Formulation, parallel implementation and scalability properties." *International Journal for Numerical Methods in Engineering* 74.9 (2007), pp. 1393–1420. DOI: 10.1002/nme.2213.

[29] D. Versino, H. M. Mourad, C. G. Dávila, and F. L. Addessio. "A thermodynamically consistent discontinuous Galerkin formulation for interface separation". *Composite Structures* 133 (Dec. 2015), pp. 595–606. DOI: 10.1016/j.compstruct.2015.07.080.

[30] D. Uribe-Suárez, P. O. Bouchard, M. Delbo, and D. Pino-Muñoz. "Numerical modeling of crack propagation with dynamic insertion of cohesive elements". *Engineering Fracture Mechanics* 227 (Mar. 2020), p. 106918. DOI: 10.1016/J.ENGFRACMECH.2020.106918.

[31] L. Huo, C. Kassapoglou, and R. C. Alderliesten. "A criterion for predicting delamination growth in composite laminates". *Materials and Design* 223 (Nov. 2022), p. 111160. DOI: 10.1016/J.MATDES.2022.111160.

[32] G. Guarino, A. Milazzo, and V. Gulizzi. "Equivalent-Single-Layer discontinuous Galerkin methods for static analysis of multilayered shells". *Applied Mathematical Modelling* 98 (Oct. 2021), pp. 701–721. DOI: 10.1016/j.apm.2021.05.024.

[33] J. Reddy. *Mechanics of Laminated Composite Plates and Shells Theory and Analysis*. 2nd ed. CRC Press, 2003.

[34] W. Sprenger, F. Gruttmann, and W. Wagner. "Delamination growth analysis in laminated structures with continuum-based 3D-shell elements and a viscoplastic softening model". *Computer Methods in Applied Mechanics and Engineering* 185 (2-4 May 2000), pp. 123–139. DOI: 10.1016/S0045-7825(99)00255-8.

[35] G. Kirchhoff. "4. Über das Gleichgewicht und die Bewegung einer elastischen Scheibe". *Journal fur die Reine und Angewandte Mathematik* 1850 (40 Jan. 1850), pp. 51–88. DOI: 10.1515/crll.1850.40.51.

[36] A. Brugnoli, D. Alazard, V. Pommier-Budinger, and D. Matignon. "Port-Hamiltonian formulation and symplectic discretization of plate models Part II: Kirchhoff model for thin plates". *Applied Mathematical Modelling* 75 (Nov. 2019), pp. 961–981. DOI: 10.1016/J.APM.2019.04.036.

[37] E. Reissner. "The Effect of Transverse Shear Deformation on the Bending of Elastic Plates". *Journal of Applied Mechanics* 12 (2 June 1945), A69–A77. DOI: 10.1115/1.4009435.

[38] R. D. Mindlin. "Influence of Rotatory Inertia and Shear on Flexural Motions of Isotropic, Elastic Plates". *Journal of Applied Mechanics* 18 (1 Mar. 1951), pp. 31–38. DOI: 10.1115/1.4010217.

[39] M. Sadeghmanesh, H. Haddadpour, M. T. Abadi, and H. M. Navazi. "A method for selection of structural theories for low to high frequency vibration analyses". *European Journal of Mechanics - A/Solids* 75 (May 2019), pp. 27–40. DOI: 10.1016/J.EUROMECHSOL.2019.01.004.

[40] J. Simo and D. Fox. "On a stress resultant geometrically exact shell model. Part I: formulation and optimal parametrization". 72 (1989), pp. 267–304.

[41] J. Simo, D. Fox, and M. Rifai. "On a stress resultant geometrically exact shell model. Part III: computational aspects of the non-linear theory". 79 (1990), pp. 21–70. DOI: 10.1016/0045-7825(90)90094-3.

[42] L. Noels and R. Radovitzky. "A new discontinuous Galerkin method for Kirchhoff-Love shells". *Computer Methods in Applied Mechanics and Engineering* 197 (33-40 June 2008), pp. 2901–2929. DOI: 10.1016/J.CMA.2008.01.018.

[43] J. N. Reddy. "A generalization of two-dimensional theories of laminated composite plates". *Communications in Applied Numerical Methods* 3 (3 May 1987), pp. 173–180. DOI: 10.1002/CNM.1630030303.

[44] J. N. Reddy, E. J. Barbero, and J. L. Teply. "A plate bending element based on a generalized laminate plate theory". *International Journal for Numerical Methods in Engineering* 28 (10 Oct. 1989), pp. 2275–2292. DOI: 10.1002/NME.1620281006.

[45] M. D. Sciuva. "Development of an anisotropic, multilayered, shear-deformable rectangular plate element". *Computers and Structures* 21 (4 Jan. 1985), pp. 789–796. DOI: 10.1016/0045-7949(85)90155-5.

[46] Y. B. Cho and R. C. Averill. "First-order zig-zag sublaminate plate theory and finite element model for laminated composite and sandwich panels". *Composite Structures* 50 (1 Sept. 2000), pp. 1–15. DOI: 10.1016/S0263-8223(99)00063-X.

[47] T. O. Williams. "A generalized multilength scale nonlinear composite plate theory with delamination". *International Journal of Solids and Structures* 36 (20 July 1999), pp. 3015–3050. DOI: 10.1016/S0020-7683(98)00138-3.

[48] A. Sharma and D. K. Dubey. "Effect of porosity on shock propagation behaviour of single crystal aluminium: A molecular dynamics investigation". *Mechanics of Materials* 177 (Feb. 2023), p. 104535. DOI: 10.1016/J.MECHMAT.2022.104535.

[49] Y. Mi, M. A. Crisfield, G. A. Davies, and H. B. Hellweg. "Progressive Delamination Using Interface Elements". *Journal of Composite Materials* 32 (14 July 1998), pp. 1246–1272. DOI: 10.1177/002199839803201401.

[50] B. Y. Chen, S. T. Pinho, N. V. D. Carvalho, P. M. Baiz, and T. E. Tay. "A floating node method for the modelling of discontinuities in composites". *Engineering Fracture Mechanics* 127 (Sept. 2014), pp. 104–134. DOI: 10.1016/J.ENGFRACMECH.2014.05.018.

[51] Dassault Systèmes. *Abaqus User's Manual*. Version 2023. 2023.

[52] T. Belytschko and T. Black. "Elastic crack growth in finite element with minimal remeshing". *International Journal for Numerical Methods in Engineering* 45.5 (1999), pp. 601–620. DOI: 10.1002/(SICI)1097-0207(19990620)45:5<601::AID-NME598>3.0.CO;2-S.

[53] F. P. Van Der Meer and L. J. Sluys. "Continuum Models for the Analysis of Progressive Failure in Composite Laminates". *Journal of Composite Materials* 43 (20 Aug. 2009), pp. 2131–2156. DOI: 10.1177/0021998309343054.

[54] ANSYS Inc. *ANSYS User's Manual*. Release 2023 R2. 2023.

[55] D. S. Dugdale. "Yielding of steel sheets containing slits". *Journal of the Mechanics and Physics of Solids* 8 (2 May 1960), pp. 100–104. DOI: 10.1016/0022-5096(60)90013-2.

[56] G. Barenblatt. "The Mathematical Theory of Equilibrium Cracks in Brittle Fracture". *Advances in Applied Mechanics* 7 (Jan. 1962), pp. 55–129. DOI: 10.1016/S0065-2156(08)70121-2.

[57] J. W. Simon, D. Höwer, B. Stier, and S. Reese. "Meso-mechanically motivated modeling of layered fiber reinforced composites accounting for delamination". *Composite Structures* 122 (Apr. 2015), pp. 477–487. DOI: 10.1016/J.COMPSTRUCT.2014.12.006.

[58] C. Furtado, G. Catalanotti, A. Arteiro, P. J. Gray, B. L. Wardle, and P. P. Camanho. "Simulation of failure in laminated polymer composites: Building-block validation". *Composite Structures* 226 (Oct. 2019), pp. 1–23. DOI: 10.1016/J.COMPSTRUCT.2019.111168.

[59] M. Paggi and P. Wriggers. "A nonlocal cohesive zone model for finite thickness interfaces - Part I: Mathematical formulation and validation with molecular dynamics". *Computational Materials Science* 50 (5 Mar. 2011), pp. 1625–1633. DOI: 10.1016/j.commatsci.2010.12.024.

[60] K. Park and G. H. Paulino. "Cohesive zone models: A critical review of traction-separation relationships across fracture surfaces". *Applied Mechanics Reviews* 64 (6 2011). DOI: 10.1115/1.4023110.

[61] J. C. Schellekens and R. D. Borst. "Free edge delamination in carbon-epoxy laminates: a novel numerical/experimental approach". *Composite Structures* 28 (4 Jan. 1994), pp. 357–373. DOI: 10.1016/0263-8223(94)90118-X.

[62] A. Turon, P. P. Camanho, A. Soto, and E. V. González. "8.8 Analysis of Delamination Damage in Composite Structures Using Cohesive Elements". Elsevier, Jan. 2018, pp. 136–156. DOI: 10.1016/B978-0-12-803581-8.10059-1.

[63] X. Lu, M. Ridha, B. Y. Chen, V. B. Tan, and T. E. Tay. "On cohesive element parameters and delamination modelling". *Engineering Fracture Mechanics* 206 (Feb. 2019), pp. 278–296. DOI: 10.1016/J.ENGFRACMECH.2018.12.009.

[64] V. Tvergaard. "Effect of fibre debonding in a whisker-reinforced metal". *Materials Science and Engineering: A* 125 (2 June 1990), pp. 203–213. DOI: 10.1016/0921-5093(90)90170-8.

[65] S. Abdel-Monsef, B. H. Tijs, J. Renart, and A. Turon. "Accurate simulation of delamination under mixed-mode loading using a multilinear cohesive law". *Engineering Fracture Mechanics* 284 (May 2023), p. 109233. DOI: 10.1016/J.ENGFRACMECH.2023.109233.

[66] F. Freddi and E. Sacco. "An interface damage model accounting for in-plane effects". *International Journal of Solids and Structures* 51 (25-26 Dec. 2014), pp. 4230–4244. DOI: 10.1016/j.ijsolstr.2014.08.010.

[67] A. A. Griffith. "The phenomena of rupture and flow in solids". *Philosophical Transactions of the Royal Society of London A:Mathematical, Physical and Engineering Sciences* 221 (582-593 Jan. 1921), pp. 163–198. DOI: 10.1098/RSTA.1921.0006.

[68] G. R. Irwin. "Analysis of Stresses and Strains Near the End of a Crack Traversing a Plate". *Journal of Applied Mechanics* 24 (3 Sept. 1957), pp. 361–364. DOI: 10.1115/1.4011547.

[69] B. L. Talamini and R. Radovitzky. "A discontinuous Galerkin method for nonlinear shear-flexible shells". *Computer Methods in Applied Mechanics and Engineering* 303 (May 2016), pp. 128–162. DOI: 10.1016/J.CMA.2016.01.001.

[70] B. L. Talamini and R. Radovitzky. "A parallel discontinuous Galerkin/cohesive-zone computational framework for the simulation of fracture in shear-flexible shells". *Computer Methods in Applied Mechanics and Engineering* 317 (Apr. 2017), pp. 480–506. DOI: 10.1016/J.CMA.2016.12.018.

[71] M. E. Gurtin. "A gradient theory of small-deformation isotropic plasticity that accounts for the Burgers vector and for dissipation due to plastic spin". 52 (2004), pp. 2245–2568. DOI: 10.1016/j.jmps.2004.04.010.

[72] M. E. Gurtin, E. Fried, and L. Anand. *The Mechanics and Thermodynamics of Continua*. Cambridge University Press, 2010.

[73] J. Simo, D. Fox, and M. Rifai. "On a stress resultant geometrically exact shell model. Part IV: variable thickness shells with through-the-thickness stretching". 81 (1990), pp. 91–126. DOI: 10.1016/0045-7825(90)90143-A.

[74] T. J. Hughes. *The finite element method: Linear static and dynamic finite element analysis*. New York: Dover Publications, Inc, 2000.

[75] J. S. Wu and T. L. Lin. "Free vibration analysis of a uniform cantilever beam with point masses by an analytical-and-numerical-combined method". *Journal of Sound and Vibration* 136 (2 Jan. 1990), pp. 201–213. DOI: 10.1016/0022-460X(90)90851-P.

[76] B. Wu, A. Pagani, M. Filippi, W. Q. Chen, and E. Carrera. "Large-deflection and post-buckling analyses of isotropic rectangular plates by Carrera Unified Formulation". *International Journal of Non-Linear Mechanics* 116 (Nov. 2019), pp. 18–31. DOI: 10.1016/J.IJNONLINMEC.2019.05.004.

[77] C. Bisagni and P. Cordisco. "An experimental investigation into the buckling and post-buckling of CFRP shells under combined axial and torsion loading". *Composite Structures* 60 (4 June 2003), pp. 391–402. DOI: 10.1016/S0263-8223(03)00024-2.

[78] F. Maggioli. "A Novel Approach to Modeling Arbitrary Damage in Composite Structures through a Discontinuous Galerkin Cohesive Zone Model". MA thesis. Delft University of Technology, 2024.

[79] S. Vlachoutsis. "Shear correction factors for plates and shells". *International Journal for Numerical Methods in Engineering* 33 (7 May 1992), pp. 1537–1552. DOI: 10.1002/NME.1620330712.

[80] J. Mergheim, E. Kuhl, and P. Steinmann. "A hybrid discontinuous Galerkin/interface method for the computational modelling of failure". *Communication in Numerical Methods in Engineering* 20 (2004), pp. 511–519. DOI: 10.1002/cnm.689.

[81] J. N. Reddy and R. A. Arciniega. "Shear Deformation Plate and Shell Theories: From Stavsky to Present". *Mechanics of Advanced Materials and Structures* 11 (Nov. 2004), pp. 535–582. DOI: 10.1080/15376490490452777.

[82] H. Goldstein, C. P. Poole, and J. L. Safko. *Classical Mechanics*. 3rd ed. San Francisco: Addison-Wesley, 2002.

Appendix A

Weak Form of the Dynamic Linear Momentum Equation

The body experiences a force per unit mass $\mathbf{f}$. Its boundary surface ∂B_0 is divided into two distinct parts: a Dirichlet section $\partial_D B_0$, where displacements are fixed to $\bar{u}$, and a Neumann section $\partial_N B_0$, where surface tractions are specified as $\bar{\boldsymbol{T}}$. It holds that $\partial B_0 = \partial_D B_0 \cup \partial_N B_0$ and $\partial_D B_0 \cap \partial_N B_0 = \emptyset$. The governing equations in the material form are [28]:

$$\nabla_0 \cdot \boldsymbol{P} + \mathbf{f} = \rho_0 \ddot{u} \quad \forall \mathbf{X} \in B_0 \tag{A.1a}$$
$$u = \bar{u} \quad \forall \mathbf{X} \in \partial_D B_0 \tag{A.1b}$$
$$\boldsymbol{P} \cdot \mathbf{t} = \bar{\boldsymbol{T}} \quad \forall \mathbf{X} \in \partial_N B_0 \tag{A.1c}$$

The finite element discretization approximates the domain, denoted as $B_{0h} = \bigcup_{e=1}^{E} \bar{\Omega}_0^e$, where $\bar{\Omega}_0^e$ is the union of the elemental domain Ω_0^e with its boundary $\partial\Omega_0^e$. The elemental boundary consists of multiple parts, namely:

$$\partial\Omega_0^e = \partial_D\Omega_0^e \cup \partial_N\Omega_0^e \cup \partial_I\Omega_0^e \tag{A.2a}$$
$$\partial_D\Omega_0^e = \Omega_0^e \cap \partial_D B_{0h} \tag{A.2b}$$
$$\partial_N\Omega_0^e = \Omega_0^e \cap \partial_N B_{0h} \tag{A.2c}$$
$$\partial_I B_{0h} = \left[\bigcup_{e=1}^{E} \partial\Omega_0^e\right] \setminus \partial B_{0h} \tag{A.2d}$$

Where $\partial_I B_{0h}$ refers to the set of all internal boundaries that are specific to the Discontinuous Galerkin method.
Multiplying the governing equation with a test function and integrating over the body results in the weak form:

$$\int_{B_{0h}} \delta u \cdot (\nabla_0 \cdot \boldsymbol{P} + \mathbf{f})\, dV = \int_{B_{0h}} \delta u \cdot \rho_0 \ddot{u}\, dV \tag{A.3}$$

Which can be rewritten as:

$$\int_{B_{0h}} \delta u \cdot \rho_0 \ddot{u}\, dV - \int_{B_{0h}} \delta u \cdot \nabla_0 \cdot \boldsymbol{P}\, dV - \int_{B_{0h}} \delta u \cdot \mathbf{f}\, dV = 0 \tag{A.4}$$

The integrals over the body can be written as a summation of integrals over the elemental domains:

$$\sum_{e=1}^{n} \int_{\Omega_0^e} \delta u \cdot \rho_0 \ddot{u}\, dV - \sum_{e=1}^{n} \int_{\Omega_0^e} \delta u_i \cdot \frac{\partial P_{ij}}{\partial X_j}\, dV - \sum_{e=1}^{n} \int_{\Omega_0^e} \delta u \cdot \mathbf{f}\, dV = 0 \tag{A.5}$$

Applying integration by parts to the second term results in the addition of an external boundary term:

$$\sum_{e=1}^{n}\int_{\Omega_0^e}\delta u\cdot\rho_0\ddot{u}\,dV+\sum_{e=1}^{n}\int_{\Omega_0^e}\boldsymbol{P}:\nabla_0\delta u\,dV-\boxed{\sum_{e=1}^{n}\int_{\partial\Omega_0^e}\delta u\cdot\boldsymbol{P}\cdot\mathbf{t}\,dS}-\sum_{e=1}^{n}\int_{\Omega_0^e}\delta u\cdot\mathbf{f}\,dV=0 \tag{A.6}$$

Now focussing on this external boundary term which can be rewritten over the Dirichlet, Neumann, and internal boundaries using Equation A.2 as:

$$\begin{aligned}\boxed{\sum_{e=1}^{n}\int_{\partial\Omega_0^e}\delta u\cdot\boldsymbol{P}\cdot\mathbf{t}\,dS}&=\cancelto{0}{\sum_{e=1}^{n}\int_{\partial_D\Omega_0^e}\delta u\cdot\boldsymbol{P}\cdot\mathbf{t}\,dS}+\sum_{e=1}^{n}\int_{\partial_N\Omega_0^e}\delta u\cdot\boldsymbol{P}\cdot\mathbf{t}\,dS+\sum_{e=1}^{n}\int_{\partial_I\Omega_0^e}\delta u\cdot\boldsymbol{P}\cdot\mathbf{t}\,dS\\&=\sum_{e=1}^{n}\int_{\partial_N\Omega_0^e}\delta u\cdot\bar{\boldsymbol{T}}\,dS+\sum_{e=1}^{n}\int_{\partial_I\Omega_0^e}\delta u\cdot\boldsymbol{P}\cdot\mathbf{t}\,dS\end{aligned} \tag{A.7}$$

Since the variation of displacement over the Dirichlet boundary is zero, this term cancels out leaving a Neumann and internal boundary term:

$$\begin{aligned}&\sum_{e=1}^{n}\int_{\Omega_0^e}\delta u\cdot\rho_0\ddot{u}\,dV+\sum_{e=1}^{n}\int_{\Omega_0^e}\boldsymbol{P}:\nabla_0\delta u\,dV-\boxed{\sum_{e=1}^{n}\int_{\partial_I\Omega_0^e}\delta u\cdot\boldsymbol{P}\cdot\mathbf{t}\,dS}-\sum_{e=1}^{n}\int_{\partial_N\Omega_0^e}\delta u\cdot\bar{\boldsymbol{T}}\,dS\\&-\sum_{e=1}^{n}\int_{\Omega_0^e}\delta u\cdot\mathbf{f}\,dV=0\end{aligned} \tag{A.8}$$

Now the Internal boundary term can be rewritten using the jump and average operators by noting that $\mathbf{t}^+$ is equal to $-\mathbf{t}^-$:

$$\begin{aligned}\boxed{\sum_{e=1}^{n}\int_{\partial_I\Omega_0^e}\delta u\cdot\boldsymbol{P}\cdot\mathbf{t}\,dS}&=\int_{\partial_I\Omega_0^1}\delta u\cdot\boldsymbol{P}\cdot\mathbf{t}^+\,dS+\int_{\partial_I\Omega_0^2}\delta u\cdot\boldsymbol{P}\cdot\mathbf{t}^-\,dS+\ldots+\int_{\partial_I\Omega_0^{n-1}}\delta u\cdot\boldsymbol{P}\cdot\mathbf{t}^+\,dS\\&+\int_{\partial_I\Omega_0^n}\delta u\cdot\boldsymbol{P}\cdot\mathbf{t}^-\,dS=-\boxed{\int_{\partial_I B_{0h}}[\![\delta u\cdot\boldsymbol{P}]\!]\cdot\mathbf{t}\,dS}\end{aligned} \tag{A.9}$$

The last term can be rewritten and simplified since the jump in stress $[\![\boldsymbol{P}]\!]$ is zero across crack interfaces:

$$\boxed{\int_{\partial_I B_{0h}}[\![\delta u\cdot\boldsymbol{P}]\!]\cdot\mathbf{t}\,dS}=\int_{\partial_I B_{0h}}[\![\delta u]\!]\cdot\{\boldsymbol{P}\}\cdot\mathbf{t}\,dS+\cancelto{0}{\int_{\partial_I B_{0h}}\{\delta u\}\cdot[\![\boldsymbol{P}]\!]\cdot\mathbf{t}\,dS} \tag{A.10}$$

Substituting this result into the weak form results in:

$$\begin{aligned}&\sum_{e=1}^{n}\int_{\Omega_0^e}\delta u\cdot\rho_0\ddot{u}\,dV+\sum_{e=1}^{n}\int_{\Omega_0^e}\boldsymbol{P}:\nabla_0\delta u\,dV+\int_{\partial_I B_{0h}}[\![\delta u]\!]\cdot\{\boldsymbol{P}\}\cdot\mathbf{t}\,dS-\sum_{e=1}^{n}\int_{\partial_N\Omega_0^e}\delta u\cdot\bar{\boldsymbol{T}}\,dS\\&-\sum_{e=1}^{n}\int_{\Omega_0^e}\delta u\cdot\mathbf{f}\,dV=0\end{aligned} \tag{A.11}$$

At this point, the summation of the elemental body integrals can be rewritten as an integral over the entire body B_{0h} again:

$$\begin{aligned}&\int_{B_{0h}}\delta u\cdot\rho_0\ddot{u}\,dV+\boxed{\int_{B_{0h}}\boldsymbol{P}:\nabla_0\delta u\,dV}+\int_{\partial_I B_{0h}}[\![\delta u]\!]\cdot\{\boldsymbol{P}\}\cdot\mathbf{t}\,dS+\int_{\partial_I B_{0h}}\frac{\beta}{h_s}[\![u]\!]\cdot[\![\delta u]\!]\,dS\\&-\int_{\partial_N B_{0h}}\delta u\cdot\bar{\boldsymbol{T}}\,dS-\int_{B_{0h}}\delta u\cdot\mathbf{f}\,dV=0\end{aligned} \tag{A.12}$$

The second term can be rewritten using the equality $\delta \boldsymbol{F} = \frac{\partial \delta u}{\partial \mathbf{X}} = \nabla_0 \delta u$:

$$\boxed{\int_{B_{0h}} \boldsymbol{P} : \nabla_0 \delta u \, dV} = \int_{B_{0h}} \boldsymbol{P} : \delta \boldsymbol{F} \, dV \tag{A.13}$$

Now the stability terms over the internal boundary are introduced by simply adding it to the weak form:

$$\begin{aligned} &\int_{B_{0h}} \delta u \cdot \rho_0 \ddot{u} \, dV + \int_{B_{0h}} \boldsymbol{P} : \delta \boldsymbol{F} \, dV + \boxed{\int_{\partial_I B_{0h}} [\![\delta u]\!] \cdot \{\boldsymbol{P}\} \cdot \mathbf{t} \, dS + \int_{\partial_I B_{0h}} \frac{\beta}{h_s} [\![u]\!] \cdot [\![\delta u]\!] \, dS} \\ &= \int_{\partial_N B_{0h}} \delta u \cdot \bar{\boldsymbol{T}} \, dS + \int_{B_{0h}} \delta u \cdot \mathbf{f} \, dV \end{aligned} \tag{A.14}$$

The terms over the internal boundaries can be rewritten as a summation over the interfaces k:

$$\begin{aligned} &\boxed{\int_{\partial_I B_{0h}} [\![\delta u]\!] \cdot \{\boldsymbol{P}\} \cdot \mathbf{t} \, dS + \int_{\partial_I B_{0h}} \frac{\beta}{h_s} [\![u]\!] \cdot [\![\delta u]\!] \, dS} = \sum_{k=1}^{n-1} \int_{\partial_I \Omega_0^k} [\![\delta u]\!]^{(k)} \cdot \{\boldsymbol{P}\}^{(k)} \cdot \mathbf{t} \, dS \\ &+ \sum_{k=1}^{n-1} \int_{\partial_I \Omega_0^k} \frac{\beta}{h_s^{(k)}} [\![u]\!]^{(k)} \cdot [\![\delta u]\!]^{(k)} \, dS \end{aligned} \tag{A.15}$$

As explained in [80], a parameter α can be introduced to disable the stability and consistency terms while simultaneously activating the cohesive traction. This parameter illustrates the strength of the Discontinuous Galerkin method, as it allows for the selection of either stability tractions or cohesive tractions based on the failure criterion:

$$\begin{aligned} &\int_{B_{0h}} \delta u \cdot \rho_0 \ddot{u} \, dV + \int_{B_{0h}} \boldsymbol{P} : \delta \boldsymbol{F} \, dV + \sum_{k=1}^{n-1} \int_{\partial_I \Omega_0^k} (1-\alpha) [\![\delta u]\!]^{(k)} \cdot \{\boldsymbol{P}\}^{(k)} \cdot \mathbf{t} \, dS + \sum_{k=1}^{n-1} \int_{\partial_I \Omega_0^k} \alpha [\![\delta u]\!]^{(k)} \cdot \boldsymbol{T_{TSL}}^{(k)} \, dS \\ &+ \sum_{k=1}^{n-1} \int_{\partial_I \Omega_0^k} (1-\alpha) \frac{\beta}{h_s^{(k)}} [\![u]\!]^{(k)} \cdot [\![\delta u]\!]^{(k)} \, dS = \int_{\partial_N B_{0h}} \delta u \cdot \bar{\boldsymbol{T}} \, dS + \int_{B_{0h}} \delta u \cdot \mathbf{f} \, dV \end{aligned} \tag{A.16}$$

For plate and shell structures, integration over the domain can be represented as integration over the mid-surface of the plate followed by integration over the thickness of the plate [33]:

$$\int_V \dots dV = \int_h \int_{\mathcal{S}} \dots \mu d\mathcal{S} d\xi_3, \quad \int_h \dots d\xi_3 = \sum_{k=1}^{n} \int_{h^{(k)}} \dots d\xi_3 = \sum_{k=1}^{n} h^{(k)} \int_{\xi_3^{(k-1)}}^{\xi_3^{(k)}} \dots d\xi_3 \tag{A.17}$$

Since tractions and forces can only be applied the the shell mid-surface, the Neumann boundary integral needs to be slightly rewritten:

$$\int_{\partial_N B_{0h}} \delta u \cdot \bar{\boldsymbol{T}} \, dS = \int_h \int_{\partial_N \mathcal{S}_h} \delta u \cdot \bar{\boldsymbol{T}} \, \mu d\mathcal{S} d\xi_3 \tag{A.18}$$

Finally the weak form can be rewritten as:

$$\begin{aligned} &\int_h \int_{\mathcal{S}_h} \delta u \cdot \rho_0 \ddot{u} \, \mu d\mathcal{S} d\xi_3 + \int_h \int_{\mathcal{S}_h} \boldsymbol{P} : \delta \boldsymbol{F} \, \mu d\mathcal{S} d\xi_3 + \sum_{k=1}^{n-1} \int_{\mathcal{S}_h} (1-\alpha) [\![\delta u]\!]^{(k)} \cdot \{\boldsymbol{P}\}^{(k)} \cdot \mathbf{t} \, \mu^{(k)} d\mathcal{S} \\ &+ \sum_{k=1}^{n-1} \int_{\mathcal{S}_h} \alpha [\![\delta u]\!]^{(k)} \cdot \boldsymbol{T_{TSL}}^{(k)} \, \mu^{(k)} d\mathcal{S} + \sum_{k=1}^{n-1} \int_{\mathcal{S}_h} (1-\alpha) \frac{\beta}{h_s^{(k)}} [\![u]\!]^{(k)} \cdot [\![\delta u]\!]^{(k)} \, d\mathcal{S} \\ &= \int_h \int_{\partial_N \mathcal{S}_h} \delta u \cdot \bar{\boldsymbol{T}} \, \mu d\mathcal{S} d\xi_3 + \int_h \int_{\mathcal{S}_h} \delta u \cdot \mathbf{f} \, \mu d\mathcal{S} d\xi_3 \end{aligned} \tag{A.19}$$

Appendix B

Configuration of an Undeformed Shell

An example of a mapping $\boldsymbol{\varphi}^0$ for plates is [81]:

$$\varphi_1^0 = \xi_1 \qquad \varphi_2^0 = \xi_2 \qquad \varphi_3^0 = \xi_3 \tag{B.1}$$

With:

$$\Phi^0 = \boldsymbol{\varphi}^0 + \xi_3 \mathbf{t}^0 \tag{B.2}$$

The convected basis is calculated as:

$$a_1^0 \coloneqq \frac{\partial \boldsymbol{\varphi}^0}{\partial \xi_1} = \begin{bmatrix} 1 \\ 0 \\ 0 \end{bmatrix} \qquad a_2^0 \coloneqq \frac{\partial \boldsymbol{\varphi}^0}{\partial \xi_2} = \begin{bmatrix} 0 \\ 1 \\ 0 \end{bmatrix} \qquad \mathbf{t}^0 = \frac{a_1 \times a_2}{\|a_1 \times a_2\|} = \begin{bmatrix} 0 \\ 0 \\ 1 \end{bmatrix} \tag{B.3}$$

Using the convected basis, the surface metric tensor is:

$$a_{\alpha\beta}^0 = \partial_\alpha \boldsymbol{\varphi} \cdot \partial_\beta \boldsymbol{\varphi} = \begin{bmatrix} 1 & 0 \\ 0 & 1 \end{bmatrix} \tag{B.4}$$

The Jacobian of the surface metric tensor can be shown to be equal to one since in the case of a plate $\mathrm{d}\mathcal{S}$ is equal to $\mathrm{d}\mathcal{A}$. The covariant base vectors g_i^0 are:

$$g_1^0 \coloneqq \frac{\partial \Phi^0}{\partial \xi_1} = \begin{bmatrix} 1 \\ 0 \\ 0 \end{bmatrix} \qquad g_2^0 \coloneqq \frac{\partial \Phi^0}{\partial \xi_2} = \begin{bmatrix} 0 \\ 1 \\ 0 \end{bmatrix} \qquad g_3^0 = \mathbf{t}^0 = \begin{bmatrix} 0 \\ 0 \\ 1 \end{bmatrix} \tag{B.5}$$

The metric tensor of the entire body is then given by:

$$g_{ij}^0 = g_i^0 \cdot g_j^0 = \begin{bmatrix} 1 & 0 & 0 \\ 0 & 1 & 0 \\ 0 & 0 & 1 \end{bmatrix} \tag{B.6}$$

Finally, the shifter tensor is given as:

$$\mu_\alpha^\beta = \begin{bmatrix} 1 & 0 \\ 0 & 1 \end{bmatrix} \tag{B.7}$$

Its determinant does not depend on the thickness coordinate ξ_3. This implies that in the reference configuration, quantities are the same in both the $\{a_\alpha^0\}_{\alpha=1,2}$ and in the $\{g_i^0\}_{i=1,2,3}$ reference frames. This is a trivial result, however, for curved shells, different interfaces will have different areas.

Appendix C

Exponential Map

C.1. Rotation Group and its Lie Algebra

Following [41], SO(3) is denoted by the rotation group of all possible orthogonal transformations in $\mathbb{R}^3$ with determinant equal to +1. Formally:

$$\mathrm{SO}(3) \coloneqq \left\{ \boldsymbol{\Lambda} \in \mathbb{R}^3 \to \mathbb{R}^3 \mid \boldsymbol{\Lambda}^T = \boldsymbol{\Lambda}^{-1} \text{ and } \det(\boldsymbol{\Lambda}) = +1 \right\} \tag{C.1}$$

This means all proper orthogonal rotation tensors that preserve the angle between vectors and their magnitude. Any matrix $\boldsymbol{\Lambda} \in \mathrm{SO}(3)$ possesses an eigenvector $\Psi \in \mathbb{R}^3$ such that:

$$\boldsymbol{\Lambda}\Psi = \Psi \tag{C.2}$$

Geometrically, $\boldsymbol{\Lambda}$ represents a rotation about Ψ. The tangent space to SO(3) at the identity matrix $\boldsymbol{I}$ is denoted by so(3). The identity matrix $\boldsymbol{I}$ represents zero rotation, so the tangent space at the identity matrix consists of all infinitesimal rotations (rotations close to identity). These infinitesimal rotations are described by elements of so(3), which is the Lie algebra of SO(3). Hence, so(3) describes all rotations with infinitesimally small increments. This set consists of all skew-symmetric matrices, and is defined as:

$$\mathrm{so}(3) \coloneqq \left\{ \hat{\boldsymbol{\Theta}} \in \mathbb{R}^3 \to \mathbb{R}^3 \mid \hat{\boldsymbol{\Theta}}^T = -\hat{\boldsymbol{\Theta}} \right\} \tag{C.3}$$

Any matrix $\hat{\boldsymbol{\Theta}} \in \mathrm{so}(3)$ has an eigenvector $\Theta \in \mathbb{R}^3$ such that:

$$\hat{\boldsymbol{\Theta}}\Theta = 0 \tag{C.4}$$

This defines the isomorphism $\hat{\bullet}$: so(3) $\to \mathbb{R}^3$ by the relation:

$$\hat{\boldsymbol{\Theta}} h = \Theta \times h \quad \forall h \in \mathbb{R}^3 \tag{C.5}$$

For any $\hat{\boldsymbol{\Theta}} \in \mathrm{so}(3)$, the matrix representation relative to the inertial basis $\{\mathbf{E}_i\}_{i=1,2,3}$ is:

$$\hat{\boldsymbol{\Theta}} = \begin{bmatrix} 0 & -\Theta_3 & \Theta_2 \\ \Theta_3 & 0 & -\Theta_1 \\ -\Theta_2 & \Theta_1 & 0 \end{bmatrix}, \quad \Theta = \begin{bmatrix} \Theta_1 \\ \Theta_2 \\ \Theta_3 \end{bmatrix} \tag{C.6}$$

where $\Theta_1, \Theta_2, \Theta_3$ are components of the eigenvector Θ. The tangent space at any $\boldsymbol{\Lambda}$ is given by rotating so(3):

$$\hat{\boldsymbol{\theta}} = \boldsymbol{\Lambda}\hat{\boldsymbol{\Theta}}\boldsymbol{\Lambda}^T \tag{C.7}$$

Now the set of finite rotations with rotation axis perpendicular to $\mathbf{E_3}$ can be defined as:

$$S^2_{\mathbf{E_3}} \coloneqq \left\{ \boldsymbol{\Lambda} \in \mathrm{SO}(3) \mid \text{ where } \Psi \in \mathbb{R}^3, \text{such that } \boldsymbol{\Lambda}\Psi = \Psi, \text{satisfies } \Psi \cdot \mathbf{E_3} = 0 \right\} \tag{C.8}$$

It can thus be stated that $S^2_{\mathbf{E_3}}$ is a subset of SO(3), e.g., ($S^2_{\mathbf{E_3}} \subset \mathrm{SO}(3)$). Essentially, each point on the unit sphere S^2 can be uniquely associated with a certain rotation $\boldsymbol{\Lambda}$ in $S^2_{\mathbf{E_3}}$. As before, the tangent space at the identity can be defined as:

$$T_I S^2_{\mathbf{E_3}} \coloneqq \left\{ \hat{\boldsymbol{\Theta}} \in \mathrm{so}(3) \mid \text{ where } \Theta \cdot \mathbf{E_3} = 0 \right\} \tag{C.9}$$

C.2. Derivation of Rotation Tensor

The *exponential mapping* exp: $so(3) \rightarrow SO(3)$ maps infinitesimal rotations, which are represented by skew-symmetric matrices in so(3) and transform incremental changes in orientation, into finite rotations. These finite rotations are represented by orthogonal rotation matrices in SO(3), which actually perform the incremental rotation on directors. The derivation starts with the rotation formula, it holds for any rotation around any axis no matter its magnitude [82]:

$$\exp[\hat{\boldsymbol{\Theta}}] = \boldsymbol{\Lambda} = \cos(\|\Theta\|)\boldsymbol{I} + \sin(\|\Theta\|)\hat{e} + (1 - \cos(\|\Theta\|))e \otimes e \tag{C.10}$$

Where $e = \frac{\Theta}{\|\Theta\|}$ and $\hat{e}$ is its skew-symmetric counterpart. Since $\mathbf{t} = \boldsymbol{\Lambda}\mathbf{E_3}$:

$$\mathbf{t} = (\cos(\|\Theta\|)\boldsymbol{I} + \sin(\|\Theta\|)\hat{\boldsymbol{e}} + (1 - \cos(\|\Theta\|))e \otimes e)\mathbf{E_3} \tag{C.11}$$

This can be rewritten as:

$$\mathbf{t} = \cos(\|\Theta\|)\mathbf{E_3} + \sin(\|\Theta\|)(e \times \mathbf{E_3}) + (1 - \cos(\|\Theta\|))(\mathbf{E_3} \cdot e)e \tag{C.12}$$

Since $\mathbf{E_3} \cdot e = 0$ this equation simplifies to:

$$\mathbf{t} = \cos(\|\Theta\|)\mathbf{E_3} + \sin(\|\Theta\|)(e \times \mathbf{E_3}) \tag{C.13}$$

Thus $\mathbf{t} = \boldsymbol{\Lambda}\mathbf{E_3}$ becomes $\cos(\|\Theta\|)\mathbf{E_3} + \sin(\|\Theta\|)(e \times \mathbf{E_3})$. From this equation the following relations can be obtained:

$$\mathbf{t} \cdot \mathbf{E_3} = (\cos(\|\Theta\|)\mathbf{E_3} + \sin(\|\Theta\|)(e \times \mathbf{E_3})) \cdot \mathbf{E_3} \tag{C.14a}$$

$$\mathbf{E_3} \times \mathbf{t} = \mathbf{E_3} \times (\cos(\|\Theta\|)\mathbf{E_3} + \sin(\|\Theta\|)(e \times \mathbf{E_3})) \tag{C.14b}$$

Which becomes:

$$\mathbf{t} \cdot \mathbf{E_3} = \cos(\|\Theta\|) \tag{C.15a}$$

$$\mathbf{E_3} \times \mathbf{t} = \sin(\|\Theta\|)\mathbf{E_3} \times (e \times \mathbf{E_3}) = \sin(\|\Theta\|)[e - (\mathbf{E_3} \cdot e)\mathbf{E_3}] = \sin(\|\Theta\|)e \tag{C.15b}$$

Where Lagranges's formula $c \times (a \times b) = (c \cdot b)a - (c \cdot a)b$ has been used. Substituting these two equation into Equation C.10 while leaving the last term as is:

$$\exp[\hat{\Theta}] = \boldsymbol{\Lambda} = (\mathbf{t} \cdot \mathbf{E_3})\boldsymbol{I} + \widehat{\mathbf{E_3} \times \mathbf{t}} + (1 - \cos(\|\Theta\|))e \otimes e \tag{C.16}$$

Now focussing on the last term:

$$(1 - \cos(\|\Theta\|))e \otimes e \tag{C.17}$$

Starting with:

$$\sin^2(\|\Theta\|) + \cos^2(\|\Theta\|) = 1 \tag{C.18}$$

Rearranging this and dividing both sides by $1 + \cos(\|\Theta\|)$:

$$\frac{\sin^2(\|\Theta\|)}{1 + \cos(\|\Theta\|)} = \frac{1 - \cos^2(\|\Theta\|)}{1 + \cos(\|\Theta\|)} \tag{C.19}$$

Simplifying the right-hand side:

$$\frac{\sin^2(\|\Theta\|)}{1 + \cos(\|\Theta\|)} = 1 - \cos(\|\Theta\|) \tag{C.20}$$

Substituting this into the original term:

$$(1 - \cos(\|\Theta\|))e \otimes e = \frac{\sin^2(\|\Theta\|)}{1 + \cos(\|\Theta\|)}e \otimes e \tag{C.21}$$

Now, expressing $e \otimes e$ in terms of $\mathbf{E_3} \times \mathbf{t}$:

$$e = \frac{\mathbf{E_3} \times \mathbf{t}}{\sin(\|\Theta\|)} \tag{C.22}$$

$$e \otimes e = \left(\frac{\mathbf{E_3} \times \mathbf{t}}{\sin(\|\Theta\|)}\right) \otimes \left(\frac{\mathbf{E_3} \times \mathbf{t}}{\sin(\|\Theta\|)}\right) = \frac{1}{\sin^2(\|\Theta\|)}(\mathbf{E_3} \times \mathbf{t}) \otimes (\mathbf{E_3} \times \mathbf{t}) \tag{C.23}$$

Substitute into the previous:

$$(1 - \cos(\|\Theta\|))e \otimes e = \frac{\sin^2(\|\Theta\|)}{1 + \cos(\|\Theta\|)} \cdot \frac{1}{\sin^2(\|\Theta\|)}(\mathbf{E_3} \times \mathbf{t}) \otimes (\mathbf{E_3} \times \mathbf{t}) \tag{C.24}$$

Simplifying:

$$(1 - \cos(\|\Theta\|))e \otimes e = \frac{1}{1 + \cos(\|\Theta\|)}(\mathbf{E_3} \times \mathbf{t}) \otimes (\mathbf{E_3} \times \mathbf{t}) \tag{C.25}$$

The final explicit representation then becomes:

$$\exp[\hat{\Theta}] = \mathbf{\Lambda} = (\mathbf{t} \cdot \mathbf{E_3})\boldsymbol{I} + (\widehat{\mathbf{E_3} \times \mathbf{t}}) + \frac{1}{1 + \mathbf{t} \cdot \mathbf{E_3}}(\mathbf{E_3} \times \mathbf{t}) \otimes (\mathbf{E_3} \times \mathbf{t}) \tag{C.26}$$

C.3. Derivation of $\exp_{\mathbf{t}_A^k}$

Starting with the following expression which presents the incremental rotation of the director:

$$\mathbf{t}_A^{k+1} = \exp[\hat{\boldsymbol{\theta}}]\mathbf{t}_A^k = \exp_{\mathbf{t}_A^k}[\Delta\mathbf{t}_A] \tag{C.27}$$

Where $\boldsymbol{\theta} \coloneqq \mathbf{t}_A^k \times \Delta\mathbf{t}_A$, that is director variations $\Delta\mathbf{t}_A$ are perpendicular to the infinitesimal rotations axis $\boldsymbol{\theta}$. As a result $\boldsymbol{\theta} \cdot \mathbf{t}_A^k = \Delta\mathbf{t}_A \cdot \mathbf{t}_A^k = 0$. The rotation formula is given as before:

$$\exp[\hat{\boldsymbol{\theta}}] = \mathbf{\Lambda} = \cos(\|\boldsymbol{\theta}\|)\boldsymbol{I} + \sin(\|\boldsymbol{\theta}\|)\hat{e} + (1 - \cos(\|\boldsymbol{\theta}\|))e \otimes e \tag{C.28}$$

Multiplying this formula by the previous nodal director and rewriting it as:

$$\mathbf{t}_A^{k+1} = \cos(\|\boldsymbol{\theta}\|)\mathbf{t}_A^k + \sin(\|\boldsymbol{\theta}\|)(e \times \mathbf{t}_A^k) + (1 - \cos(\|\boldsymbol{\theta}\|))(\mathbf{t}_A^k \cdot e)e \tag{C.29}$$

Since $e = \frac{\boldsymbol{\theta}}{\|\boldsymbol{\theta}\|}$, $(\mathbf{t}_A^k \cdot e)$ is zero as defined before:

$$\mathbf{t}_A^{k+1} = \cos(\|\boldsymbol{\theta}\|)\mathbf{t}_A^k + \frac{\sin(\|\boldsymbol{\theta}\|)}{\|\boldsymbol{\theta}\|}(\boldsymbol{\theta} \times \mathbf{t}_A^k) \tag{C.30}$$

It also holds that $\boldsymbol{\theta} \times \mathbf{t}_A^k = \Delta\mathbf{t}_A$, substituting this into the previous result together with the fact that $\|\boldsymbol{\theta}\| = \|\Delta\mathbf{t}_A\|$ results in the expression:

$$\mathbf{t}_A^{k+1} = \cos(\|\Delta\mathbf{t}_A\|)\mathbf{t}_A^k + \frac{\sin(\|\Delta\mathbf{t}_A\|)}{\|\Delta\mathbf{t}_A\|}\Delta\mathbf{t}_A \tag{C.31}$$

C.4. Derivation of $\Delta\mathbf{\Lambda}_A$

As before, starting with the following expression which presents the incremental rotation of the director:

$$\mathbf{t}_A^{k+1} = \exp[\hat{\boldsymbol{\theta}}]\mathbf{t}_A^k = \exp_{\mathbf{t}_A^k}[\Delta\mathbf{t}_A] \tag{C.32}$$

From this the unique rotation can be determined:

$$\mathbf{t}_A^{k+1} = \Delta\mathbf{\Lambda}_A\mathbf{t}_A^k \tag{C.33}$$

With rotation axis $\boldsymbol{\theta} \coloneqq \mathbf{t}_A^k \times \Delta\mathbf{t}_A$ as before. Using this, the rotation is given by:

$$\Delta\mathbf{\Lambda}_A = \cos(\|\boldsymbol{\theta}\|)\boldsymbol{I} + \sin(\|\boldsymbol{\theta}\|)\hat{\boldsymbol{e}} + (1 - \cos(\|\boldsymbol{\theta}\|))e \otimes e \tag{C.34}$$

Using $e = \frac{\boldsymbol{\theta}}{\|\boldsymbol{\theta}\|}$ and $\boldsymbol{\theta} \coloneqq \mathbf{t}_A^k \times \Delta\mathbf{t}_A$, this becomes:

$$\Delta\mathbf{\Lambda}_A = \cos(\|\mathbf{t}_A^k \times \Delta\mathbf{t}_A\|)\boldsymbol{I} + \frac{\sin(\|\mathbf{t}_A^k \times \Delta\mathbf{t}_A\|)}{\|\mathbf{t}_A^k \times \Delta\mathbf{t}_A\|}\widehat{(\mathbf{t}_A^k \times \Delta\mathbf{t}_A)} + \frac{(1 - \cos(\|\mathbf{t}_A^k \times \Delta\mathbf{t}_A\|))}{\|\mathbf{t}_A^k \times \Delta\mathbf{t}_A\|^2}(\mathbf{t}_A^k \times \Delta\mathbf{t}_A) \otimes (\mathbf{t}_A^k \times \Delta\mathbf{t}_A) \tag{C.35}$$

The final results follows from the fact that $\|\mathbf{t}_A^k \times \Delta\mathbf{t}_A\| = \|\boldsymbol{\theta}\|$, which is equal to $\|\Delta\mathbf{t}_A\|$:

$$\Delta\mathbf{\Lambda}_A = \cos(\|\Delta\mathbf{t}_A\|)\boldsymbol{I} + \frac{\sin(\|\Delta\mathbf{t}_A\|)}{\|\Delta\mathbf{t}_A\|}\widehat{(\mathbf{t}_A^k \times \Delta\mathbf{t}_A)} + \frac{(1 - \cos(\|\Delta\mathbf{t}_A\|))}{\|\Delta\mathbf{t}_A\|^2}(\mathbf{t}_A^k \times \Delta\mathbf{t}_A) \otimes (\mathbf{t}_A^k \times \Delta\mathbf{t}_A) \tag{C.36}$$